On the Conversion of Plastic Work into Heat

Thesis by
Jon Hodowany

In Partial Fulfillment of the Requirements
for the Degree of
Doctor of Philosophy

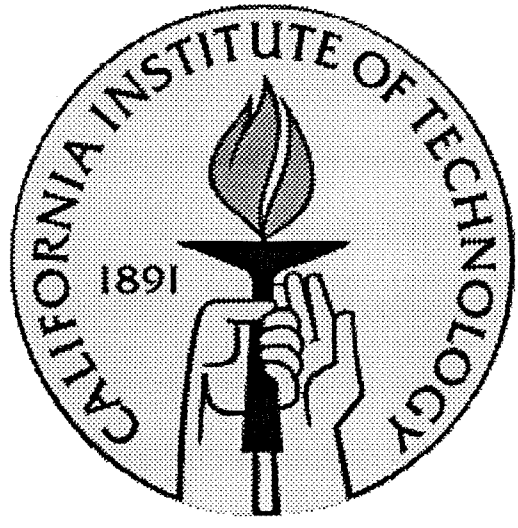

California Institute of Technology
Pasadena, California
1997
Submitted May 20, 1997

ACKNOWLEDGEMENTS

For several years, I have looked forward to writing this section, if for no other reason than to be able to use the first person in a technical document.

I was fortunate to work with not one, but two excellent mentors in Prof. Ravichandran and Prof. Rosakis. Prof. Ravichandran is very much a realist, and was always straight with me on all matters. He is also a veritable encyclopedia, encompassing a plethora of scientific and non-scientific subjects. I am convinced that if academics had not beckoned, he could have made a fortune as a contestant on Jeopardy. Prof. Rosakis is a true optimist, like myself, and was always an encouraging influence in our numerous discussions. It was fun to watch him get excited about mechanics problems, and his youthful vigor, in my opinion, is his greatest asset. A hearty thanks goes out to the other distinguished faculty who took interest in my thesis work. I benefited greatly from my interaction with Prof. Miguel Ortiz, a dedicated scholar and the trend-setter in computational mechanics. The insightful theory that Prof. Phoebus Rosakis contributed to this project was invaluable, and lends some legitimacy to a very controversial topic. One of my favorite instructors at Caltech was Prof. Kaushik Bhattacharya. His comprehensive knowledge of continuum mechanics, together with an organized teaching style and a very cool British accent, contributed greatly to my intellectual development.

Thanks to all my colleagues at the Boeing Company, especially Donald Sandstrom, Tom Skillman, and Mike Hyatt. Don and Tom are my company mentors, and I aspire to match their enthusiasm, professionalism, and all-around good nature. Mike

Hyatt, one of the company's premier metallurgists, taught me a great deal about aluminum alloys.

Thanks to Y.D.S. Rajapakse of the Office of Naval Research, and Oscar Dillon of the National Science Foundation for their generous financial support.

My Caltech experience was definitely enriched by friends and colleagues. There wasn't a day that went by that I didn't have a hearty discussion with Dr. David Owen. Dave and I go back to our time at UCSD, and I will always consider him one of my closest friends. It's amazing that in only five years time, Dave and I were able to solve the majority of society's problems over Whoppers at Burger King. Maybe it's in the food. Thanks to many fellow students and friends, most notably Dr. John Lambros, Dr. Mark Walter, Dr. Weinong Chen, the soon-to-be Dr. Karina Montilla, Dr. Tony Deng, Dr. Raman Singh, Eduardo Repetto, and my favorite Ukrainian-Argentinian, Raul Radovitzky. As an experimentalist, the first thing you learn is to befriend the local machine shop artisans. In my case, these were Joe Haggerty, and his two cronies, Larry Frazier and Ali Kiani. Thanks for all the help and advice. The stylish Lydia Suarez was both a secretary deluxe, and a master authority on talk radio. What credentials.

Finally, I would like to acknowledge the love and encouragement of my wife Judy. She is, and will always be, my best friend and companion. Watching her accumulate shoes and other luxury items made me realize that I could be the first graduate student at Caltech to file Chapter 11. This was the inspiration I needed to complete my degree requirements in a timely fashion.

ABSTRACT

The present study investigated heat evolution in metal plasticity. Specifically, experiments were designed to measure the partition of plastic work into heat and stored energy during dynamic deformations. The fraction of plastic work converted into heat has implications in a wide range of thermomechanical phenomena, including shear bands, dynamic fracture, ballistic penetration and high speed machining.

Kolsky bars, in compression and torsion, were used to determine mechanical properties at strain rates between 10^3 s^{-1} and 10^4 s^{-1}. For dynamic loading, in-situ temperature changes were measured using a high-speed HgCdTe photoconductive detector. Specially designed infrared optics, configured in tandem with the HgCdTe detector and the Kolsky bar constituted a novel experimental configuration for determining the fraction of plastic work converted into heat, and thus, the amount of energy stored in metals. The temperature detection system was ideally suited for small temperature excursions from ambient conditions, and was sensitive to temperature changes as little as 0.5 °C. The emissivity of metals was found to increase above certain high levels of plastic strain due to changes in surface roughness, which can affect the validity of temperature calibration. A technique of sample recovery, rough surface layer removal, and reloading was employed to obtain large plastic strains in the Kolsky bar. A Materials Testing System (MTS) servo-hydraulic load frame was used to measure mechanical properties at lower strain rates, 10^{-5} s^{-1} to 1 s^{-1}. When temperature measurement was needed within this range of strain rates, a fast E-type thin wire thermocouple, with a time response of 1 ms, was employed.

The fraction of plastic work converted into heat, β, was treated as a constitutive function of strain and strain rate in the heat conduction equation. 2024 aluminum alloy and commercially pure α-titanium were the metal systems used in the current study to determine the functional dependence of β on strain and strain rate. The T351, T4 and T6 tempers of 2024 aluminum did not exhibit strain rate dependence in flow stress over the entire range of strain rates tested. At low levels of plastic strain, all tempers of 2024 aluminum stored more than 50% of the input plastic work. At some level of plastic strain, depending on temper, 2024 aluminum could no longer store plastic work. After this point, β increased to a value near 1.0 and remained nearly constant during subsequent plastic deformation. When averaged over all strains, β was 0.85-0.95 depending on the particular heat treatment. The fraction of plastic work dissipated as heat was not found to be sensitive to strain rate over a wide range of strain rates. In contrast, the flow stress of α-titanium was strongly dependent on strain rate. The initial flow stress increased by more than 15% between strain rates of 10^{-3} s^{-1} and 10^{3} s^{-1}. In addition, the strain hardening was also observed to be rate dependent. For fixed plastic strain, the tangent modulus increased as strain rate increased. Titanium dissipated a greater proportion of energy as heat at low strains than all tempers of 2024 aluminum. The ability to store energy in titanium decreased with increasing plastic strain. For plastic strains above 0.3, titanium dissipated nearly all input plastic work as heat. The proportion of energy dissipated as heat at fixed strain increased as strain rate increased.

TABLE OF CONTENTS

CHAPTER 1

INTRODUCTION

1.1 Motivation

Many important problems in engineering involve dynamic events. In some sense, all problems have dynamic character. For example, consider constant loads on a bridge or truss, which at first glance is a static equilibrium problem. Engineers who study creep deformation would argue that over a long enough time scale, the bridge problem is actually one of dynamics. Time scale is an important consideration in the physics of any problem.

Many problems of engineering mechanics, especially those that involve short time dynamic events, are difficult to duplicate in the laboratory. A practical example is the high speed machining of metals. The deformation in the vicinity of the tool in a machining process is inherently dynamic, and very difficult to instrument if one wishes to measure properties such as stress, strain or temperature. Also, the deformation process can be highly inhomogeneous, involving shear localization and fracture. Figure 1.1 is an example of an orthogonal machining simulation. Numerical simulations (e.g., Marusich and Ortiz, 1995) may be the only way to accurately characterize these problems. However, the accuracy of any computational model is invariably linked to the reliability of experimental information used as input to the model. Physical and thermal parameters, such as density, heat capacity, conductivity, resistivity, etc., and material

constitutive information, including stress-strain behavior and strain rate sensitivity, are required for accurate simulations.

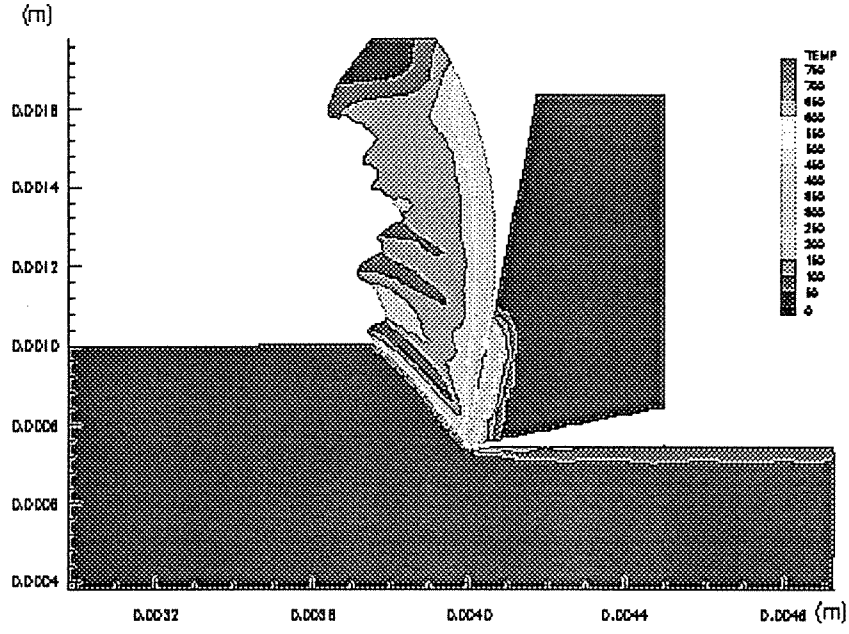

Figure 1.1 Contours of temperature in a finite element simulation of orthogonal machining of aluminum (courtesy of the Boeing Company, Seattle, WA).

When metals deform plastically, significant amounts of heat can be generated, especially in cases of highly localized deformation. If the deformation process is adiabatic, the heat generation can lead to a large temperature rise since there is no time to conduct heat away from the deforming metal. The temperature increase can cause thermal softening in the metal, and reduce its mechanical performance. Even at moderate strain rates, plastic deformation can often be treated as nearly adiabatic. Understanding the coupling between plastic deformation and heat evolution is fundamental to predicting temperature fields, and associated thermal softening, in engineering mechanics.

Part of the mechanical energy expended during a plastic deformation process is converted into heat, with the remainder stored in the material microstructure. The stored energy is an essential feature of the cold-worked state, and represents the change in

internal energy of the metal. Another characteristic of the stored energy of cold work is that it remains in the material after removal of external loads. This fact distinguishes cold work from reversible thermoelastic energy, which is recovered upon removal of the external loads. It is generally accepted that most of the mechanical energy is dissipated as heat during plastic deformation. The fraction of energy dissipated as heat is often treated as a constant parameter of 0.9, independent of material. The evidence for this is murky at best. Over the years, predictions of the amount of stored energy versus dissipated energy have varied considerably, even for nominally similar metals. Furthermore, no systematic study of the possible strain and strain rate dependence of the partition of energy during cold work has been attempted.

1.2 Review

1.2.1 Original Experiments of Taylor, Farren and Quinney

G. I. Taylor (Farren and Taylor, 1925; Taylor and Quinney, 1937) first published a series of experiments on the latent energy remaining in copper after cold working. At that time, the concepts of crystal dislocations and dislocation movement were in their infancy. In addition, the studies were handicapped by a lack of modern test equipment, nevertheless, many qualitative observations of metal plasticity were made.

The experiment of Taylor and Quinney (1937) was particularly noteworthy, in that large plastic strains were attained in torsion. A geared lathe loaded the long metal sample in torsion. The tailstock was connected to a lever, fitted with a spring balance used to measure load. Angular displacement was measured from the relative motion of two disks. Two methods were used to measure the heat evolved. First, an iron-constantan thermocouple was affixed onto the outer surface of the sample, and

temperature was recorded directly from a galvanometer. Second, the sample was removed from the load fixture after deformation, and dropped immediately into a calorimeter. It was claimed that both methods for measuring heat gave similar results. Mild steel, nearly pure iron, and copper were used as the test materials. The main conclusions are summarized here:

- The fraction of stored energy to total work, f, was never larger than 15%, at any strain.
- The fraction f was a function of the extent of deformation. As the amount of cold work increased, the ability of the metal to store energy decreased.
- The fraction, f, remained nearly constant (10-12%), for copper and mild steel, over a relatively large range of strains.
- There exists a saturation point, after which the metal cannot store any more energy.

Taylor's experiments contained many potential sources of error. The technique for measuring torque and angular displacement was quite crude, leading to possible errors when calculating total work. Tests generally lasted tens of seconds, which allowed for heat conduction from the ends of the samples. In addition, since the work rate in torsion is not uniform over the entire volume of the sample, temperature was measured several seconds after each test was completed. Calorimetry has an advantage over direct temperature measurement in this case. Without knowledge of microstructural mechanisms for energy storage and strain hardening, Taylor concluded "the fact that the absorption of latent energy and the increase in strength with increasing strain both cease

when the same amount of cold work has been applied suggests that the strength of pure metals may depend only on the amount of cold work which is latent in them."

1.2.2 Other Attempts over the Years.

The review text by Bever, Holt and Titchener (1973) gives an excellent overview of various attempts to measure the stored energy of cold work. The text also covers basic thermodynamic aspects of plasticity, and microstructural characteristics of the cold worked state. There will be no attempt here to include the wealth of material found in the text, but it is instructive to elucidate general conclusions and quote results of research of particular interest to the present study.

In measuring the stored energy of cold work, the vast majority of investigations considered low strain rate deformation processes. Data for stored energy at high strain rates is scarce. Appleton (1961), Iyer and Gordon (1962), Scattergood et al. (1963), and Beardmore et. al. (1964) measured stored energy for metals during shock loading. Each of these studies employed anisothermal annealing techniques to measure stored energy, and did not report on the ratio of stored energy to total work. Williams (1961, 1962, 1963) provided data on energy storage during compression by impact. A single-step approach, which will be described later, was used, which gave not only an estimation of the stored energy, but of the ratio of stored energy to total work. Nakada (1965) also used single-step methods to measure stored energy in aluminum and silver single crystals. The only other notable work at high strain rates measured stored energy during wire drawing and extrusion. For these experiments, it is difficult to obtain useful comparisons to data obtained from conventional loading devices.

Mason et al. (1994) made the first systematic attempt to measure the strain dependence of the partition of plastic work during dynamic deformations. Although demonstrating that the amount of stored energy should be treated as a function of strain, they were hampered by a lack of temperature resolution of their thermal transducer near ambient conditions.

For lower strain rates, there is no such dearth of data, and the reader is referred to Table 3.1 of Bever, Holt and Titchener (1973). Specific work will be cited where a comparison of results is appropriate. Of note, however, is the large scatter in data, even for studies on nominally similar materials. Copper, historically, has been the most widely studied metals concerning the stored energy of cold work. Ironically, based on data summarized in the review text of Bever et al., copper has the least consensus as to the relative partition of plastic work into heat and stored energy.

1.3 Objectives

There is much speculation as to how and how much plastic work is stored in metals during deformation. The literature is no comfort, and it is in fact disturbing that such a large spread in values of stored energy exists for nominally similar materials. It is perhaps more disturbing that in absence of clarifying data, the solid mechanics community assumes a constant value of stored energy relative to input work for coupled thermomechanical problems.

The present study attempted to measure the partition of plastic work into dissipated heat and stored energy during dynamic deformations. The goal was not to merely obtain volumes of data on a variety of metals, but to incorporate and adapt modern sensing devices to improve on previous attempts to measure heat generation

during plastic deformation. Of particular interest was the variation in stored energy with strain and strain rate. Also, a relative comparison of energy storage in strain rate sensitive and strain rate insensitive metals was desired.

Chapter 2 outlines the underlying thermodynamics of plasticity with internal variables. Implications of the first and second laws of thermodynamics on the various thermodynamics functions and mechanical field quantities are discussed. The fundamental coupled heat conduction equation of continuum plasticity with internal variables is rewritten, clearly elucidating a thermodynamic basis for the strain and strain rate dependence of the plastic source term. Several special processes, relevant to experimental mechanics, are considered, leading to a usable form of the heat conduction equation.

Several experimental techniques to measure the terms of the heat conduction equation are discussed in Chapter 3. The Kolsky bar, used to generate one-dimensional loading pulses, is reviewed. The chapter also deals with the intricacies of temperature measurement. Remote photoconductive and photovoltaic temperature sensors are compared with contact sensors, such as thermocouples. Techniques for maximizing the accuracy of temperature measurements are given. The integration of temperature measurement with mechanical loading provides several experimental setups for measuring the partition of plastic work into heat and stored energy in metals. Finally, the various sources of error, both small and significant, are analyzed and discussed.

Chapter4 and Chapter 5 show the strain and strain rate dependence of the partition of plastic work for strain rate sensitive and insensitive metals, respectively. Chapter 4 deals primarily with α-titanium. Stress-strain strain curves over a spectrum of strain rates

are plotted to show the relative strain rate sensitivity in flow stress. The fraction of plastic work dissipated as heat as a function of strain and strain rate is given. Chapter 5 investigates the partition of plastic work in several tempers of 2024 aluminum alloy. 2024 aluminum is demonstrated to be strain rate sensitive between strain rates of 10^{-3} s^{-1} and 10^{3} s^{-1}. The functional dependence of the partition of plastic work on strain and strain rate is given for dynamic torsion and compression. Also, the variation of this parameter with hardening is investigated. Chapter 6 summarizes the important conclusions of the work presented here.

1.4 References

Appleton, A.S., Dieter, G.E., Bever, M.B. (1961), *Trans. Met. Soc. AIME*, **221**, 90.

Beardmore, P., Holtzman, A.H., Bever, M.B. (1964), *Trans. Met. Soc. AIME*, **230**, 725.

Bever, M.B., Holt, D.L., Titchener, A.L., (1973), "The Stored Energy of Cold Work," *Prog. Mat. Sci.*, **17**, 1.

Bodner, S.R., Lindenfeld, A. (1995), "Constitutive Modelling of the Stored Energy of Cold Work under Cyclic Loading," *Eur. J. Mech., A/Solids*, **14**, 333.

Farren, W.S., Taylor, G.I. (1925), "The Heat Developed during Plastic Extension of Metals," *Proc. Royal Soc.*, **A107**, 422.

Iyer, A.S., Gordon, P. (1962), *Trans. Met. Soc. AIME*, **224**, 1077.

Marusich, T.D., Ortiz, M. (1995), "Modelling and Simulation of High-Speed Machining," *Int. J. for Numerical Methods in Engineering*, **38**, 3675.

Mason, J.J., Rosakis, A.J, Ravichandran, G. (1994), *Mech. of Materials*, **17**, 135.

Nakada, Y. (1965), *Phil Mag.*, **11**, 251.

Scattergood, R.O., Beardmore, P., Bever, M.B. (1963), *Trans. Met. Soc. AIME*, **227**, 1468.

Taylor, G.I., Quinney, H. (1937), "The Latent Heat Remaining in a Metal after Cold Working," *Proc. Royal Soc.*, **A163**, 157.

Williams, R.O. (1961), *Acta Metall.*, **9**, 949.

Williams, R.O. (1962), *Trans. Met. Soc. AIME*, **224**, 719.

Williams, R.O. (1962), *Trans. Met. Soc. AIME*, **227**, 1290.

CHAPTER 2

THEORETICAL DEVELOPMENT

2.1 Irreversible Thermodynamics and Coupled Thermoplasticity

2.1.1 Preface

In an elastic continuum, every local state is an equilibrium state, that is, a state that has no tendency to change without a change in external boundary. Problems involving heat conduction, viscosity, and plasticity belong to the realm of non-equilibrium thermomechanics. The existence of non-equilibrium states is an essential feature of rate-dependent inelastic continua, and such non-equilibrium states evolve by means of irreversible processes. The fundamental laws of equilibrium thermodynamics are assumed valid for irreversible processes. However, there is no full agreement in the scientific community, or even within continuum mechanics, about the meaning of such variables as entropy, or the range of validity of the 2nd Law of Thermodynamics. One need only read the introductory chapter of Truesdell's *Rational Thermodynamics* (1983), or the paper by L.C. Woods (1982), to realize the existence of controversy within the field of continuum thermodynamics.

In this section, a theoretical framework for heat conduction in an elastic-plastic continuum, including the stored energy of cold work, will be developed. The theory developed here is not meant to be an exhaustive treatment of the subject. There is no attempt here to extract *the* most general statements of the first and second laws of

thermodynamics. The continuum thermodynamics approach will be used, with every effort made to report all underlying assumptions. The goal here is to establish relations that can be explored further with simple, elegant methods of experimental mechanics.

2.1.2 The 1st and 2nd Laws of Thermodynamics

The principle of energy balance asserts that, in a reference region R_0, there exists a state variable, e, such that

$$\frac{d}{dt}\int_{R_0}\rho_0 e dV_0 + \dot{K} = \dot{Q} + \dot{W}_t \tag{2.1}$$

where e is the internal energy density, $\dot{K}$ is the rate of change of kinetic energy, $\dot{Q}$ is the heat flow into R_0, and $\dot{W}_t$ is the total power applied to R_0. If we assume that all of the power is supplied by the applied loads and corresponding displacements, then

$$\dot{W}_t - \dot{K} = \dot{W} = \int_{R_0} \mathbf{S}\cdot\dot{\mathbf{E}} dV_0 \tag{2.2}$$

where $\dot{W}$ is the deformation power, **S** is the second Piola-Kirchhoff stress tensor, and **E** is the Green-St. Venant strain tensor. The heat flow into the body is

$$\dot{Q} = \int_{R_0}\rho_0 r dV_0 + \int_{\partial R_0}\mathbf{h}\cdot\mathbf{n} dA_0 \tag{2.3}$$

where r is body radiation power per unit mass, **h** is a vector representing heat inflow per unit undeformed surface area per unit time, and **n** is the outward normal. Using Gauss' theorem, the local energy equation in a Lagrangian formulation is (Lubliner, 1990)

$$\mathbf{S}\cdot\dot{\mathbf{E}} + \rho_0 r + \mathrm{div}\mathbf{h} = \rho_0\dot{e} \tag{2.4}$$

This formulation assumes no mass is transferred into R_0, but in the most general formulation, mass transfer would also be included.

The second law of thermodynamics for a homogeneous system is given here (Prigogine, 1947; Fung, 1965). There exists two single-valued functions of state, η, called the entropy density, and θ, the absolute temperature with the following properties:

- θ is a strictly positive number.
- The entropy of a system is equal to the sum of entropies of its parts.
- Total entropy is given by,

$$S = \int \rho_0 \eta dV_0 \tag{2.5}$$

- The entropy of a system can change in two distinct ways, by interaction with external surroundings and by internal processes.

$$dS = d_e S + d_i S \tag{2.6}$$

where dS denotes the change in entropy of the system, d_eS denotes the part of the change due to interaction with surroundings, and d_iS denotes the part of the change associated with internal processes. If dQ denotes the heat absorbed by the system from the surroundings, then

$$d_e S = \frac{dQ}{\theta} \tag{2.7}$$

d_iS is non-negative, that is

$d_i \eta > 0$ (irreversible process)

$d_i\eta = 0$ (reversible process)

$d_i\eta < 0$ (never occurs in nature)

Using the assumed form of heat addition, Q, from above, the application of this postulate leads to

$$\int_{R_0} \rho_0 \dot{\eta} dV_0 - \left[\int_{R_0} \rho_0 \frac{r}{\theta} dV_0 + \int_{\partial R_0} \frac{\mathbf{h}}{\theta} \cdot \mathbf{n} dA_0 \right] \equiv \Gamma \geq 0 \tag{2.8}$$

known as the Clausius-Duhem inequality, and is usually taken to be the general form of the second law of thermodynamics for continua, with some caveats explained below. Making use of Gauss' theorem, the local form of (2.8) is

$$\rho_0 \dot{\eta} - \rho_0 \frac{r}{\theta} - \rho_0 \mathrm{div}\left(\frac{\mathbf{h}}{\theta}\right) = \rho_0 \gamma \geq 0 \tag{2.9}$$

where

$$\Gamma = \int_{R_0} \rho_0 \gamma dV_0 \tag{2.10}$$

Introducing the Helmholtz free energy per unit mass, ψ,

$$\psi \equiv e - \theta\eta \tag{2.11}$$

and using the local form of the first law, the Clausius-Duhem inequality is recast as,

$$\mathbf{S} \cdot \dot{\mathbf{E}} - \rho_0 \dot{\psi} - \rho_0 \eta \dot{\theta} + \frac{1}{\theta} \mathbf{h} \cdot \mathrm{grad}\theta = \rho_0 \theta \gamma \geq 0 \tag{2.12}$$

For either adiabatic ($\mathbf{h}$=0), or homogenous processes (gradθ=0), (2.12) reduces to

$$\mathbf{S} \cdot \dot{\mathbf{E}} - \rho_0 \dot{\psi} - \rho_0 \eta \dot{\theta} \equiv \rho_0 \delta \geq 0 \tag{2.13}$$

where δ is defined by

$$\delta \equiv \frac{1}{\rho_0}\mathbf{S}\cdot\dot{\mathbf{E}} - \dot{\psi} - \eta\dot{\theta} \tag{2.14}$$

which can be interpreted as internal power dissipation per unit mass. Using this terminology the first law can be rewritten as

$$\rho_0\delta + \mathrm{div}\mathbf{h} + \rho_0 r = \rho_0\theta\dot{\eta} \tag{2.15}$$

The relations above are certainly valid for a thermoelastic solid (Carlson, 1972, Lubliner 1990) for which every local state is an equilibrium state. Furthermore, it is assumed that the reversible and irreversible parts of the total entropy are distinctly separable, and that the body radiation and heat flux terms represent *reversible* heat additions. For irreversible processes, the applicability is not as certain. Rational thermodynamics (Truesdell, 1984) suggests that entropy and temperature, which are associated with equilibrium states in the relations above, are also uniquely defined for non-equilibrium states. From this point of view, the Clausius-Duhem inequality holds for all states, whether it is an equilibrium state or not. Rice (1970) suggested that the above formulation of the second law can be applied to irreversible processes with the use of internal variables provided that the following is true: every achievable irreversible process may be considered a sequence of constrained equilibrium states corresponding to the instantaneous values of the internal variables.

2.1.3 Response Functions and Constitutive Assumptions

The material at point **X** in a reference configuration, R_0, is characterized by five response functions

$$
\begin{aligned}
\psi &= \hat{\psi}(\varepsilon^e, \theta, \xi) \\
\eta &= \hat{\eta}(\varepsilon^e, \theta, \xi) \\
\sigma &= \hat{\sigma}(\varepsilon^e, \theta, \xi) \\
\dot{\varepsilon}^P &= \hat{\mathbf{P}}(\varepsilon^e, \theta, \xi) \\
\dot{\xi} &= \hat{\Xi}(\varepsilon^e, \theta, \xi)
\end{aligned}
\tag{2.16}
$$

If we consider small strain theories of plasticity, then ε^e is the linearized elastic strain tensor, and is defined as $\varepsilon^e=\varepsilon-\varepsilon^P$, where ε and ε^P are the total strain and plastic strain, respectively (Mandel, 1972; 1973). Some remarks on the above constitutive assumptions:

- Truesdell's principle of equipresence (Truesdell and Toupin, 1960) is used, which asserts that a quantity present as an independent variable in one constitutive equation should so be present in all, unless it contradicts a general law of physics.
- The explicit dependence on the gradient of temperature, gradθ , is ruled out by the second law following the procedure of Coleman and Mizel (1964).
- A single internal variable, ξ, is used. The components of ε^P can also be thought of as internal variables, although they do not appear explicitly in (2.16). For multiple internal variables, ξ can be thought of as a vector, and Ξ as a vector valued function. Several researchers have developed theory based on multiple internal variables (see for example, Coleman and Gurtin (1967), Rice (1971)).
- Plasticity enters the theory through the definition of ε^e (Mandel, 1972).
- This formulation will lead to a rate-dependent theory, despite the absence of $\dot{\varepsilon}^e$ and $\dot{\theta}$ in the evolution equations for $\dot{\varepsilon}^P$ and $\dot{\xi}$.

For a linearized theory, the local representation of the first law applied below is

$$\rho_0\delta + \mathrm{div}\mathbf{h} + \rho_0 r = \rho_0\theta\dot{\eta} \tag{2.17}$$

where

$$\delta \equiv \frac{1}{\rho_0}\boldsymbol{\sigma}\cdot\dot{\boldsymbol{\varepsilon}} - \dot{\psi} - \eta\dot{\theta} \tag{2.18}$$

is the internal dissipation. Using this definition, the Clausius-Duhem inequality reduces to

$$\boldsymbol{\sigma}\cdot\dot{\boldsymbol{\varepsilon}} - \rho_0\dot{\psi} - \rho_0\eta\dot{\theta} \equiv \rho_0\delta \geq 0. \tag{2.19}$$

2.1.4 Consequences of the 2nd Law

The Clausius-Duhem inequality (2.19) and the constitutive definitions (2.16) are intimately coupled in the sense that one cannot use (2.19) until entropy is defined, but the Clausius-Duhem inequality is used as a restriction on the constitutive definition of entropy. In the thermoelastic case, where every local state is an equilibrium state, the definition of entropy, and the use of the Clausius-Duhem inequality as the general form of the second law, are less controversial. Assuming that entropy can be treated in a way similar to the thermoelastic case, the second law likewise restricts the constitutive quantities in an analogous fashion.

Using the chain rule, and constitutive form for free energy (2.16)

$$\begin{aligned}
&\hat{\psi}_{\boldsymbol{\varepsilon}^e}\cdot\dot{\boldsymbol{\varepsilon}}^e = \hat{\psi}_{\boldsymbol{\varepsilon}^e}\cdot\left(\dot{\boldsymbol{\varepsilon}} - \dot{\boldsymbol{\varepsilon}}^p\right)\\
&\dot{\psi} = \hat{\psi}_{\boldsymbol{\varepsilon}^e}\cdot\dot{\boldsymbol{\varepsilon}} - \hat{\psi}_{\boldsymbol{\varepsilon}^e}\cdot\dot{\boldsymbol{\varepsilon}}^p + \hat{\psi}_{\xi}\dot{\xi} + \hat{\psi}_{\theta}\dot{\theta}
\end{aligned} \tag{2.20}$$

Using (2.19) and (2.20),

$$\rho_0\delta = \left[\hat{\sigma} - \rho_0\hat{\psi}_{\varepsilon^e}\right]\cdot\dot{\varepsilon} - \rho_0\left[\hat{\eta} + \hat{\psi}_\theta\right]\dot{\theta} + \rho_0\left[\hat{\psi}_{\varepsilon^e}\cdot\hat{\mathbf{P}} - \hat{\psi}_\xi\hat{\Xi}\right] \geq 0 \tag{2.21}$$

Since this must hold for all $\dot{\varepsilon}$ and $\dot{\theta}$, and for any process. By considering certain convenient processes (Coleman and Gurtin, 1967), (2.21) is equivalent to

$$\begin{aligned}
&\hat{\sigma}(\varepsilon^e,\theta,\xi) = \rho_0\hat{\psi}_{\varepsilon^e}(\varepsilon^e,\theta,\xi)\\
&\hat{\eta}(\varepsilon^e,\theta,\xi) = -\hat{\psi}_\theta(\varepsilon^e,\theta,\xi) \qquad\qquad \forall(\varepsilon^e,\theta,\xi)\\
&\rho_0\left[\hat{\psi}_{\varepsilon^e}\cdot\hat{\mathbf{P}} - \hat{\psi}_\xi\hat{\Xi}\right] = \boldsymbol{\sigma}\cdot\dot{\boldsymbol{\varepsilon}}^P - \rho_0\hat{\psi}_\xi\dot{\xi} = \rho_0\delta \geq 0
\end{aligned} \tag{2.22}$$

which the reduced form of the second law given the constitutive assumptions (2.16). Assuming Fourier's linear phenomenological relation for heat conduction

$$\mathbf{h} = \mathbf{K}\cdot\mathbf{grad}\,\theta \tag{2.23}$$

where $\mathbf{K}$ is the conductivity tensor, and using (2.22), (2.17) becomes

$$\begin{aligned}
&\mathrm{div}\left(\mathbf{K}\cdot\mathbf{grad}\theta\right) + \rho_0 r + \left\{\boldsymbol{\sigma}\cdot\dot{\boldsymbol{\varepsilon}}^P - \rho_0\left(\hat{\psi}_\xi - \theta\hat{\psi}_{\xi\theta}\right)\dot{\xi}\right\} + \left\{\rho_0\theta\hat{\psi}_{\boldsymbol{\varepsilon}^e\theta}\cdot\dot{\boldsymbol{\varepsilon}}^e\right\} = -\rho_0\theta\hat{\psi}_{\theta\theta}\dot{\theta}\\
&\mathrm{div}\left(\mathbf{K}\cdot\mathbf{grad}\theta\right) + \rho_0 r + \left\{\dot{Q}^P\right\} + \left\{\dot{Q}^e\right\} = \rho_0 c\left(\varepsilon^e,\theta,\xi\right)\dot{\theta}
\end{aligned} \tag{2.24}$$

$\dot{Q}^P$ represents the part of the plastic power available for heating; $\dot{Q}^e$ is the thermoelastic power, and $c\left(\varepsilon^e,\theta,\xi\right)$ is the specific heat capacity per unit mass. (2.24) is the general form of the energy equation given the constitutive assumptions (2.16), with the restriction that the Clausius-Duhem inequality must be satisfied for all processes.

2.1.5 Heat Capacity Independent of Internal Variables

Following a procedure outlined by Rosakis et al. (1997), suppose heat capacity is independent of internal variables, i.e.

$$\hat{\psi}_{\theta\theta} = -\frac{c(\varepsilon^e,\theta)}{\theta} \tag{2.25}$$

from the definition of heat capacity. $\hat{\psi}(\varepsilon^e,\theta,\xi)$ can be found by integrating twice with respect to θ. (2.25) becomes

$$\hat{\psi}(\varepsilon^e,\theta,\xi) = \overset{1}{\psi}(\varepsilon^e,\theta) + \theta\,\overset{2}{\psi}(\varepsilon^e,\xi) + \overset{3}{\psi}(\varepsilon^e,\xi) \tag{2.26}$$

From this, the entropy density and stress are determined from (2.22), and internal energy density from the definition of the Helmholtz free energy (2.11)

$$\hat{\eta}(\varepsilon^e,\theta,\xi) = -\hat{\psi}_\theta = -\overset{1}{\psi}_\theta(\varepsilon^e,\theta) - \overset{2}{\psi}(\varepsilon^e,\xi) \tag{2.27}$$

$$\hat{\sigma}(\varepsilon^e,\theta,\xi) = \rho_0\hat{\psi}_{\varepsilon^e} = \overset{1}{\psi}_{\varepsilon^e}(\varepsilon^e,\theta) + \theta\,\overset{2}{\psi}_{\varepsilon^e}(\varepsilon^e,\xi) + \overset{3}{\psi}_{\varepsilon^e}(\varepsilon^e,\xi) \tag{2.28}$$

$$\begin{aligned}\hat{e} &= \hat{\psi} + \theta\hat{\eta} = \overset{1}{\psi}(\varepsilon^e,\theta) - \theta\,\overset{1}{\psi}_\theta(\varepsilon^e,\theta) + \overset{3}{\psi}(\varepsilon^e,\xi) \\ &= \overset{1}{e}(\varepsilon^e,\theta) + \overset{3}{\psi}(\varepsilon^e,\xi)\end{aligned} \tag{2.29}$$

Using (2.26), and differentiating

$$\begin{aligned}&\hat{\psi}_\xi - \theta\hat{\psi}_{\theta\xi} = \overset{3}{\psi}_\xi(\varepsilon^e,\xi) = \hat{e}_\xi \\ &\hat{\psi}_{\varepsilon^e\theta} = \overset{1}{\psi}_{\varepsilon^e\theta}(\varepsilon^e,\theta) + \overset{2}{\psi}_{\varepsilon^e}(\varepsilon^e,\xi)\end{aligned} \tag{2.30}$$

Substituting these relations into (2.24) assuming $\mathbf{K}=k\mathbf{1}$, the heat conduction equation reduces to

$$k\nabla^2\theta + \rho_0 r + \left\{\sigma\cdot\dot{\varepsilon}^p - \rho_0\hat{e}_\xi(\varepsilon^e,\theta,\xi)\dot{\xi}\right\} + \left\{\rho_0\theta(\overset{1}{\psi}_{\varepsilon^e\theta} + \overset{2}{\psi}_{\varepsilon^e})\cdot\dot{\varepsilon}^e\right\} = \rho_0 c(\varepsilon^e,\theta)\dot{\theta}$$

or, equivalently

$$k\nabla^2\theta + \rho_0 r + \left\{\sigma \cdot \dot{\varepsilon}^p - \rho_0 \hat{e}_\xi\left(\varepsilon^e, \theta, \xi\right)\dot{\xi}\right\} + \left\{\rho_0 \theta \hat{\sigma}_\theta \cdot \dot{\varepsilon}^e\right\} = \rho_0 c\left(\varepsilon^e, \theta\right)\dot{\theta} \qquad (2.31)$$

which holds for a specific heat capacity independent of internal variables.

2.1.6 Restrictions on the Stress Function

If the stress function, $\hat{\sigma}$, is independent of internal variables, that is

$$\hat{\sigma}_\xi = 0$$

then stress, from equation (2.28), is reduced to

$$\hat{\sigma}_\xi\left(\varepsilon^e, \theta, \xi\right) = \theta \overset{2}{\psi}_{\varepsilon^e\xi}\left(\varepsilon^e, \xi\right) + \overset{3}{\psi}_{\varepsilon^e\xi}\left(\varepsilon^e, \xi\right) = 0. \qquad \forall\theta \qquad (2.32)$$

In the case of uniaxial deformation, (2.31) is equivalent to the condition that elastic loading and unloading regions of the stress-strain curve are parallel. Since the above equation must hold for all θ, (2.32) implies

$$\begin{aligned} \overset{2}{\psi}_{\varepsilon^e\xi}\left(\varepsilon^e, \xi\right) &= 0 \\ \overset{3}{\psi}_{\varepsilon^e\xi}\left(\varepsilon^e, \xi\right) &= 0. \end{aligned} \qquad (2.33)$$

After integrating twice, with respect to ε^e and ξ

$$\begin{aligned} \overset{2}{\psi}\left(\varepsilon^e, \xi\right) &= -\overset{1}{\eta}\left(\varepsilon^e\right) - \overset{2}{\eta}\left(\xi\right) \\ \overset{3}{\psi}\left(\varepsilon^e, \xi\right) &= \overset{2}{e}\left(\varepsilon^e\right) + \overset{3}{e}\left(\xi\right). \end{aligned} \qquad (2.34)$$

The response functions are now rewritten with the restriction given by (2.34)

$$\hat{\psi}\left(\varepsilon^e, \theta, \xi\right) = \overset{1}{\psi}\left(\varepsilon^e, \theta\right) - \theta\left(\overset{1}{\eta}\left(\varepsilon^e\right) + \overset{2}{\eta}\left(\xi\right)\right) + \overset{2}{e}\left(\varepsilon^e\right) + \overset{3}{e}\left(\xi\right) \qquad (2.35)$$

$$\hat{\eta}(\varepsilon^e,\theta,\xi) = -\hat{\psi}_\theta = -\overset{1}{\psi}_\theta(\varepsilon^e,\theta) + \overset{1}{\eta}(\varepsilon^e) + \overset{2}{\eta}(\xi) \tag{2.36}$$

$$\hat{\sigma}(\varepsilon^e,\theta,\xi) = \rho_0\hat{\psi}_{\varepsilon^e} = \rho_0\left(\overset{1}{\psi}_{\varepsilon^e}(\varepsilon^e,\theta) + \overset{2}{e}'(\varepsilon^e) - \theta\,\overset{1}{\eta}'(\varepsilon^e)\right) \tag{2.37}$$

$$\hat{e} = \hat{\psi} + \theta\hat{\eta} = \overset{1}{e}(\varepsilon^e,\theta) + \overset{2}{e}(\varepsilon^e) + \overset{3}{e}(\xi) \tag{2.38}$$

Thus, the restriction on the stress function leads to a simplification of the coupled heat conduction equation (2.24), (2.30)

$$k\nabla^2\theta + \rho_0 r + \sigma\cdot\dot{\varepsilon}^p - \rho_0\,\overset{3}{e}'(\xi)\dot{\xi} + \rho_0\theta\hat{\psi}_{\varepsilon^e\theta}\cdot\dot{\varepsilon}^e = \rho_0 c(\varepsilon^e,\theta)\dot{\theta}\,. \tag{2.39}$$

2.1.7 Further Restrictions on Heat Capacity

Typically specific heat capacity is listed in handbooks as a function of temperature only, i.e., c=c(θ). If this functional form for heat capacity is assumed, the coupled heat conduction equation, (2.39), can be further reduced. From the definition of heat capacity, the Helmholtz free energy density becomes

$$\hat{\psi}(\varepsilon^e,\theta,\xi) = \overset{1}{\psi}(\theta) + \theta\,\overset{2}{\psi}(\varepsilon^e,\xi) + \overset{3}{\psi}(\varepsilon^e,\xi)\,. \tag{2.40}$$

After imposing the same restriction on the stress function as in the above section,

$$\hat{\psi}(\varepsilon^e,\theta,\xi) = \overset{1}{\psi}(\theta) - \theta\left(\overset{1}{\eta}(\varepsilon^e) + \overset{2}{\eta}(\xi)\right) + \overset{2}{e}(\varepsilon^e) + \overset{3}{e}(\xi) \tag{2.41}$$

$$\hat{\eta}(\varepsilon^e,\theta,\xi) = -\hat{\psi}_\theta = -\overset{1}{\psi}'(\theta) + \overset{1}{\eta}(\varepsilon^e) + \overset{2}{\eta}(\xi) \tag{2.42}$$

$$\hat{\sigma}(\varepsilon^e,\theta,\xi) = \rho_0\hat{\psi}_{\varepsilon^e} = \rho_0\left(\overset{2}{e}'(\varepsilon^e) - \theta\,\overset{1}{\eta}'(\varepsilon^e)\right) \tag{2.43}$$

$$\hat{e} = \hat{\psi} + \theta\hat{\eta} = \overset{1}{e}(\theta) + \overset{2}{e}(\varepsilon^e) + \overset{3}{e}(\xi) \tag{2.44}$$

The heat conduction equation now reduces to

$$k\nabla^2\theta + \rho_0 r + \sigma \cdot \dot{\varepsilon}^p - \rho_0 \overset{3}{e}'(\xi)\dot{\xi} - \rho_0 \theta \overset{1}{\eta}'(\varepsilon^e) \cdot \dot{\varepsilon}^e = \rho_0 c(\theta)\dot{\theta} . \tag{2.45}$$

2.1.8 Special Cases

Consider a uniaxial deformation process that is adiabatic, and further, that the elastic strain rate can be neglected in comparison to the plastic strain rate. Also, let the evolution equation for $\dot{\xi}$ be associated with the rate of accumulation of plastic strain, $\dot{\varepsilon}^p$. No detailed explanation or justification for this assumption will be given here, other than a mention that both quantities are related to the velocity of dislocations, and the reader is referred to Rosakis et al. (1997). Under these assumptions, the heat conduction equation (2.45) is further reduced to, denoting $\overset{3}{e}(\xi) = \overline{E}(\xi)$,

$$\begin{aligned} &\sigma \cdot \dot{\varepsilon}^p - \rho_0 \overline{E}'(\xi)\dot{\varepsilon}^p = \rho_0 c(\theta)\dot{\theta} \\ &\sigma \cdot \dot{\varepsilon}^p \left(1 - \frac{\rho_0 \overline{E}'(\xi)}{\sigma}\right) = \rho_0 c(\theta)\dot{\theta} \\ &\beta \sigma \cdot \dot{\varepsilon}^p = \rho_0 c(\theta)\dot{\theta} \end{aligned} \tag{2.46}$$

where the function β is interpreted as the fraction of plastic work available for heating. β can be determined, given the stated assumptions, from the thermal and mechanical fields

$$\beta = \frac{\rho_0 c(\theta)\dot{\theta}}{\sigma \cdot \dot{\varepsilon}^p} \tag{2.47}$$

2.1.9 Conclusions

The thermodynamic framework presented in this section provides a foundation for the experimental determination of the fraction of plastic work converted into heat. If suitable experiments are designed, one can use a simple equation, like (2.47) above, to

calculate the relative partition of plastic work into heat and stored energy. Even if certain restrictions, such as negligible thermoelastic power, are relaxed, the calculation of the relative fraction of dissipated energy is straightforward. In that case, the numerator would consist of the difference of heating rate and thermoelastic power.

Equation (2.46) gives an explicit model for the functional form of the β, the fraction of plastic work converted into heat. Since stress can depend on strain, strain rate, and temperature, rate dependence of β is determined directly from the rate dependence of σ. Internal energy in (2.46) is not a function of strain rate. Thus, the internal energy determined at one strain rate can be used to predict β at other rates, if stress is known.

2.2 Models for the Stored Energy of Cold Work.

Aravas et al. (1990) introduced a model for energy storage attributed to residual microstresses and the generation of dislocations in ductile metals. The model allows for a simple estimation of the fraction of stored energy from a uniaxial stress-strain curve, which is relevant to the current experimental study. Thus, a brief synopsis of the method will be given here. Small strain additive decomposition

$$\varepsilon = \varepsilon^e + \varepsilon^p \tag{2.48}$$

was assumed, and a generalized force, Q, and displacement, q, defined such that $\int_0^q Qdq = \int_0^Q qdQ$ represented the total work done by all applied forces. Relating this to the elastic and plastic work

$$\int_0^Q qdQ = W^e + W^p = \int_V \frac{1}{2}\sigma \cdot \varepsilon^e dV + \int_V \int_0^\sigma \varepsilon^p \cdot d\sigma \, dV \tag{2.49}$$

The model considered an elastic-perfectly plastic body undergoing non-homogeneous deformation. Figure 2.1 shows generalized load versus generalized displacement. The body deforms elastically up to point A, at which point the body yields. At loads above A, part of the body deforms plastically, and the load-displacement curve becomes non-linear. At maximum load B

$$\int_0^Q q dQ = W_B^e + \int_V \int_0^{\sigma_B} \varepsilon^p \cdot d\sigma \, dV \tag{2.50}$$

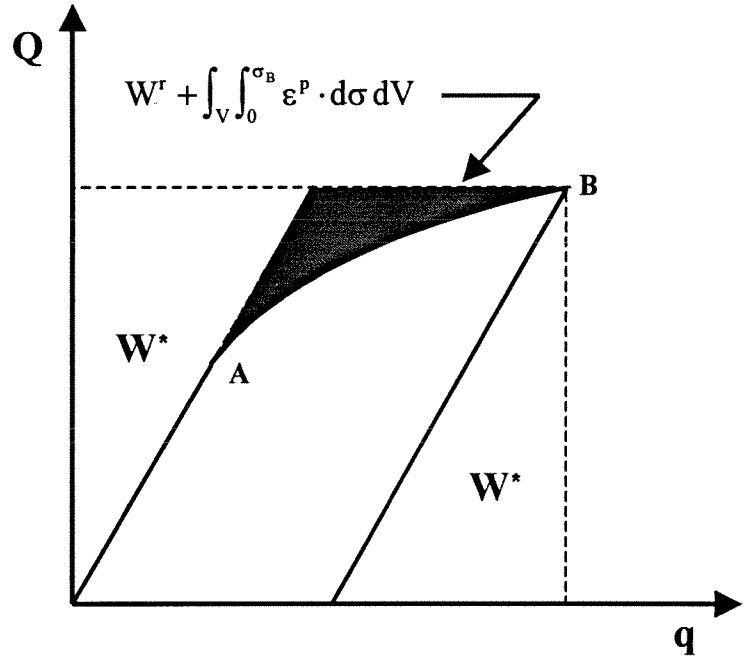

Figure 2.1 Generalized load-displacement curve used to determine the stored energy of cold work by a residual stress model.

If σ^* and ε^* are stresses and strains of an ideal linear elastic body at the same load, Q_B, then the residual stresses and strains at B are

$$\begin{aligned} \sigma^r &= \sigma_B - \sigma^* \\ \varepsilon^r &= \varepsilon_B - \varepsilon^* \end{aligned} \tag{2.51}$$

Using the principle of virtual work,

$$W_B^e = W^* + W^r \tag{2.52}$$

where W^* is defined in Figure 2.1,and

$$W^r = +\int_V \frac{1}{2}\sigma^r \cdot \mathbf{C}^{-1} \cdot \sigma^r dV \tag{2.53}$$

C is the fourth-order elasticity tensor. W^r is the energy stored in the material upon unloading, and is associated with residual stresses in the body. The relation for total work becomes

$$\int_0^Q q dQ = W^* + W^r + \int_V \int_0^{\sigma_B} \varepsilon^p \cdot d\sigma \, dV \tag{2.54}$$

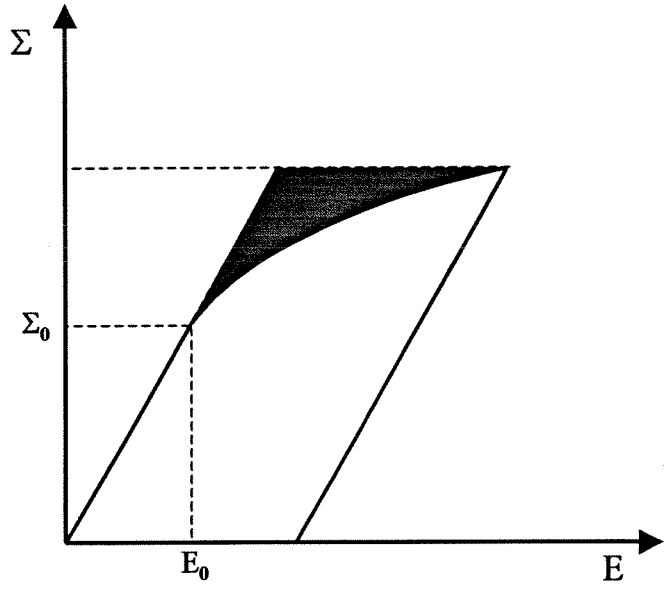

Figure 2.2 Example of uniaxial stress strain curve with exponential hardening used to determine the fraction of plastic work stored in the material.

For either proportional loading, or local elastic-perfectly plastic material behavior, the integral on the right vanishes identically. In either of these cases, the shaded region in Figure 2.1 is equivalent to W^r, or the total energy stored in the body. Even in cases where the integral does not vanish, the shaded region provides an upper bound for stored energy.

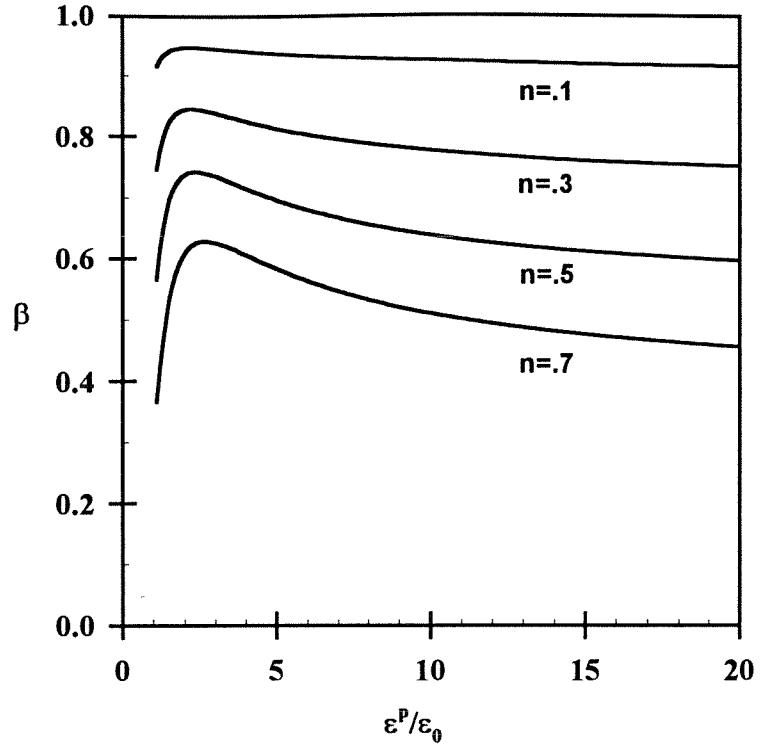

Figure 2.3 Fraction of plastic work dissipated as heat predicted by residual stress theory.

Aravas et al. applied the above concepts to deformation of a polycrystal. Each individual grain was composed of an elastic-perfectly plastic material. The uniaxial macroscopic stress and strain were analogous to the generalized load and displacement of the above discussion. The macroscopic stress was assumed to be linear in the elastic range, with exponential hardening after yield (Figure 2.2). Symbolically, the stress is written

$$\Sigma = \begin{cases} \Sigma_0 \, E/E_0 & \text{for } \Sigma \le \Sigma_0 \\ \Sigma_0 \left(E/E_0 \right)^n & \text{for } \Sigma > \Sigma_0 \end{cases} \tag{2.55}$$

where Σ_0 and E_0 are the macroscopic yield stress and strain, respectively. The ratio of energy stored to total work, f, can be calculated using (2.54)

$$f = \frac{An - (n+1)}{A - (n+1)} \tag{2.56}$$

where

$$A = 2\frac{\left(\frac{E}{E_0}\right)^{n+1} - 1}{\left(\frac{E}{E_0}\right)^{2n} - 1} \tag{2.57}$$

To coincide with the terminology of the previous section, the fraction of work converted into heat, β is equivalent to 1-f. The result of these calculations is given in Figure 2.3.

A different type of model, proposed by Zehnder (1990), actually takes into account the stored energy associated with dislocations in metals. Many of the original concepts of dislocation energies were discussed by Nabarro (1987). The model considers the simple, but instructive case of uniaxial deformation, with normal stress σ and normal strain ε, composed of elastic and plastic parts, i.e., $\varepsilon = \varepsilon^e + \varepsilon^p$. The parameter K, the ratio of the elastic modulus to the plastic tangent modulus, directly influences β, the fraction of plastic work dissipated as heat. In terms of stress, the plastic work rate can be written as

$$\dot{W}^p = \sigma\dot{\varepsilon}^p = \sigma\left(\partial\varepsilon^p / \partial\sigma\right)\dot{\sigma} = \frac{K}{E}\sigma\dot{\sigma} \tag{2.58}$$

The stress macroscopic stress is related to the stress required to move dislocations past one another, and hence allow plastic strain can be approximated

$$\sigma \sim \frac{\mu b}{r} \tag{2.59}$$

where μ is the shear modulus, b the Burger's vector, and r the average distance between dislocations ($= 1/\sqrt{N}$, N being the dislocation density). Differentiating and substituting into (2.58), assuming that μ and E are of the same order

$$\dot{W}^p \sim \mu b^2 \dot{N} K \tag{2.60}$$

The stored energy is assumed to be attributed to dislocation multiplication, e.g.,

$$\dot{W}^s \sim U\dot{N} \tag{2.61}$$

where U is the average energy of a dislocation, which has been estimated in many texts to be

$$U = \frac{\mu b^2}{4\pi} \ln\left(\frac{r/2}{r_0}\right) \tag{2.62}$$

r_0 is the core radius, estimated to be equal to b as a first approximation. Because of the logarithmic dependence on r, and thus N, it was argued that U is less sensitive to N, and

$$\begin{aligned} U &\sim \mu b^2 \\ \dot{W}^s &\sim \mu b^2 \dot{N} \end{aligned} \tag{2.63}$$

It follows that

$$\frac{\dot{W}^s}{\dot{W}^p} \sim \frac{1}{K} \tag{2.64}$$

and from the balance of energy

$$\frac{\dot{Q}}{\dot{W}^p} \sim \frac{K-1}{K} \tag{2.65}$$

Zehnder used this result and applied it to a power hardening material

$$\frac{\varepsilon^p}{\varepsilon_0} \sim \left(\frac{\sigma}{\sigma_0}\right)^N \tag{2.66}$$

Combining (2.65) and (2.66), the model reduces to

$$\frac{\dot{Q}}{\dot{W}^p} = \beta = \frac{N\left(\varepsilon^p / \varepsilon_0\right)^{\frac{N-1}{N}} - 1}{N\left(\varepsilon^p / \varepsilon_0\right)^{\frac{N-1}{N}}} \tag{2.67}$$

where N=1/n when compared to the previous model. Figure 2.4 is a plot of eq. (2.67) for various values of n.

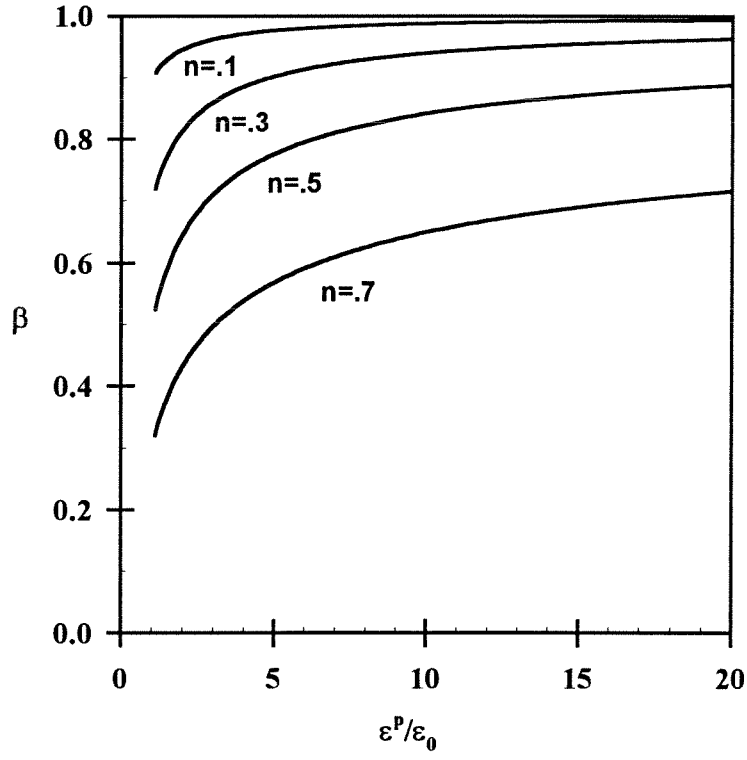

Figure 2.4 Fraction of plastic work dissipated as heat predicted by dislocation theory.

The two models described above do not predict equivalent functional forms for β, but provide some justification for including a strain dependence in the amount of plastic work dissipated as heat. The advantage of these approaches is that they can be applied

directly to uniaxial stress-strain curves, which forms the bulk of mechanical property tests in practice.

2.3 References

Aravas, N., Kim, K.S., Leckie, F.A. (1990), "On the Calculations of the Stored Energy of Cold Work," *J. Eng. Mat. Tech.*, **112**, 465.

Bridgeman, P.W. (1950), "The Thermodynamics of Plastic Deformation and Generalized Entropy," *Rev. Mod. Phys.*, **22**, 56.

Carlson, D.E. (1972), "Linear Thermoelasticity," in *Encyclopedia of Physics*, ed. Truesdell, Springer-Verlag, Berlin.

Coleman, B.D., Gurtin, M.E. (1967), "Thermodynamics with Internal State Variables," *J. Chem. Phys.*, **47**, 597.

Coleman, B.D., Mizel, V.J. (1964), "The Existence of Caloric Equations of State in Thermodynamics," *J. Chem. Phys.*, **40**, 1116.

Coleman, B.D., Noll, W. (1963), "The Thermodynamics of Elastic Materials with Heat Conduction and Viscosity," *Arch. Rational Mech. Anal.*, **13**, 176.

Fung, Y.C. (1965), *Foundations of Solid Mechanics*, Prentice Hall, New York.

Lubliner (1990), *Plasticity Theory*, Macmillan, New York.

Lubliner, J. (1972), "On the Thermodynamic Foundations of Non-Linear Solid Mechanics," *J. Non-Linear Mechanics*, **7**, 237.

Mandel (1972), *Classical Plasticity and Viscoplasticity*, Springer-Verlag, Vienna-New York.

Mandel (1973), *Int. J. Solids Struc.*, **9**, 725.

Nabarro, F.R.N. (1987), *Theory of Crystal Dislocations*, Dover Publications, New York.

Prigogine, I. (1947), in *The Study of Thermodynamics of Irreversible Processes*, Ed. Desoer, Dunod., Paris.

Rice, J.R. (1970), "On the Structure of Stress-Strain Relations for Time-Dependent Plastic Deformation in Metals," *J. Appl. Mech.*, **37**, 728.

Rice, J.R. (1971), "Inelastic Constitutive Relations for Solids: An Internal Variable Theory and its Application to Metal Plasticity," *J. Mech. Phys. Solids*, **19**, 433.

Rosakis, P., Rosakis, A.J., Ravichandran G., Hodowany, J. (1997), "On the Partition of Plastic Work into Heat and Stored Energy during Dynamic Deformations", to be submitted to *J. Mech. Phys. Solids*.

Truesdell, C. (1984), *Rational Thermodynamics*, Springer-Verlag, New York.

Truesdell, C., Toupin, R.A. (1960), "The Classical Field Theories," in *Encyclopedia of Physics*, ed. by S. Flugge, Springer-Verlag, Berlin.

Woods, L.C. (1982), "Thermodynamic Inequalities in Continuum Mechanics," *IMA J. of Appl. Math.*, **29**, 221.

Zehnder, A.T. (1990), "A Model for the Heating due to Plastic Work," *Mech. Res. Comm.*, **18**, 23.

CHAPTER 3

EXPERIMENTAL TECHNIQUES

3.1 Methods of Measuring the Stored Energy of Cold Work.

The techniques for measuring the stored energy of cold work can be separated into two broad categories: (1) In-situ methods, where measurements are made during deformation, and, (2) Post mortem methods, where the stored energy is measured after deformation.

In-situ methods rely on the direct application of the first law of thermodynamics. Work is determined from force-displacement data. The total work includes all elastic and plastic work, and all frictional work at the boundaries of the body. That is, all terms that contribute to changes in the internal energy of the body need to be considered. The heat produced during deformation can be measured from the increase in temperature of the deforming body. Calorimetric methods have also been used extensively, either by deforming a body inside a calorimeter, or by placing the deformed body into a calorimeter immediately after the deformation process. No real deformation process is ideally adiabatic, so the heat measure must be corrected for any heat lost during the process. Heat loss to the surrounding environment can occur by radiation, convection or conduction. Bever (1973) correctly argued that since heat and work are measured by different techniques, systematic errors in one do not automatically cancel systematic errors in the other. Therefore, to obtain accurate results in the calculation of stored

energy, the two quantities, work and heat, must be measured to a high degree of absolute accuracy.

Post deformation, or two-step, methods measure the stored energy by comparing the thermal behavior of a cold worked sample and a virgin sample. The virgin sample should be in the same state as the cold worked sample prior to cold working. Annealing methods can be used to release the stored energy of the cold worked sample. For anisothermal annealing, a constant rate of heat is applied to both samples, and the temperatures of each sample are recorded separately. Any release of stored energy will manifest itself by a temperature difference between the cold worked and virgin sample. Differential Thermal Analysis (DTA) and Differential Scanning Calorimetry (DSC) both fall under this category. For isothermal annealing, samples are placed in a constant temperature calorimeter, and the effect of the energy release is observed as a function of time. As the sample releases stored energy, it's temperature rises above that of the calorimeter. The difference between the temperatures is a function of the rate of release of energy. The primary disadvantage of isothermal calorimetry is that an amount of energy is lost in bringing the sample up to the temperature of the calorimeter. This error can be significant if energy is released below the isothermal annealing temperature. Reaction methods measure released stored energy by comparing reactions in a calorimeter. The principle is that a cold worked sample and a virgin sample will release different amounts of energy upon reaction with a third substance.

3.2 Measuring Mechanical Properties.

Typically, the quantity of energy given off as heat is measured independently of the total amount of expended energy. The total expended energy is generally calculated

from the product of forces and displacements. Thus, all loading apparatus must have the means to determine all relevant forces and displacements acting on a material sample.

3.2.1 MTS Hydraulic Test Apparatus.

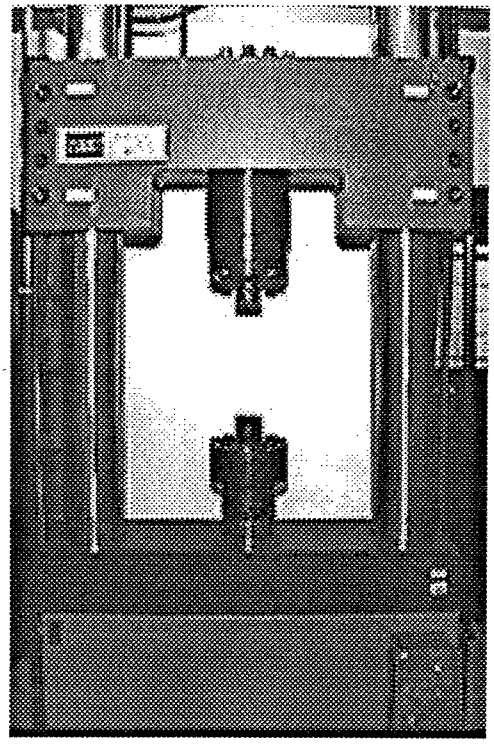

Figure 3.1 The MTS servo-hydraulic multi-axial load frame.

A Materials Test System (MTS Corporation, Minneapolis, Minnesota) Compression/Torsion load frame was used for axial compressive loading at strain rates below 1 s^{-1}. A photograph of the apparatus is shown in Figure 3.1. All experiments were run in displacement control, with load and displacement output recorded using a Nicolet 440 oscilloscope. To ensure pure, one-dimensional loading, a supplementary alignment fixture, shown schematically in Figure 3.2, was employed. Strain was calculated from the output of the built-in displacement transducer. The displacement transducer on the MTS was located at the bottom of the lower loading arm, so the output was corrected for

compliance of the load frame and alignment fixture. The compliance curve is generally non-linear, as seen in Figure 3.3.

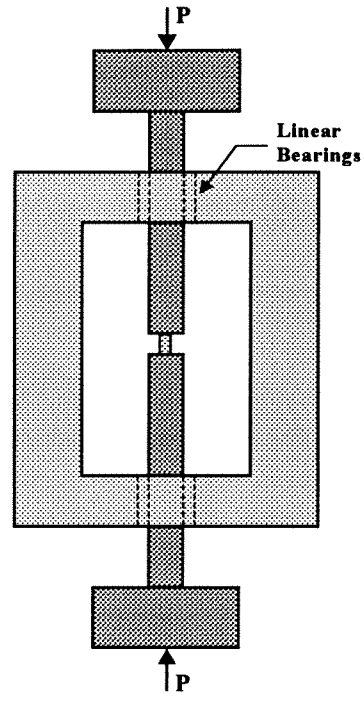

Figure 3.2 Alignment fixture used to obtain uniaxial compressive loads in the MTS load frame.

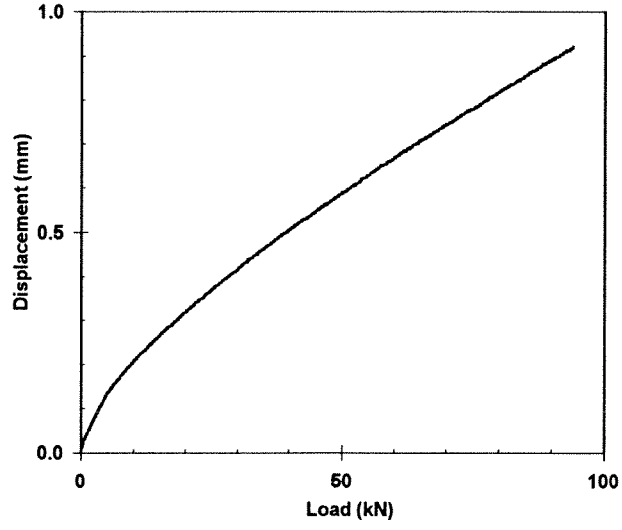

Figure 3.3 Typical compliance curve for the MTS load frame coupled with the alignment fixture.

3.2.2 Kolsky Bar in Compression

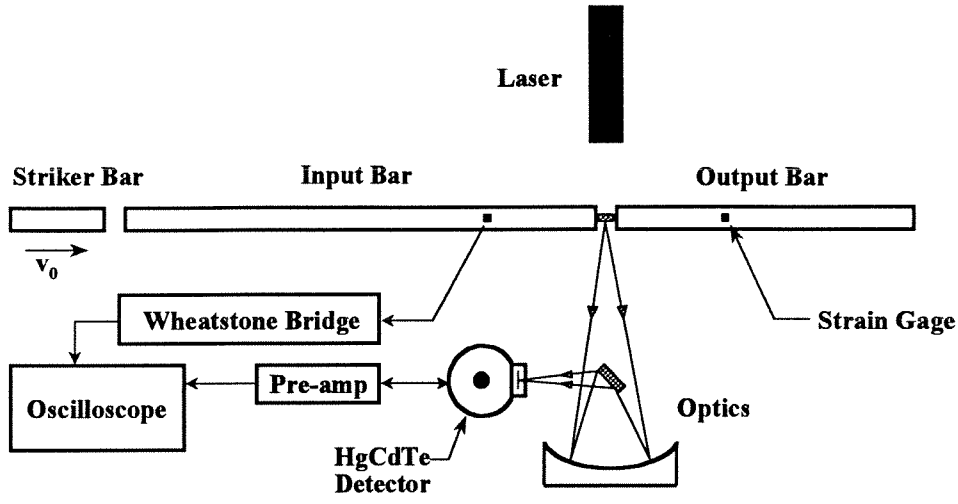

Figure 3.4 Kolsky bar in compression coupled with HgCdTe photoconductive detectors.

The Kolsky (split-Hopkinson) pressure bar is, by now, a well established apparatus for the high strain rate testing of ductile metals. Although there exist many references on this technique, see Lindholm (1964) and Follansbee (1985), a brief review will be given here. The apparatus consists of a striker bar, an input bar, and an output bar as in Figure 3.4, all of which are assumed to remain elastic during a test. A test sample of length L is placed between the input and output bars. When the striker bar impacts the input bar, an elastic stress pulse, with a rise time of approximately 10μs, propagates along the length of the input bar with velocity

$$c_0 = \sqrt{\frac{E}{\rho}} \tag{3.1}$$

where E is the Young's modulus and ρ is the density of the bar material. The duration of the pulse is

$$\Delta t = \frac{2L_{striker}}{c_0} \tag{3.2}$$

where $2L_{striker}$ represents round-trip travel of a one-dimensional longitudinal elastic wave in the striker bar. When the stress pulse reaches the test sample, a fraction of the original pulse is reflected back into the input bar, and the remaining fraction transmitted through the sample into the output bar. The relative fraction depends on differences in mechanical impedence between the input bar and sample. Strain gages, mounted on the input and output bars allow a time-resolved measure of strain in each bar. Kolsky (1949) showed that the nominal strain rate, $\dot{\varepsilon}(t)$, is given by

$$\dot{\varepsilon}(t) = -\frac{2c_0}{L}\varepsilon_R(t) \tag{3.3}$$

where $\varepsilon_R(t)$ is the reflected strain in the input bar. The strain in the sample can be calculated from (3.3) by integration.

$$\varepsilon(t) = \int_0^t \dot{\varepsilon}(\tau)\, d\tau \tag{3.4}$$

The nominal stress is calculated from the load in the output bar divided by the original sample area

$$\sigma(t) = \frac{A_0}{A} E\varepsilon_T(t) \tag{3.5}$$

where A is the undeformed area of the test sample, and $\varepsilon_T(t)$ is the time-resolved strain in the output bar of cross-sectional area A_0. The above results are based on the assumption that the test sample deforms homogeneously. The input and output bars are assumed to be composed of the same material, and of identical and uniform cross-sectional area. For any given situation, equations (3.3)-(3.5) are only accurate to the

extent that a measure of average stress and strain is adequate to define the state of stress and strain in the entire sample.

3.2.3 Kolsky Bar in Torsion.

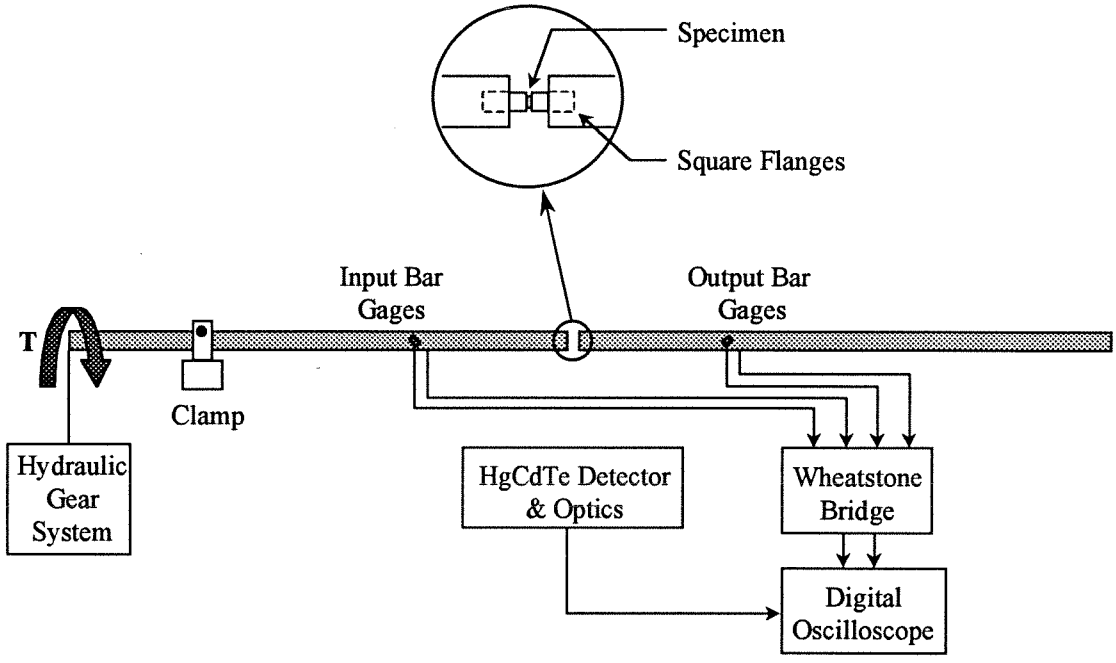

Figure 3.5 Kolsky bar in torsion .

For loading in torsion, a stored-torque Kolsky bar, a 25mm diameter bar made from 7075-T6 aluminum alloy, was used. The loading pulse was produced by the sudden release of a stored torque. This required a hydraulic actuated rack and pinion system to generate the torque, and a clamp positioned within a short distance to prevent free rotation of the bar (see Fig. 3.5). After the desired amount of torque was obtained, the clamp, made from 2024-T351 aluminum alloy, was fractured, which released a constant amplitude torsion pulse (rise time ~ 25 μs). The specimens used in the torsion Kolsky bar experiments were thin-walled tubes with integral flanges machined from plate stock (Fig. 3.5). Incident, reflected and transmitted signals (γ_I, γ_R, and γ_T respectively) were detected by two four-arm electrical resistance strain gage bridges mounted at 45° to the

bar axis, at equal distances from the specimen. From these signals, the shear stress and strain in the sample can be determined from

$$\dot{\gamma}(t) = \frac{2cD_s}{L_s D}\gamma_R(t) \tag{3.6}$$

$$\gamma(t) = \int_0^t \dot{\gamma}(\tau)d\tau \tag{3.7}$$

$$\tau(t) = \frac{\mu D^3}{8}\frac{\gamma_T(t)}{D_s^2 t_s} \tag{3.8}$$

where c is the shear wave speed, D is the diameter of the Kolsky bar, D_s, L_s, and t_s are the mean diameter, length, and wall thickness of the thin-walled specimen respectively, μ is the shear modulus of the Kolsky bar. In order to compare stress and strain values obtained in torsion to those obtained in compression, the equivalent stress and strain was used. According to Von Mises theory of plasticity, uniaxial stress and strain are related to stress and strain in simple shear by

$$\sigma^e = \sqrt{3}\tau \tag{3.9}$$

$$\varepsilon^e = \frac{\gamma}{\sqrt{3}} \tag{3.10}$$

where σ and ε are uniaxial stress and strain; τ and γ are the stress and strain, respectively. The torsion Kolsky bar has several advantages including a loading pulse free from dispersion effects and the ability to deform samples to large plastic strains. The primary disadvantage of the technique is the possibility of superimposed bending waves on the torsion pulse, which can corrupt strain signals measured on the bar surfaces. A detailed background and analysis of the torsion Kolsky bar is given by Hartley and Duffy (1990).

3.3 Temperature Measurement and Infrared Photon Detectors.

There exists several types of transducers available for the measurement of temperature, each having relative advantages and disadvantages. Temperature transducers fall into several broad categories: (1) thermistors, or technology based on materials whose electrical impedance changes with temperature, (2) thermocouples and thermopiles, whose technology is based on the Seebeck effect, (3) instruments which rely on the direct heat transfer to the transducer, and (4) photon detectors, which are semi-conducting devices that produce charge carriers when excited by photons having energies within a range of wavelengths, which depends on the particular semiconductor. Important factors which influence the choice of temperature transducer are temperature and time resolution, expected temperature range, materials involved in the experiments, ease of implementation, and cost. Photon detectors have high speed response, and thus, are particularly suitable for short time events. Also, they measure temperature remotely. The disadvantages are higher cost, and relative difficulty in calibration.

Since photon detectors were used in this investigation, a discussion of their characteristics and performance will be presented here. As mentioned above, photon detectors are semi-conducting devices that produce resistance changes when excited by photons of certain wavelengths, which depends on the detector material. The detector can be photovoltaic (photodiode), which utilizes a p-n or p-i-n junction to convert radiant power directly into electric current, or photoconductive, which changes conductivity as a function of radiant power. All bodies above absolute zero emit electromagnetic radiation. The spectral distribution of electromagnetic energy varies with the temperature of the body. The choice of detector material depends on the temperature range expected in

experiments, which determines the wavelength range of emitted electromagnetic radiation.

A single, photoconductive HgCdTe photon detector, whose responsivity was maximum between wavelengths of 8-12 μm, was used for the present study. This wavelength range was chosen to match the peak spectral power distribution of a body between 300-400 K, the range of temperatures expected during the Kolsky bar experiments. HgCdTe is a ternary semiconductor compound which exhibits a wavelength cutoff proportional to the alloy composition (EG&G, 1994). The actual detector is composed of a thin layer (10-20 μm) of HgCdTe with metal contact pads defining the active area. Photons with energy greater than the semiconductor band-gap energy excite electrons into the conduction band, thereby increasing the conductivity of the material. The wavelength of peak response depends on the material's band-gap energy, which can be changed by varying alloy composition. To sense the change in conductivity, a bias current or voltage is required. Typically, detectors are manufactured in a square configuration to maintain a uniform bias current throughout the active region. The detector element configuration is shown in Figure 3.6.

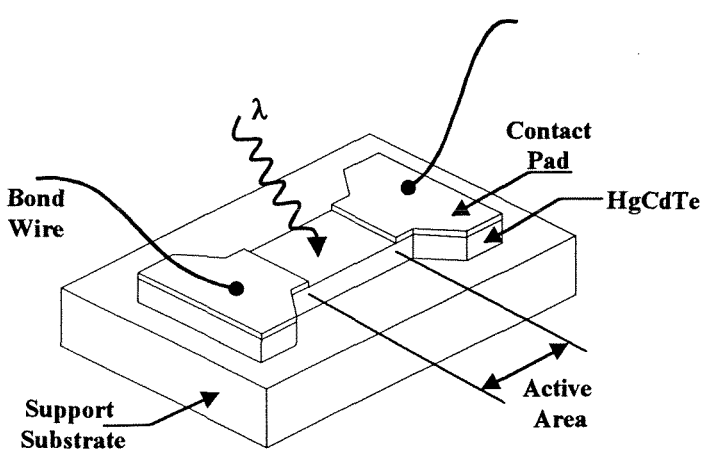

Figure 3.6 Schematic of single HgCdTe photoconductive detector element.

Since only a single detector was used, temperature could only be measured at a "point," or small area. The size of the area depends on the active area of the detector, which was 100 μm by 100 μm square, and the associated optics, which will be discussed below.

In general, the speed of infrared detector system is not limited by the detector element, but rather on the electronics associated with it (Zehnder and Rosakis, 1993). The circuit for amplifying the photoconductive HgCdTe detector is shown in Figure 3.7 (EG&G, 1994). The detector is a low impedance device, typically 10-150 Ω, and requires a low voltage noise preamplifier. A constant bias current is produced in the detector using a low noise DC power supply with a current-limiting resistor, R_B. The detector element changes resistance in response to incident photons, and the resulting voltage is amplified by the preamplifier. An AC coupling capacitor blocks the DC bias voltage from the high gain preamplifier and prevents DC saturation. The amplifier had a bandwidth specification of 5Hz to 1MHz. The detector/amplifier combination, which included a custom feedback resistor for optimum performance, had a peak cutoff closer to 2MHz.

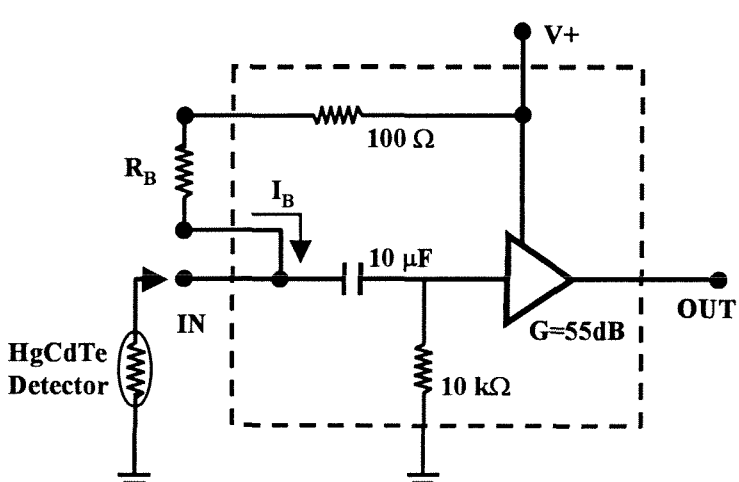

Figure 3.7 Basic operating circuit for photoconductive detectors.

3.4 Infrared Optics.

Electromagnetic radiation is emitted from a surface in all directions. To optimize the infrared detector system for use as a temperature measuring device, a means of bringing radiation from a surface to the detector must be devised. Merely placing the detector in front of an emitting body is a possibility, but by no means is it an efficient method of gathering the radiation. In general, some type of designed optics is used in conjunction with the infrared detector to efficiently gather radiation from the surface of a body. The optical system, similar to those for visible light, can make use of refractive or reflective optics.

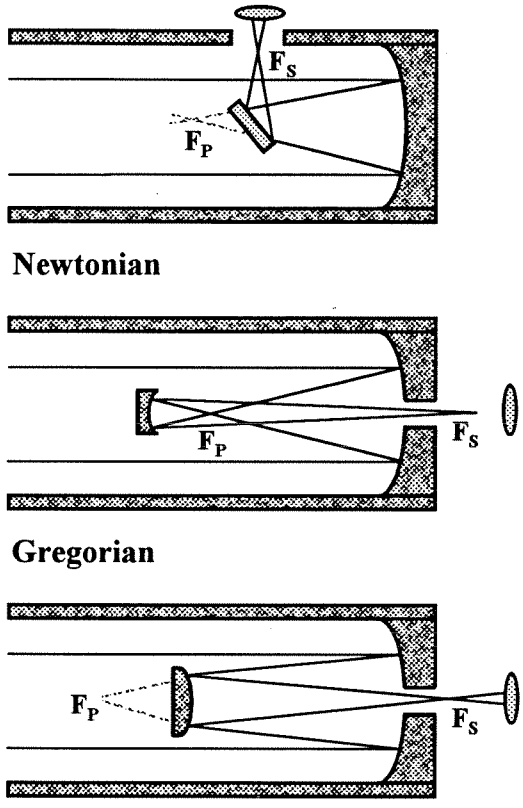

Figure 3.8 The three basic catoptric telescopes

For a refractive system, lenses must be able to transmit radiation from the object plane to the image plane. Optical materials for use within infrared wavelengths include ZnSe, Ge and Si. The primary advantage of refractive infrared optics is that the optical path is straight. The main disadvantages are the high cost for larger diameter lenses, high chromatic aberrations, and the inability to focus the system using visible light.

Reflective IR optical systems have several advantages over refractive systems. Visible light can be used to focus the system. Chromatic aberrations are eliminated.

Furthermore, mirrors can be made larger than lenses for equivalent cost. With mirrors, the transparency and optical homogeneity of the material are of no concern – only the quality and shape of the reflective surface matter. The three principal coatings for IR optical reflectors are gold, silver and aluminum. Although the reflectivity of these coatings is a function of wavelength, and in general, is not constant, the coatings provide good reflectivity over most IR wavelengths. The variation in reflectivity can be accounted for in the calibration, which is discussed in the next section.

Most IR optical systems are a variation of one of the basic catoptric telescopes shown in Figure 3.8. Zehnder and Rosakis (1991) and Mason, Rosakis, and Ravichandran (1993) used an Offner optical system, which is a modification of the Cassegrain telescope, for their temperature measurements. The Offner system is useful when imaging at 1:1 magnification. It consists of two spherical mirrors located such that their centers of curvature are coincident. This system does an excellent job eliminating spherical aberrations, but is limited to unit magnification, which may not be suitable for all applications. The Newtonian system allows for easy adjustment of magnification, and was used as the basis for the optical system used in the present investigation. One has to live with the aberrations, however, this is of less concern when using a single infrared detector. Duffy et al. (1971) used a modification of the Newtonian telescope to measure temperature evolution in shear bands. Detailed information on infrared optics is given in Wolfe and Zissis (1978).

3.5 Integrating Mechanical Testing and In-Situ Temperature Measurement.

To calculate the fraction of plastic work converted into heat, the temperature measurement device was integrated with the loading devices mentioned above. Accurate results depended on resolving certain issues involved in integrating thermal and mechanical measurement. Since plastic deformation and heat evolution are intimately coupled phenomena, measurement of one requires a thorough knowledge of the other. For example, when measuring temperature, one needs to know the underlying state of stress in the body. Infrared photon detectors provide an average temperature measure of a small, finite area of a body. This area could include regions of non-uniform stress and strain, and thus a non-uniform spatial temperature field. Likewise, a body with non-uniform temperature may cause anomalous measures of stress and strain.

3.5.1 Dynamic Compression and Torsion.

As described above, the Kolsky bar, both in compression and torsion, provide a measure of average stress and strain rate in a cylindrical sample. Furthermore, if the sample is homogeneous, and undergoes a homogeneous deformation, then the average stress and strain rate provided by equations (3.3) and (3.5) represent the actual strain rate and stress at all points in the sample.

In reality, only single crystals with no inclusions will have spatial uniformity of stress and strain rate. For polycrystalline samples, active slip planes will be oriented randomly due to the random orientation of the grains. The resolved shear stress for the slip planes of a particular grain volume will necessarily be different from that of neighboring grains. This is a mute point from the perspective of macroscopic continuum

mechanics, which will average the effects over large number of grains. However, when measuring temperature, one must at least consider the deformation on a smaller scale. The length scale of the HgCdTe detector described above is 100 μm. For many metal polycrystals, the grain size is on the order of tens of microns. If using unit magnification infrared optics, the temperature measure will be an average over a small number of grains, which can lead to anomalous results if this temperature is extrapolated over the entire sample dimensions. Inclusions and 2^{nd}-phase particles can also contribute to local gradients of stress, strain and temperature. Again, the important factor is the length scale over which these gradients are introduced. If a large enough area is considered, these local effects are averaged, and a reasonable assessment of the material behavior can be obtained.

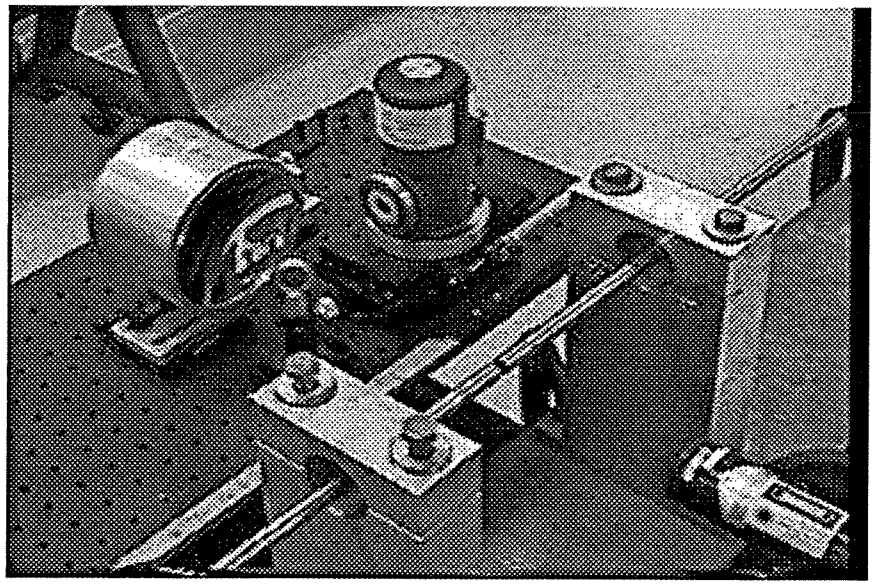

Figure 3.9 Photograph of the dynamic compression setup.

The experimental setup for dynamic compression is shown in Figure 3.9. The detector is focussed onto the sample face by using heated wires placed in the same plane as an actual test sample. The cross-wire fixture is sketched in Figure 3.10. After

confirming the focal position, the intersection of the heated wires is marked remotely by the laser. This assures positional repeatability between tests.

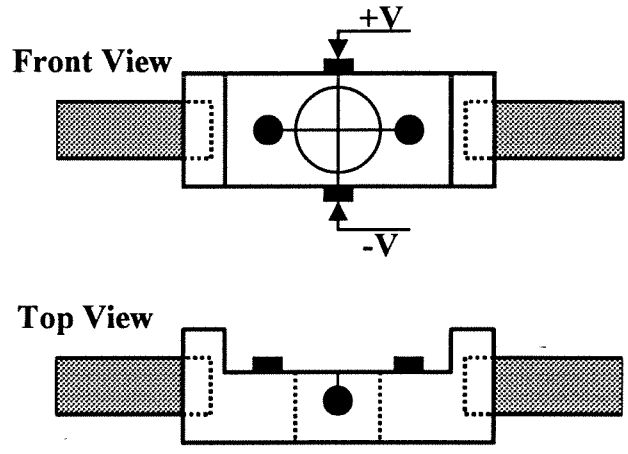

Figure 3.10 Device used focus detector element onto the center of a compression sample. Detectors were focussed on heated cross-hairs.

The setup for dynamic torsion experiments is very similar to that in compression. The procedure of temperature measurement for both loading mechanisms is identical. The differences in measuring the mechanical fields were discussed previously. The plastic strains obtained in the torsion Kolsky bar are, in general, much larger than those obtained in compression. For most materials, this additional plastic strain can lead to a pronounced increase in surface roughness which tends to increase the emissivity of the surface.

3.5.2 Large-strain Dynamic Experiments in Compression.

One drawback of the Kolsky bar in compression is the inability to obtain large plastic strains during a test. In addition, accumulation of plastic strain in compression can produce large changes in surface roughness and color.

To obtain larger plastic strains in compression, a technique of recovering and reusing the samples was employed. The reflection of input stress waves from the free

end of the input bar can cause repeated loading of the sample. To avoid repeated loading during one test, a short output bar was used. In this configuration, the tensile stress wave that results from reflection from the free end of the output bar will cause the output bar to pull away from the sample, ending the test before a second loading (Chen and Ravichandran, 1996). For a given sample, the dimensions before and after testing were recorded. The sample was then re-machined, resulting in a sample of the same diameter and surface finish as that prior to testing. The re-machined sample was then re-tested with a known initial value of plastic strain. This process was repeated until the desired value of plastic strain was attained. This technique works especially well with rate insensitive materials, since any strain rate differences between tests would be inconsequential. However, the technique will also work with rate sensitive materials if the strain rates are carefully duplicated for each subsequent test in the sequence.

3.5.3 Quasi-Static Compression with Temperature Measurement.

Mechanical tests at low strain rates often are nearly isothermal. The particular strain rate below which the deformation process can be considered isothermal depends on the thermal properties of the material and specimen geometry. There also exists a range of strain rates where the deformation process is neither isothermal nor adiabatic, and all terms of the heat conduction equation must be addressed. It turns out that for some materials, deformations at the highest strain rates achievable on the MTS servo-hydraulic load frame are nearly adiabatic. Titanium and steel, for example, have relatively low thermal diffusivity, and can be deformed adiabatically on the MTS. Even aluminum alloys, despite a high thermal diffusivity can be deformed adiabatically, if a suitable sample geometry is defined.

Integrating the infrared detector system with the MTS load frame is problematic. The pass band of the detector and amplifier rejects low frequency signals. For plastic deformation of metal samples in the Kolsky bar, the temperature rise is rapid enough for the detectors system to pass the entire signal. This is not true, even for a relatively high strain rate, for deformation in the MTS load frame. The test duration is at least four orders of magnitude slower in the MTS than in the Kolsky bar.

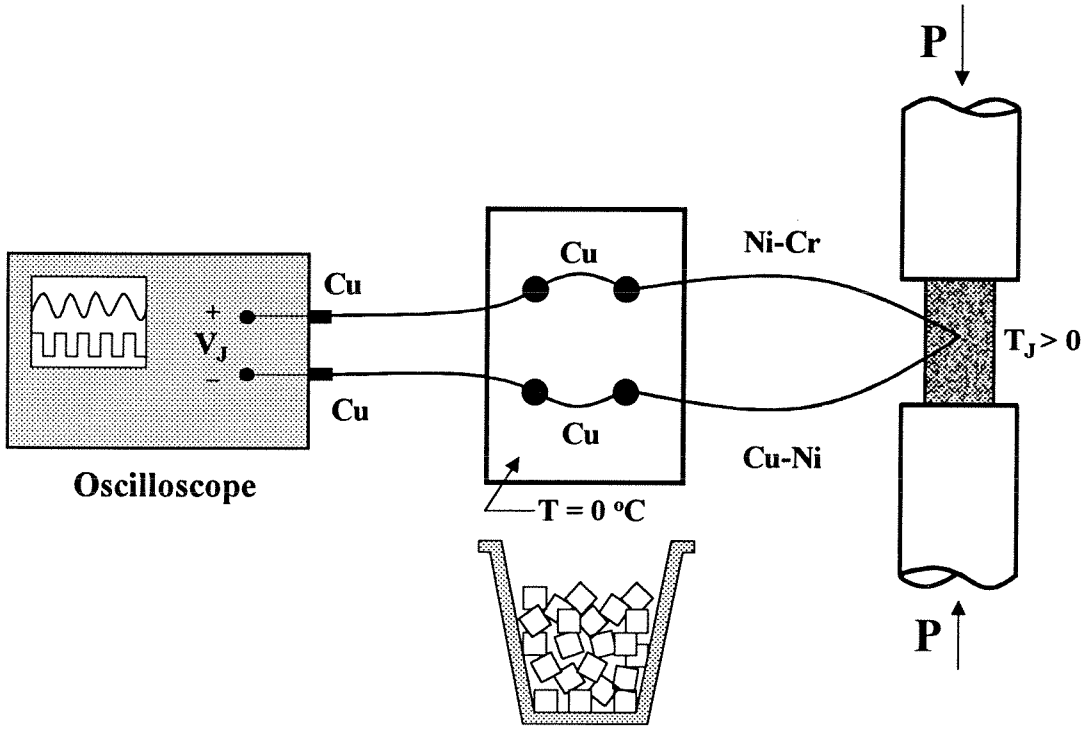

Figure 3.11 Diagram of experimental setup used to measure the in-situ temperature changes of metals deforming at lower strain rates

Instead, a fast, E-type thin wire thermocouple was used to measure temperature changes in the MTS load frame. The diameter of the thermocouple wire was 25 μm. Voltage changes produced by the thermocouple were registered directly on the Nicolet oscilloscope. The lead wires on the thermocouple could not simply be connected to the terminals of the oscilloscope, since the connections at terminals would produce measurable voltages. The internal wires of the oscilloscope were made of copper. The

equivalent thermocouple circuit of Figure 3.11 was used instead. The thermocouple was bonded to the center of the metal sample using silver contact cement. The presence of the cement did not alter the thermocouple circuit, since only the temperature at the junction is recognized. The thermocouple lead wires were attached to copper lead wires, and these were placed into a 0 °C ice bath. The copper wires were then connected to the oscilloscope terminals. For this circuit, the only voltage was produced by the junction at the specimen surface. The 0 °C junctions did not produce a voltage, nor do the same-metal junctions at the oscilloscope terminals.

The time response of the E-type thermocouple was approximately 1 ms. This was determined by placing the thermocouple junction in 100 °C water. This was an upper bound for the response time, in a sense, since only a fraction of the surface area of the thermocouple is in contact with the sample during a test in the MTS. At 100 °C, as seen in the figure, the voltage produced was between 6 and 7 mV. The highest voltage resolution on the Nicolet oscilloscope is on the order of 0.5 μV. For many metals, the test duration must be less than 1 second to achieve a near adiabatic deformation process, so one could expect to obtain a temperature signal containing several hundred points.

3.6 Calibration Issues.

Perhaps the most important experimental issue was the calibration of the infrared detectors. The accuracy of the test results depended directly on the accuracy of the calibration. The premise is as follows: the output from the detector is always in the form of a voltage. In order to use the detector to measure the temperature of a test sample, the functional relationship between detector output voltage and the temperature of the body must first be ascertained. In principle, the calibration can be performed analytically or

experimentally. To do so analytically, one would need detailed knowledge of certain physical parameters, including specimen emissivity, medium transmissivity, and sensitivity and spectral responsivity of the detectors. Accurate measurement of emissivity over a wide range of temperatures makes the analytical approach quite challenging.

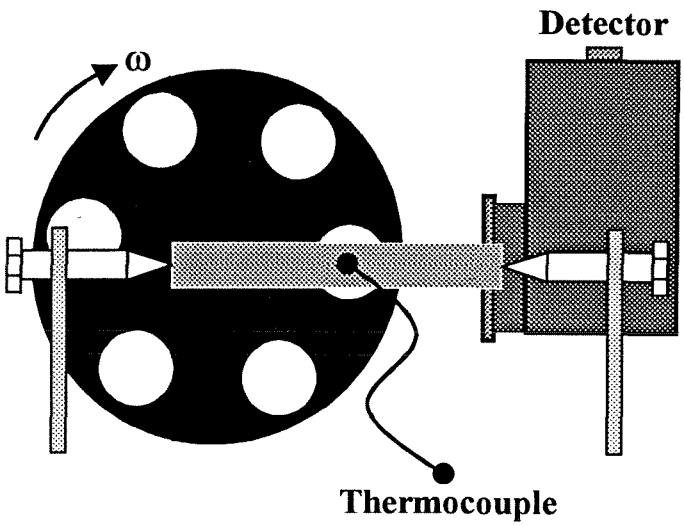

Figure 3.12 Setup used to calibrate the HgCdTe infrared detector for analyzing data from the compression Kolsky bar. A similar setup was used to calibrate for the dynamic torsion experiments, with a slightly modified specimen geometry.

For all tests included here, an experimental approach to calibration was adopted. The general rule of any experimental calibration can be succinctly stated as: *one should always, to the extent possible, reproduce the conditions of an actual experiment when performing calibrations.* Many calibration configurations were tested, but the one eventually used to analyze the experimental data closely mimicked the conditions of an actual Kolsky bar experiment. This configuration is shown in Figure 3.12. After a series of Kolsky bar tests, without moving the position of the detector and optics, a cylindrical sample was placed in the same location as an actual test specimen. The calibration specimen was held in place by a holding fixture, designed to minimize conductive heat

transfer from the specimen ends. The laser was used to position the calibration specimen, similar to an actual test. On the lateral side furthest from the detectors, a K-type thermocouple was placed into a pre-machined slot, and held in place by a set screw of the same material as the calibration specimen. The calibration specimen was then removed, placed in a furnace to raise it's temperature above the expected maximum temperature of an actual test, and returned to the holding fixture. Since the HgCdTe and pre-amplifier were only sensitive to AC signals, a chopping wheel was placed between the specimen and detector. The frequency of the chopped signal was well within the pass band of the detector and amplifier. The chopping wheel served a two-fold purpose: creating an AC signal, and providing an aperture to limit radiation from unwanted parts of the specimen. During one chopping period, the detector sees a half-period of chopping wheel and a half-period of calibration specimen. An example of the output from the detectors at two different temperatures is given in Figure 3.13.

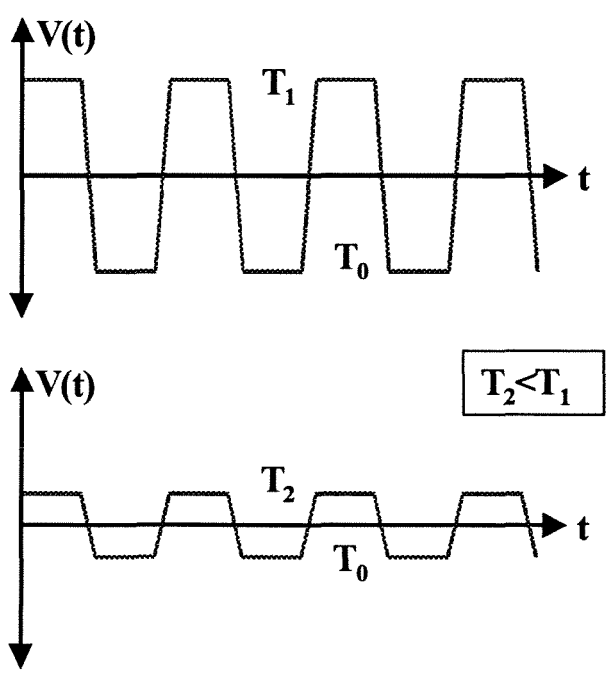

Figure 3.13 Traces obtained during calibration at two different temperatures.

Since the temperature of the chopping wheel remains constant, changes in signal for the specimen are determined using the signal from the chopping wheel as a reference (see Figure 3.12). As the specimen cools, several temperature-voltage pairs are recorded, using the output from the thermocouple and detector, respectively. A typical result is shown in Figure 3.14. The temperature-voltage pairs are then fit with a 2^{nd}-degree polynomial, which does an excellent job over the range of temperatures of a typical calibration cycle. The coefficients of the fit are used to convert experimental detector voltage signals into temperature signals.

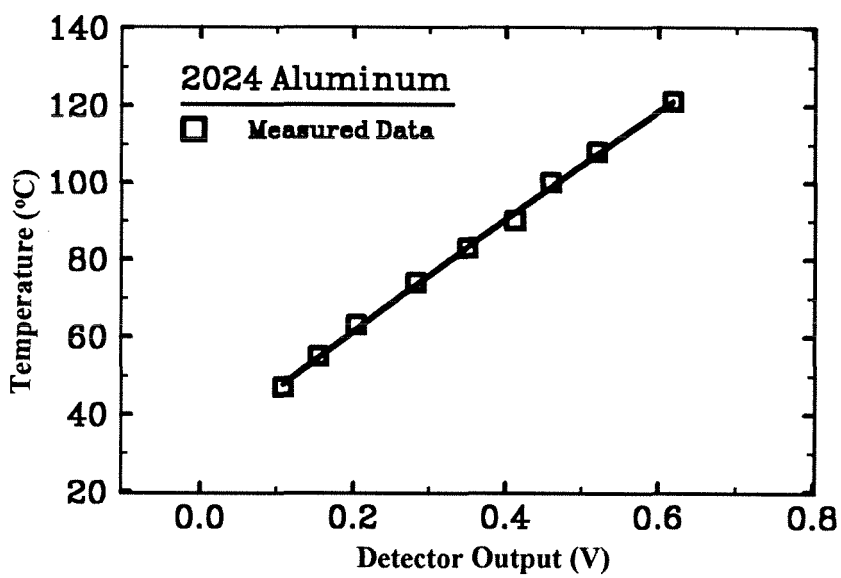

Figure 3.14 A Typical calibration curve.

The surface roughness for some metals, such as aluminum alloys, can change dramatically during deformation. This has implications on the validity of calibrations performed on virgin samples, if they are subsequently applied to entire test. As an example, Figure 3.15 shows three calibration curves plotted on the same axis. Three different aluminum samples were calibrated, each representing different levels of deformation. Initially, each sample was in the annealed condition, and had smooth,

machined surfaces. One sample was calibrated in this state. The remaining two were subjected to 15% and 25% plastic strain, respectively, and then calibrated in the deformed state.

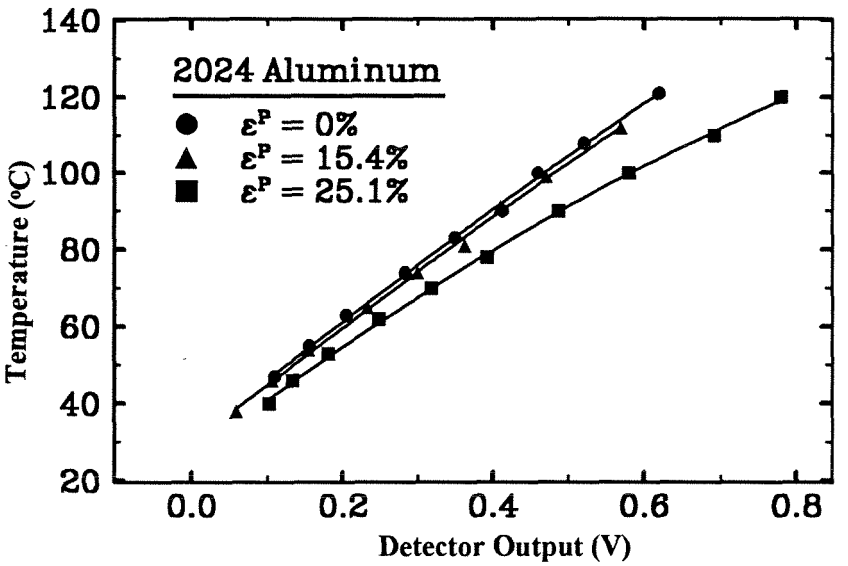

Figure 3.15 Three calibration curves, each with varying surface roughness due to residual plastic strain.

Out to 15% strain, the calibration curves were nearly identical. The sample with 25% residual strain gave a higher output for each temperature. This effect became more pronounced at higher temperatures. This is due to an increase in emissivity associated with an increase in effective surface area of a rough sample. This type of curve, which was produced for each material used in the present investigation, gave some indication of the validity of the calibration curves over a range of strains. Aluminum, however, is an extreme example of this effect. Compared to most metals, the surface quality of aluminum alloys is particularly sensitive to strain. The technique, described above, for remachining and reloading a sample has an added advantage of extending the validity of calibrations over larger strains.

3.7 Limitations in Accuracy.

3.7.1 Heat Transfer during Mechanical Loading

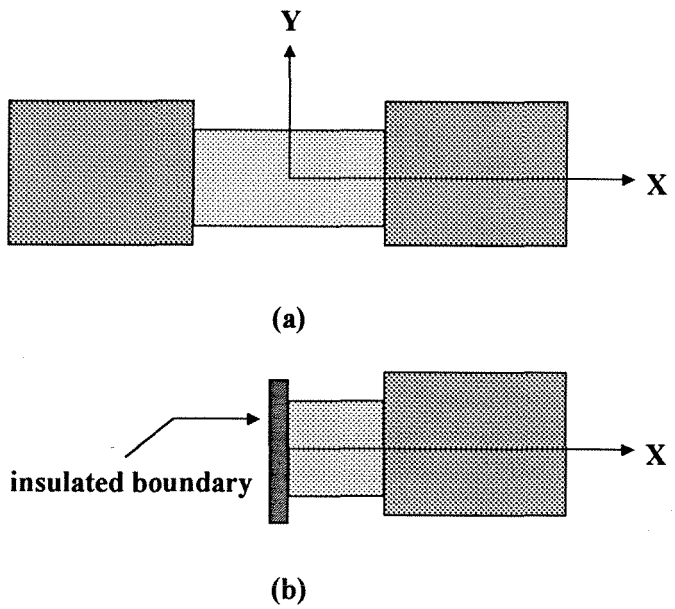

Figure 3.16 Schematic of a metal sample sandwiched between two elastic bars used in a theoretical heat transfer analysis.

During the deformation of metals, heat transfer from the sample to the loading medium is inevitable. Over a short enough time scale, the process can be considered nearly adiabatic for the purposes of analyzing the resultant temperature rise in the sample volume. Using a one-dimensional, unsteady heat transfer model, the relative error in assuming adiabatic deformation processes will be approximated. Picture a metal sample placed between two steel bars as in Figure 3.16(a). Because of symmetry, Figure 3.16(b) is equivalent to Figure 3.16(a), where the left boundary is now insulated. Material 1 has cross-sectional area A_1, and material 2 has cross-sectional area A_2. If we assume a constant source term, negligible convection, a length scale L, and a characteristic temperature θ_0, the equation representing heat conduction, in non-dimensional form, is

$$\frac{\partial^2 \Theta}{\partial X^2} - \frac{\partial \Theta}{\partial \tau} = -\Phi \tag{3.11}$$

where

$$\Theta = \frac{\theta}{\theta_0}$$

$$\tau = \frac{\alpha t}{L^2} = \frac{t}{\tau_0}$$

$$\tau_0 = \frac{L^2}{\alpha} \tag{3.12}$$

$$X = \frac{x}{L}$$

$$\Phi = \frac{\phi L^2}{k\theta_0}$$

are the dimensionless temperature, time, characteristic time, distance, and constant source term, respectively. In the above expressions, k is the thermal conductivity, and α, the thermal diffusivity. The heat conduction equation is subject to the following boundary conditions for the current problem

$$\frac{\partial \Theta}{\partial X} = 0 \qquad X = 0 \tag{3.13}$$

$$k_1 A_1 \frac{\partial \Theta_1}{\partial X} = k_2 A_2 \frac{\partial \Theta_2}{\partial X} \qquad X = 1 \tag{3.14}$$

$$\Theta_1 = \Theta_2 \qquad X = 1 \tag{3.15}$$

$$\Theta_2 \to 0 \qquad X \to \infty. \tag{3.16}$$

The second boundary condition requires that the heat into and out of the specimen-bar interface be equal. The third condition does not allow a temperature jump at the boundary. However, this condition assumes perfect thermal contact between the specimen and the bar. Actual surfaces are rough, and supply a resistance to heat transfer.

Only a fraction of the cross-sectional area of the specimen is available for heat conduction (Ozisik, 1985). Heat must be transferred by convection over the remaining area. The relative area in contact with the bar is a function of pressure. At higher pressures, the area available for conduction increases, thus, the resistance to heat transfer across the interface decreases.

Ozisik (1980) gives a solution for the temperature in material 1 of Figure 3.16(b), normalized by the adiabatic temperature rise

$$\frac{\Theta_1(X)}{\Theta_{ad}} = \frac{1}{\tau}\int_0^{\tau} \Theta_1^*(X, \tau - s)\, ds \tag{3.17}$$

where

$$\Theta_1^*(X,\tau) = 1 - \frac{1-\gamma}{2}\sum_{i=0}^{\infty}\gamma^i\left\{\operatorname{erfc}\left[\frac{2n+1+X}{2\sqrt{\tau}}\right] + \operatorname{erfc}\left[\frac{2n+1-X}{2\sqrt{\tau}}\right]\right\} \tag{3.18}$$

$$\gamma = \frac{k_1A_1 - k_2A_2\mu}{k_1A_1 + k_2A_2\mu} \tag{3.19}$$

$$\mu = \sqrt{\frac{\alpha_1}{\alpha_2}}\,. \tag{3.20}$$

Equation (3.17) provides a simple means to compare the importance of heat conduction over various time scales. Table 3.1 gives material properties and characteristic times for steel, aluminum alloy and pure α-titanium. Steel is commonly used as the loading medium – material 2 in the analysis. 2024 aluminum and α-titanium will be used as examples for material 1. The samples used in the Kolsky bar were typically right cylinders of 6.35 mm diameter and 6.35 mm length. In the MTS, for purposes of measuring temperature, the samples had a diameter of 6.35 mm, and a length of 10 mm.

Therefore, the characteristic times, τ_0, for Kolsky bar tests and MTS tests were not equal, and are denoted separately in Table 3.1.

Table 3.1 Thermal properties and characteristic times for three metals.

	Steel	α-Titanium	2024 Aluminum
k (W/m·K)	34.6	18.8	151
α ($x10^{-6}$ m^2/s)	9.86	7.7	63
γ	-	-0.73	-0.4
τ_0 (s), for Kolsky bar	-	1.3	0.16
τ, for Kolsky bar	-	$7.64x10^{-5}$	$6.25x10^{-4}$
τ_0 (s), for MTS	-	13	1.59
τ, for MTS	-	$3.8x10^{-2}$	0.315

The result of numerically integrating equation (3.17) for several normalized time scales, τ, is given in Figure 3.17 for titanium and Figure 3.18 for 2024 aluminum. For tests in the Kolsky bar, there is no question that the deformation is nearly adiabatic for both metals. Only near the specimen-bar interface is conduction important. This is a conservative estimate, since the actual specimen and bar have rough surfaces and heat transfer does not occur over the entire area of the bar, as assumed. For tests in the MTS, end effects are more pronounced. Still, if temperature is measured near X=0 – at the center of the sample – one can assume that the error in assuming adiabatic conditions is small.

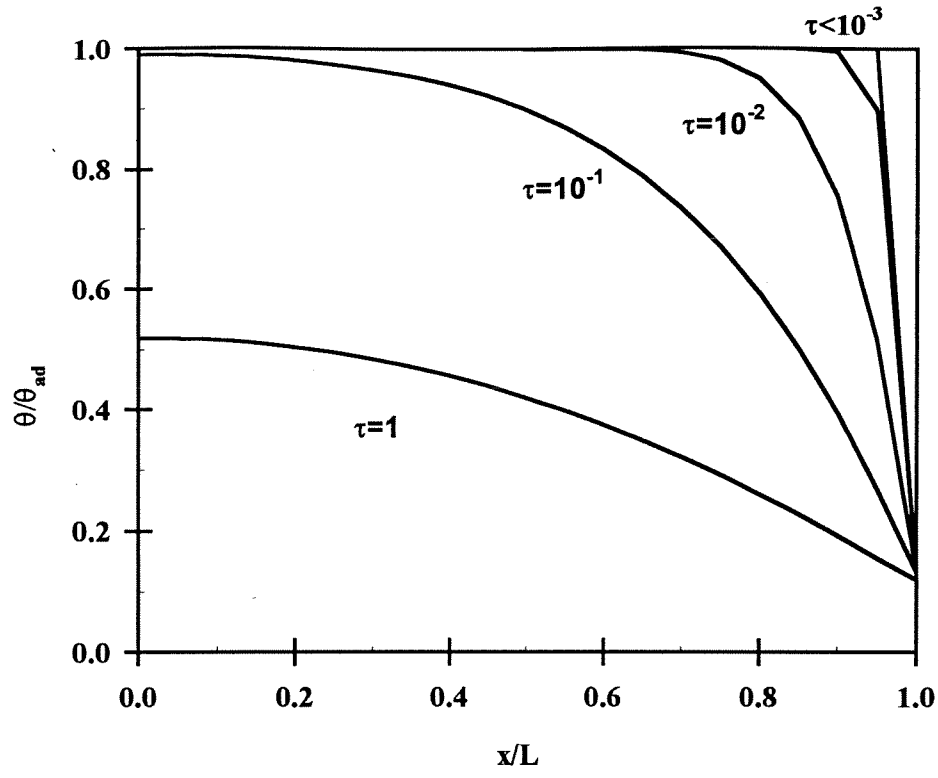

Figure 3.17 Heat transfer in titanium sample.

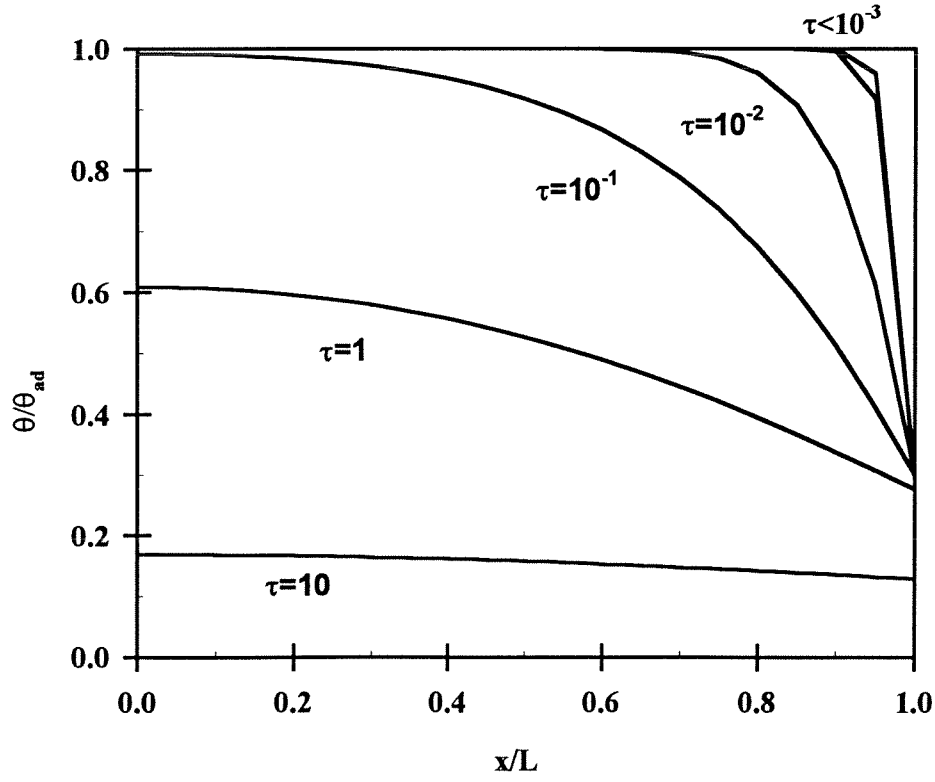

Figure 3.18 Heat transfer in 2024 aluminum sample.

3.7.2 Validity of Experimental Assumptions

Calculating the stored energy of cold work using the method outlined above relies on certain basic assumptions.

- *Homogeneous deformation*

Equations (3.3) and (3.5) from the Kolsky bar are average measures of stress and strain rate, based on load applied by, and relative motions of, the ends of the bar in contact with the sample. If the sample deforms homogeneously, then the average measure of stress and strain rate is an excellent approximation of stress and strain rate at every material point in the sample. In the case that stress and strain are not uniform in the sample, one can still use the Kolsky bar analysis to calculate total input power. However, temperature is measured over a fraction of the sample surface, and is in fact an average measure of temperature over that area. To calculate β, the fraction of plastic work available as heat, the calculated plastic power must be an accurate average measure of plastic power over the area where temperature information is collected.

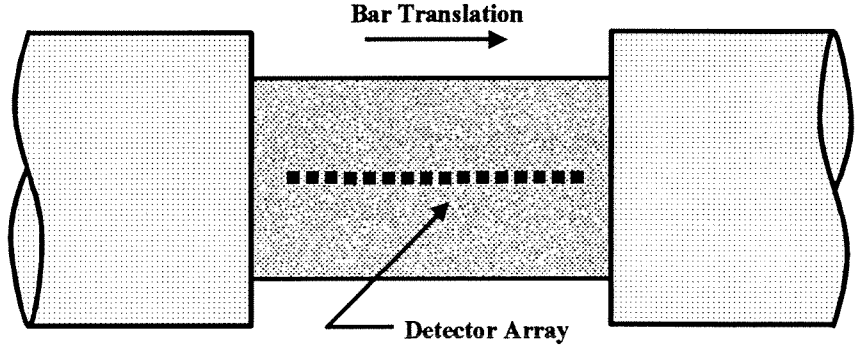

Figure 3.19 Schematic of compression Kolsky bar sample with array of infrared detectors used to determine degree of temperature homogeneity.

Metals used in the present study were chosen, in part, because each deform homogeneously in the Kolsky bar, over length scales on the order of detector size. One easy method to test such a claim is to employ a linear array of detectors to verify spatial

temperature uniformity. A 16-element InSb infrared detector array, with magnification optics, was used for this purpose. The InSb detector array was not used for actual tests because the HgCdTe detector had superior resolution near ambient temperatures. For the purpose of testing temperature uniformity, the InSb array proved more than adequate. Each candidate material was deformed in the Kolsky bar, and temperature was measured at multiple points as shown in Figure 3.19. As the sample translated relative to the detectors, a large fraction of the sample surface was viewed by the detectors. For metals which were known to localize, spikes in the temporal temperature were witnessed. Metals which deformed homogeneously had identical temperature profiles for every detector channel. It was noted that all materials have slightly higher temperatures near the bar-sample interface, since the state of stress is not purely one-dimensional there. During an actual test, the single detector is focused near the center of the sample, well away from the ends of the Kolsky bar.

- *No temperature gradients in the sample*

This assumption is related to homogeneous deformation. For a homogenous material undergoing homogeneous deformation, one would expect heat to evolve uniformly inside the sample volume. From equation (2.24), either a uniform temperature field within the sample or an adiabatic deformation process is sufficient to eliminate the heat conduction term.

- *Adiabatic deformation process*

Although the assumption of temperature uniformity within a homogeneously deforming sample is safe, a definite temperature gradient exists across the bar-sample interface. The temperature difference between the sample and surrounding environment

was never greater than 100 °C, and the maximum test duration in the Kolsky bar was 100 μs. Three possible avenues for heat loss, conduction, convection and radiation are available to the sample. Of these processes, conduction is, by far, the most significant.

In addition to the theoretical analysis above, one can simply look at the temperature profile during a test to estimate heat loss. Figure 3.20 shows a raw temperature profile for an α-Titanium sample deformed plastically in the Kolsky bar. The point where maximum temperature is attained corresponds to unloading of the sample. After that point, the sample cools by all the processes outlined above. The slope of the temperature profile after unloading provides an estimate of heat loss. Also, temperature is maximum just prior to unloading, thus the slope of the temperature curve immediately after unloading is actually an upper bound for conduction effects during sample loading. From the figure, one can see that there is a negligible temperature loss over a time that is greater than the duration of loading.

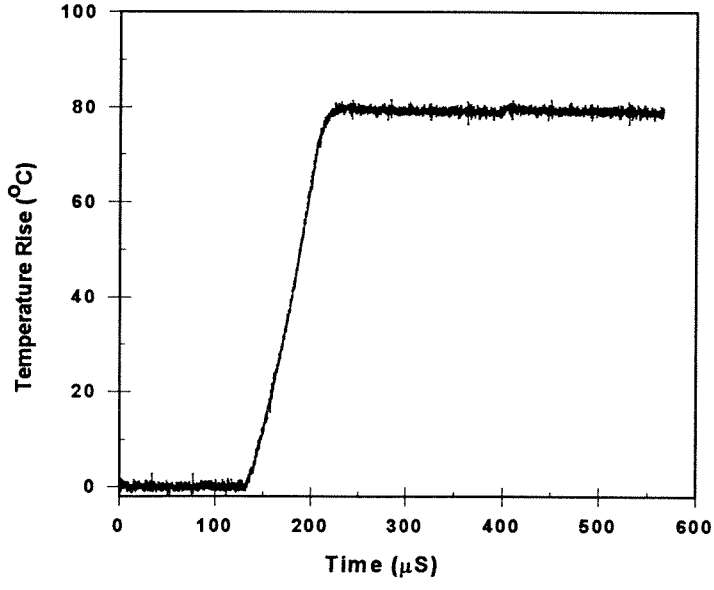

Figure 3.20 Raw temperature trace obtained during dynamic compression of titanium in the Kolsky bar.

- *Thermoelastic heating is negligible.*

For the heat conduction equation to reduce to (2.47), it is necessary to neglect thermoelastic heating. In materials with a positive coefficient of thermal expansion, the temperature decreases during adiabatic elastic extension and increases during adiabatic elastic compression. In principle, one cannot calculate β from (2.47). The numerator in that right side of (2.47) must first be corrected for thermoelastic heating. This is especially true for compressive deformation. The term

$$\frac{p}{\alpha}\frac{E}{(1-2\nu)}\theta_0 \mathrm{tr}(\dot{\varepsilon}^e) \tag{3.21}$$

which represents the thermoelastic source term found in most elasticity texts (Fung, 1965). In this equation, p is the coefficient of linear thermal expansion, α is the thermal diffusivity, θ_0 is the ambient temperature, and E and ν are Young's modulus and Poisson's ratio, respectively. Thermoelastic heating has been measured by several investigators (Bever et al., 1973), and is seldom greater than 0.2 °C. Depending on relative difference between elastic and plastic power input, the temperature rise from thermoelastic heating may or may not be significant. At low strain rates, the total temperature rise in a metal may only be a few degrees above ambient. In this case, thermoelastic heating is not negligible. For a metal deforming homogeneously at dynamic rates, a temperature rise of 80-100 degrees is not uncommon. If the metal only mildly hardens, the elastic strain rate is nearly zero after the onset of plastic flow. The elastic strain rate is typically only a couple percent of the plastic strain rate. In light of this fact, referring to equation (2.45), it is easy to see the relative dominance of the plastic power term.

3.7.3 Sources of Error.

The major assumptions of the experimental analysis were outlined above, and represent, to some extent, possible sources of error. The opinion here is that the above are not the major factors which limit the accuracy of the calculation of β.

As a metal specimen deforms in the Kolsky, its dimensions change. The object plane of the infrared optics remain fixed, so changes in specimen dimensions introduce a source of error in the measurement of temperature. The depth of field of the optics, however is quite large, on the order of the diameter of the specimen. This fact is evident when focussing the optics with the heated wire cross-hairs. Movements of the wires along the optic axis, within a span of several millimeters, produce negligible changes in the output voltage of the detector.

The Kolsky bar is ideally suited for measuring total work done on a metal sample. Oscillations, primarily due to dispersion, in the stress and strain signals can affect the measurement of total work at any given strain. These oscillations can be effectively minimized by placing tissue paper between the striker and input bars. Regardless of whether or not the sample deforms homogeneously, the Kolsky bar provides an accurate measure of total work. However, temperature is measured over a small area of the sample, so average total work will not be an adequate measure of total work within this small area unless the sample undergoes a homogeneous deformation. Even for materials which nominally deform homogeneously in the Kolsky bar, the ends of the sample near the input and output bar faces may experience local non-uniform deformation. If the temperature measurement is restricted to areas of the sample which are known to deform uniformly, the Kolsky bar's measure of total work is fairly accurate.

As demonstrated above, heat loss from the ends of the sample is a negligible source of error in the Kolsky bar.

The largest source of error is associated with temperature calibration. No single calibration can account for all conditions of a sample during deformation. The ideal situation would be to perform a calibration on a sample which exhibits known dynamic temperature changes, and whose surface texture varies predictably. However, by definition, if one could produce *known* dynamic temperature changes, then there would be no need for the infrared detectors. As long as the bandwidth of the detectors is suitable to perform both static temperature calibrations and dynamic temperature measurements, then there isn't much error in applying the calibrations to the Kolsky bar tests. The procedure used in this study was to duplicate test conditions, to the extent possible, when performing temperature calibration. The error is, at least, minimized by this approach.

Another source of error, associated with the data analysis techniques, also exists. These will be addressed, for the most part, in the next couple chapters, but they will be introduced here. Equation (2.47) requires a time derivative of temperature. Differentiation of noisy signals has inherent complexities, which can introduce error into the calculation of β. Also, there is a time shift of the traces for stress, strain rate and temperature during a test. All electromagnetic radiation travels at the speed of light, so the speed of temperature detection is limited only by the detector electronics. One can regard the whole temperature detection process, at least compared to the measurement of mechanical properties, as in-situ. Stress and strain rate are calculated from the strain gages on the input and output bars. Therefore, stress and strain rate are effectively

measured after temperature has been recorded. One must correlate the mechanical fields with the temperature field to calculate β as a function of time, or strain. The specific procedure will be discussed in the chapter that follows.

3.8 References

Bever, M.B., Holt, D.L., Titchener, A.L., (1973), "The Stored Energy of Cold Work," *Prog. Mat. Sci.*, **17**, 1.

Chen, W., Ravichandran, G. (1996), "An Experimental Technique for Imposing Dynamic Multi-axial Compression with Mechanical Confinement," *Experimental Mechanics*, **36**, 155.

Duffy, J., Cambell, J.D., and Hawley, R.H., (1971), "On the Use of the Torsional Hopkinson Bar to Study Rate Effects in 1100-0 Aluminum," *J. Appl. Mech.*, **38**, 83.

Follansbee, P.S., (1985), "The Split Hopkinson Bar," in *ASM Handbook: 9th Edition*, **8**, ASM International, Metals Park, OH.

Fung, Y.C. (1965), *Foundations of Solid Mechanics*, Prentice-Hall, New York.

Gilat, A., Pao Y.H., 1988, "High-Rate Decremental Strain Rate Test," *Experimental Mechanics*, **28**, 322.

Hartley, K.A., Duffy, J., (1990), "High Strain Rate Shear Testing," in *ASM Handbook: 9th Edition*, **8**, ASM International, Metals Park, OH.

Higgins, T.V. (1995), *Laser Focus World*, **31**, 63.

Kolsky, H. (1949), *Stress Waves in Solids*, Dover Publications, New York.

Lindholm, U.S. (1964), "Some Experiments with the Split Hopkinson Pressure Bar," *J. Mech. Phys. Solids*, **12**, 317

Mason, J.J., Rosakis, A.J., Ravichandran, G., (1993), "On the Strain and Strain Rate

Dependence of the Fraction of Plastic Work Converted into Heat: An Experimental Approach using High-Speed Infrared Detectors and the Kolsky Bar," *Mech. of Materials*, **17**, 135.

Omega Engineering (1992), *The Temperature Handbook*, **28**, Sec. Z.

Ozisik, M.N. (1980), *Heat Transfer*, Wiley, New York.

Ozisik, M.N. (1985), *Heat Transfer: A Basic Approach*, McGraw-Hill, New York.

Wolfe, W.L., Zissis, G.J, Eds. (1978), *The Infrared Handbook*, Environmental Research Institute of Michigan, Ann Arbor, MI.

Zehnder, A.T., Rosakis, A.J. (1993), "Temperature Rise at the Tip of Dynamically Propagating Cracks: Measurements Using High-Speed Infrared Detectors," in *Experimental Techniques in Fracture III*, ed. by J. Epstein, Society of Experimental Mechanics.

Zehnder, A.T., Rosakis, A.J., 1991, "On the Temperature Distribution at the Vicinity of Dynamically Propagating Cracks in 4340 Steel," J. Mech. Phys. Solids, 39, 385.

CHAPTER 4

ENERGY STORAGE IN RATE-SENSITIVE METALS

4.1 Introduction.

One of the fundamental assertions of the present study is that energy storage in metals, or equivalently, the fraction of plastic work available as heat, should be treated as a constitutive function. Classes of constitutive functions for the stress response of engineering materials are numerous. For a given material, variables which affect the stress response of materials are identified, and included in the constitutive formulation. For metals, typical variables which affect stress include a measure of strain, temperature, rate of deformation and other "internal variables," which may represent loading history or structural characteristics. It is natural to expect the dependence of stress on these variables to vary greatly between metal systems. As an extreme example, if one were to perform an isothermal mechanical test on tungsten and aluminum at 650 °C, the flow stress for tungsten would still be reasonably high, whereas aluminum would undergo eutectic melting, and flow like a fluid. The hardening of metals, which increases the stress required to further move dislocations and accumulate plastic strain, is a definite function of the extent of deformation. The microstructural mechanisms for hardening in metals are, in many ways, related to energy storage. Interactions between dislocations decrease dislocation mobility, requiring larger forces, and thus, higher energies to overcome these barriers. Dislocations can pile up at the boundaries of grains. The distorted lattice around this type of configuration has an associated strain energy, which

can be released if the dislocations "break through" the grain boundary barrier. The energy associated with this type of phenomenon can be significant, as detailed by Armstrong et al. (1982). Analogous to the conclusion that microstructural avenues for hardening depend on the particular metal system, energy storage is also material dependent. Bever (1973) remarked on the spread in measured values of stored energy in nominally pure copper. The conclusion was that impurities had a large affect on the storage of energy in the lattice of copper. Even Taylor and Quinney's original paper (1937) on energy storage in metals came to the conclusion that stored energy was a function of strain. While it is true that Taylor observed that "most" of the plastic work appears as heat for the metals he tested (copper and mild steel), that particular study is often quoted for justification in assuming a constant β of 0.9-1.0 for all metals.

For a majority of metals, the stress-strain curves are sensitive to strain rate, $\dot{\varepsilon}$. More often than not, the flow stress increases with strain rate. The work-hardening rate can also be affected by strain rate (Meyers and Chawla, 1984). Two parameters are defined to describe strain rate effects in the uniaxial case

$$m = \left(\frac{\partial \ln(\sigma)}{\partial \ln(\dot{\varepsilon})} \right)_{\varepsilon,T} \tag{4.1}$$

$$s = \left(\frac{\partial \ln(K)}{\partial \ln(\dot{\varepsilon})} \right)_{\varepsilon,T} \tag{4.2}$$

where

$$K = \left(\frac{d\sigma}{d\varepsilon} \right)_{\varepsilon,T}. \tag{4.3}$$

m is known as the strain rate sensitivity, and s, the hardening rate sensitivity. K is the tangent modulus, and is simply equal to Young's modulus for strains below the proportional limit. In general, m varies between 0.02 and 0.2 , for temperatures less than 90% of the melting temperature. Some metals, such as aluminum alloys, have a strain rate sensitivity near zero.

Property	Conditions	Value
Density	298 K	4520 kg/m^3
Melting Point	-	1668 °C
Crystal Structure	α-phase	h.c.p.
	β-phase	b.c.c.
α → β Phase Transition	-	883 °C
Coefficient of Thermal Expansion	293 K	8.41 x 10^{-6}/°C
	350 K	4.0 x 10^{-4}/°C
	400 K	7.5 x 10^{-4}/°C
Specific Heat	275 K	513 J/kg·K
	300 K	538 J/kg·K
	350 K	568 J/kg·K
	400 K	587 J/kg·K
Thermal Conductivity	300 K	18.8 W/m·K
Thermal Diffusivity	300 K	0.077 cm^2/s

Table 4.1 Selected physical and thermal properties of elemental titanium.

A hexagonal close packed (h.c.p.) metal, α-titanium, the most common phase of pure titanium, was chosen for the present study of energy storage in rate-sensitive metals. Titanium has two primary phases, dented by the Greek letters α and β. In the phase diagram of titanium, the α and β phases are separated by a well-defined temperature, 883 °C (ASM Handbook, 1990). At lower temperatures, titanium naturally exists in the α (h.c.p.) phase. Above the critical temperature, a phase transformation takes place, and titanium adopts a stable body-centered cubic (b.c.c.) β phase. Binary phase alloys of titanium is possible by adding other elements together with special heat treatments. The

most common α + β alloy is Ti-6Al-4V, used extensively in aerospace and other high performance applications. Only the α phase was used for the experiments described here.

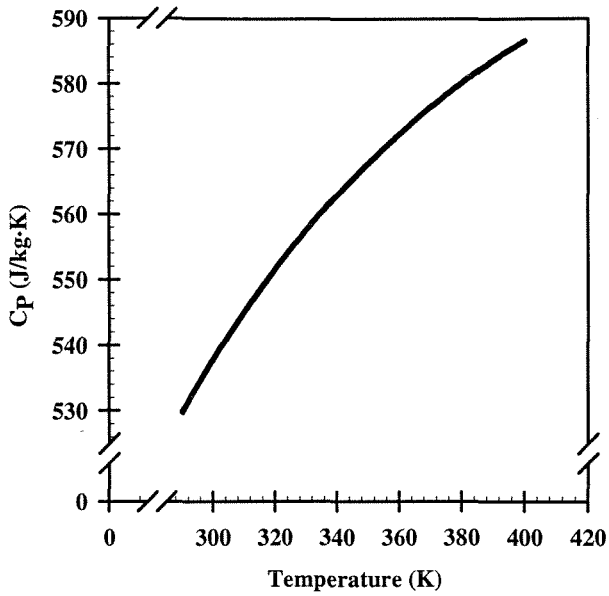

Figure 4.1 Temperature dependence of heat capacity for α-titanium.

Table 4.1 lists several relevant physical and thermal properties of pure α-titanium, many of which were used in calculations of the partition of plastic work (ASM Handbook, 1990). Figure 4.1 shows the temperature dependence of the specific heat capacity for α-titanium over the range of temperatures expected during the mechanical tests. The graph in Figure 4.1 was produced by fitting tabulated values of heat capacity over the temperature range shown. The mechanical properties and microstructure of α-titanium have been investigated by others researchers (Meyers et al., 1994; Chichili et al., 1997). These papers, although not dealing with energy storage issues per se, provide examples of various avenues for energy storage and their correlation with uniaxial mechanical properties. Meyers et al. observed strain rate sensitivity in flow stress for α-titanium, as well as planar dislocation arrays and profuse twinning at lower plastic strains. Chichili et al. also reported substantial rate-sensitivity in flow stress over a range

of strain rates from 10^{-5} to 10^{5}. The strain-hardening was also observed to be rate sensitive, which was attributed to extensive deformation twinning.

4.2 Format of Raw Data for α-Titanium.

Figure 4.2 is a plot of the raw mechanical end thermal data from a compression Kolsky bar test of α-titanium. Raw data from the torsion Kolsky bar closely resembled

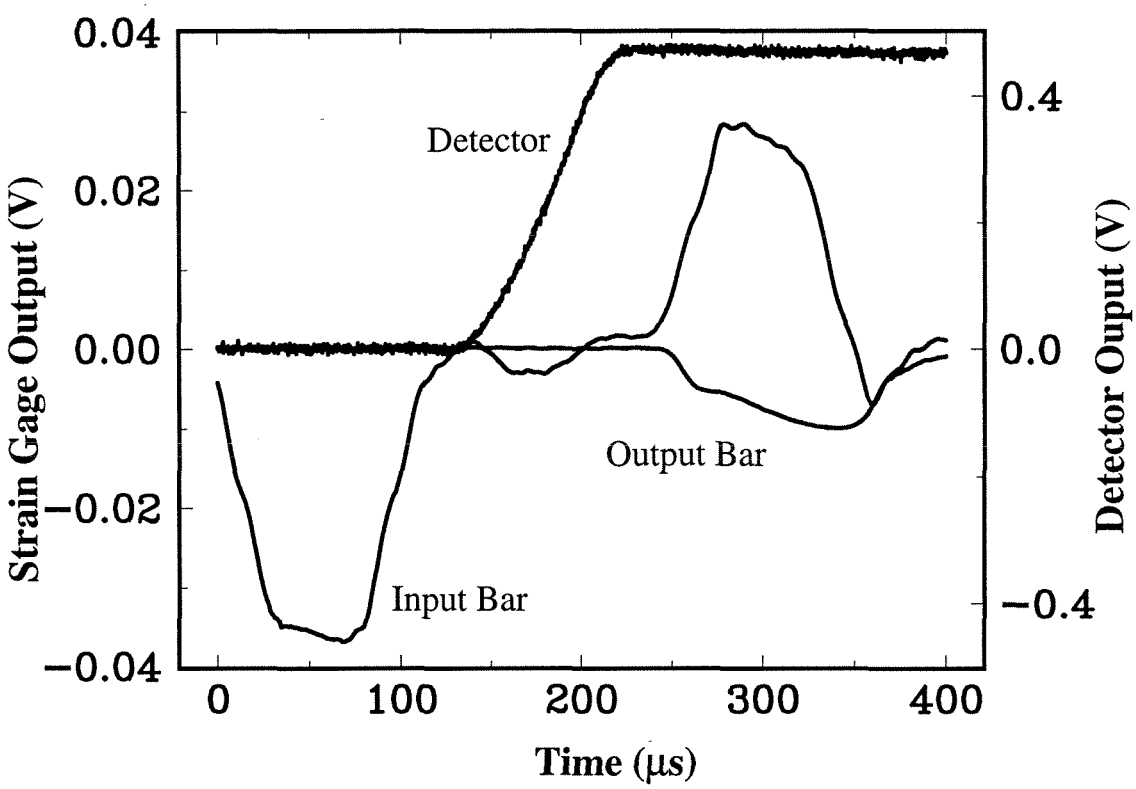

Figure 4.2 Example of raw data obtained from HgCdTe infrared detector and the compression Kolsky bar.

data in compression. From the figure, it is evident that the temperature rise in the sample was recorded at an earlier time than the mechanical data from the strain gages. This was mentioned in the previous chapter, and was a result of the location of the strain gages relative to the sample. The signals recorded from the strain gages were essentially free of oscillations. The reflected and transmitted signals often include superimposed

oscillations, due in part to ringing at the interface of the striker and input bars. Figure 4.3 shows the effect of ringing on the Kolsky bar signals. The signal with superimposed Pochammer-Chree oscillations was a result of direct impact of the striker bar and input bar. Next, a small piece of greased tissue paper was placed on the input bar face prior to impact, and the result was a signal free of large oscillations. The amplitude of the oscillations can be a reasonable fraction of the baseline signal amplitude. With smooth signals of stress and strain rate, the calculation of plastic work rate did not need additional corrections or smoothing. The temperature smoothly rose from a zero baseline voltage to a maximum, after which no further loading was encountered. The temperature profile in Figure 4.2 was typical for a metal deformed homogeneously.

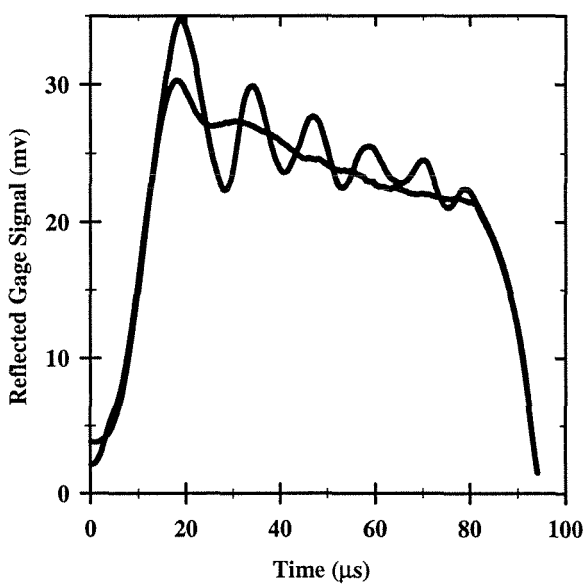

Figure 4.3 Effect of lubricant at the striker bar-input bar interface on the quality of the loading pulse for the compression Kolsky bar.

The MTS universal test frame was used to load α-titanium at lower strain rates. Raw data from this type of test is shown in Figure 4.4. Load and displacement are measured directly from the MTS, and temperature was measured from a thermocouple mounted on the sample surface. The acquisition rate of the Nicolet oscilloscope was set

to correspond with the approximate rise time of the thermocouple. In-situ load, displacement, and temperature data were measured at the same time. No time delay existed between thermal and mechanical measurements as was the case for the Kolsky bar. This fact eliminated possible errors involved in time shifting the measured signals. Also, the MTS produced more accurate mechanical data at low strains than the Kolsky bar, which needs several wave reflections in the sample to establish equilibrium (Subhash and Ravichandran, 1994). This is the primary reason elastic properties cannot be accurately determined from a conventional Kolsky bar.

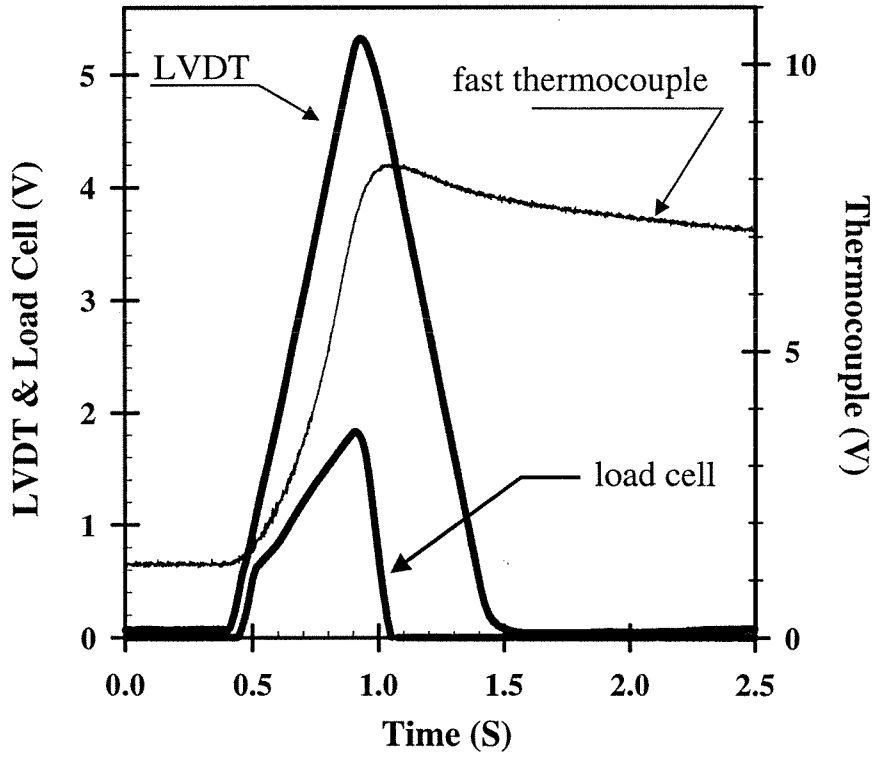

Figure 4.4 **Example of raw data obtained from E-type thermocouple and MTS servo-hydraulic load frame.**

4.3 Data Reduction and Analysis.

For every test, load, displacement or displacement rate, and temperature were measured. Examples of raw data for dynamic and quasi-static loading were given above.

One quick check of the integrity of the data involved comparing the total work and total heat evolved during a test cycle. The total work per unit volume of the sample was calculated by

$$W = \int_0^{\varepsilon_f} \sigma \, d\varepsilon \tag{4.4}$$

which is equivalent to calculating the area under the resulting stress-strain curve. Total heat evolved was, in general,

$$Q = \int_{\theta_i}^{\theta_f} \rho c_p \, d\theta \tag{4.5}$$

where θ_i and θ_f represent the initial and final temperature states, respectively. For constant density and specific heat capacity,

$$Q = \rho c_p (\theta_f - \theta_i). \tag{4.6}$$

In absence of an initial amount of stored energy, the heat calculated from temperature measurements must be less than the total work done on the sample. The ratio of total heat evolved to total work provided an approximation of the average fraction of work converted into heat. For metals with a propensity to localize, the calculated heat from equation (4.5) can be greater than equation (4.4) if temperature was measured over an area of localized deformation.

4.3.1 Kolsky Bar Experiments

The rate performing plastic work, $\dot{W}^P$, in the Kolsky bar was easily calculated directly from strain gage signals. The strain gages were carefully located at equal distances from the forward sample face (refer to Fig. 3.4), thus time-shifting of the

reflected gage signal relative to the transmitted gage signal was not required. The product of engineering stress, Eq. (3.5), and the plastic part of engineering strain rate, Eq. (3.3), gave the plastic work rate for uniaxial compression. The plastic strain rate was determined by subtracting the elastic strain rate from the total strain rate

$$\dot{\varepsilon}^{p}(t) = \dot{\varepsilon}(t) - \dot{\varepsilon}^{e}(t) = \dot{\varepsilon}(t) - \frac{1}{E}\dot{\sigma}(t) = \dot{\varepsilon}(t)\left(1 - \frac{1}{E}\frac{d\sigma}{d\varepsilon}\right) \tag{4.7}$$

where E was the elastic modulus, and $d\sigma/d\varepsilon$ the tangent modulus. Although the plastic part of the total strain rate was always used to calculate plastic work rate, in actuality, the elastic strain rate was small compared to the plastic strain rate.

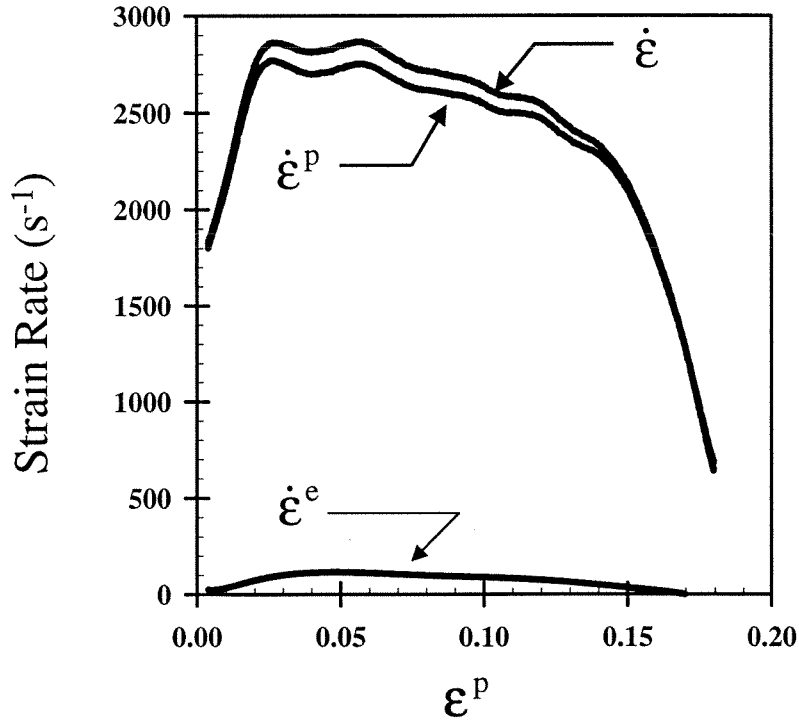

Figure 4.5 **Comparison of total, plastic, and elstic strain rates for α-titanium in the compression Kolsky bar.**

Figure 4.5 compares the total, plastic and elastic strain rates for dynamic compression of α-titanium in the Kolsky bar. The elastic strain rate peaked at a value just over 3% of the total strain rate. Titanium exhibited a high degree of hardening, so Figure 4.5 actually

represents a relatively high elastic strain rate. Metals which do not harden as severely – aluminum for example - exhibit much smaller elastic strain rates after the onset of plastic flow. The resulting plastic work rate had the form plotted in Figure 4.6.

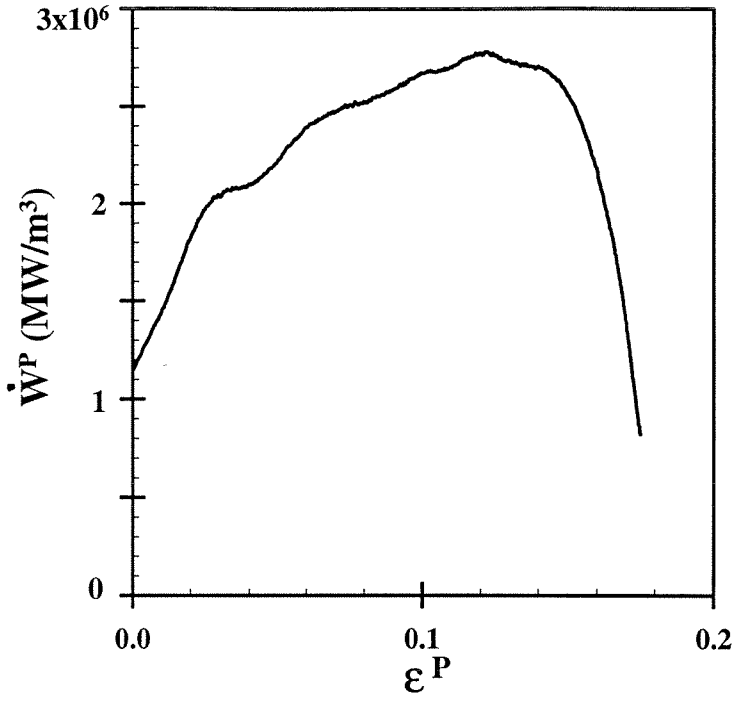

Figure 4.6 Plot of plastic work rate against plastic strain for α-titanium.

The heat evolution was calculated from the measured temperature signal. Differentiation of the time resolved temperature signal was needed to determine the rate of heat evolution, which is the product of density, specific heat capacity and the time derivative of temperature. In general, differentiation of noisy signals has inherent instabilities. Finite difference or central difference techniques are ideally suited when exact analytical functions are known. They are not suitable for differentiating experimental data. Another method, attributed to Vasin (1973) and Groetsch (1992), produces a smoothed derivative of a noisy signal using filtering techniques. The idea is as follows. Suppose the time derivative of a function, f(t), is desired. Another function, g(t), is chosen such that

$$f_s(t) = f(t) * g(t) \tag{4.8}$$

and the convolution operation results in a smoothed representation of the original function, f(t). Here, the function g(t) acts as a band-pass filter in the frequency domain. The smoothed first time derivative of f(t) can then be found by taking advantage of the relation

$$\dot{f}_s(t) = \dot{f}(t) * g(t) = f(t) * \dot{g}(t). \tag{4.9}$$

Thus, one need only convolve the original function, f(t), with the time derivative of the smoothing function, g(t), to produce a smoothed time derivative of f(t). For some experimental signals, to attain a reasonably smooth time derivative, the cutoff frequency of the filter must be made small, which can attenuate the original signal. This is equivalent to a large time window for the function g(t), or, weight averaging over too many points. In many cases, a better approach is simply to fit a high order polynomial to the noisy data, then find the time derivative by differentiating the polynomial. Obviously, this method is not optimal for all types of signals, but it worked best for temperature signals that resulted from the Kolsky bar experiments described here. Figure 4.7 illustrates the small advantage gained by fitting a polynomial to the raw temperature signal of Figure 4.2. In the figure, the signals are time shifted relative to one another for clarity. The curve using the filtering method outlined above contained oscillations which did not seem to represent real material behavior. Rather, the oscillations are a testament to the difficulty of the differentiation of noisy signals. The calculation of $\dot{W}^P$ also had oscillations, described earlier, associated with wave dispersion. If the oscillations in the temperature derivative have different frequencies and amplitudes than $\dot{W}^P$, large errors

can result when calculating the ratio of the two quantities. Density was taken to be constant, since the temperature rise was never more than 100 K above ambient conditions. Heat capacity was allowed to vary with temperature (see Table 4.1; Fig. 4.1).

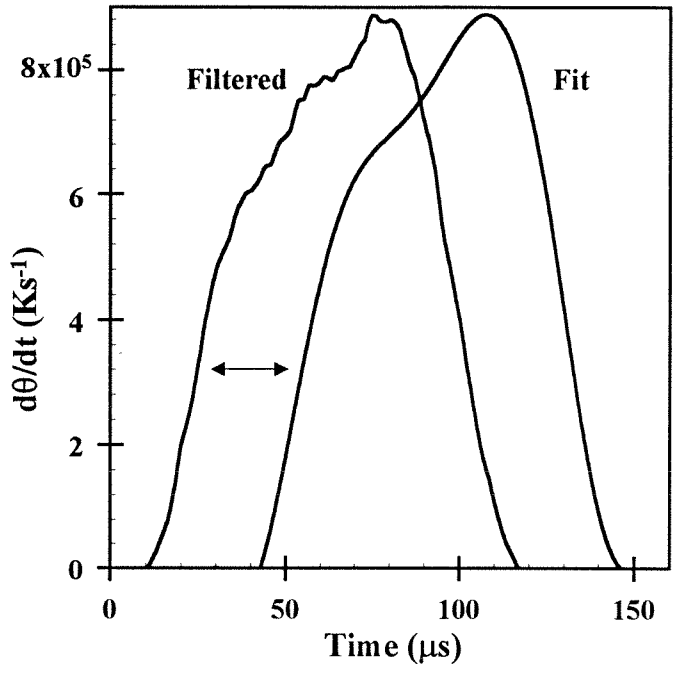

Figure 4.7 Two methods of calculating the time derivative of a noisy temperature signal.

As discussed earlier, before the ratio of heating rate to plastic work rate was calculated, the signals were time-shifted. For each test, the maximum temperature was matched, in time, with the point of maximum strain. This criterion was effectively equivalent to equating the point of zero strain rate, the start of unloading on the stress-strain curve, with the point at which the time derivative of temperature is zero. Figure 4.8 shows heating rate and plastic power plotted against plastic strain on the same graph. This type of plot was effective at revealing trends in the strain dependence of energy storage. The difference between the upper and lower curve in Figure 4.8 at any strain represented the marginal rate of energy storage in the metal.

With reference to Figure 4.8, it should be mentioned that a certain difficulty existed when calculating β near the yield point, and near the point of unloading. At the onset of plastic flow, the plastic strain rate was a rapidly increasing function of both time and strain. At this point, heating rate was also increasing rapidly, as the primary mechanism changes from a relatively small thermoelastic heating rate to one dominated by plasticity. The difficulty arose when time-shifting the two curves relative to one another. Figure 4.9 illustrates a small forward and backward shift of the same curves plotted in Figure 4.8. The ratio of the heating rate to plastic power was very stable over the central portion of the curves. Over this range, strain rate was nearly constant. However, the ratio varies substantially at either end of the curves in Figure 4.9. For this reason, the ratio of energy dissipation to work was only estimated near the yield point of the material.

4.3.2 MTS Experiments

Analyzing the measured thermal and mechanical quantities from quasi-static tests was somewhat different from tests in the Kolsky bars. The MTS load frame provided a direct measure of load and displacement, from which engineering stress and engineering strain were calculated. Plastic strain was calculated from

$$\varepsilon^{P}(t) = \varepsilon(t) - \frac{1}{E}\sigma(t). \tag{4.10}$$

The product of the time derivative of equations (4.10) and $\sigma(t)$ gave the plastic work rate, $\dot{W}^{P}$. Heating rate was calculated from the output of the attached thermocouple in the same manner as with the infrared thermal detector and the Kolsky bar. The primary difference was that the thermal and mechanical measurements did not need to be time-

shifted relative to each other. This made for easy analysis of the experimental data in quasi-static compression.

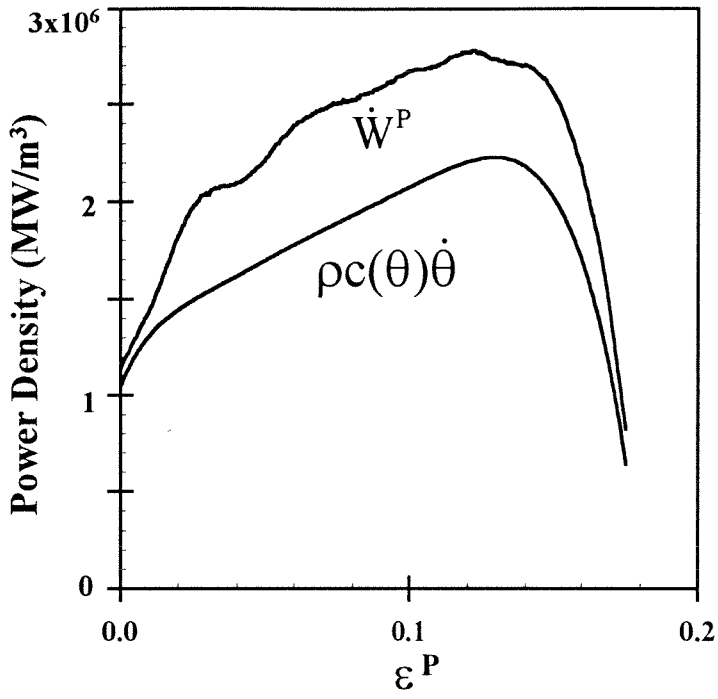

Figure 4.8 **Plastic work rate and heating rate plotted against engineering plastic strain.**

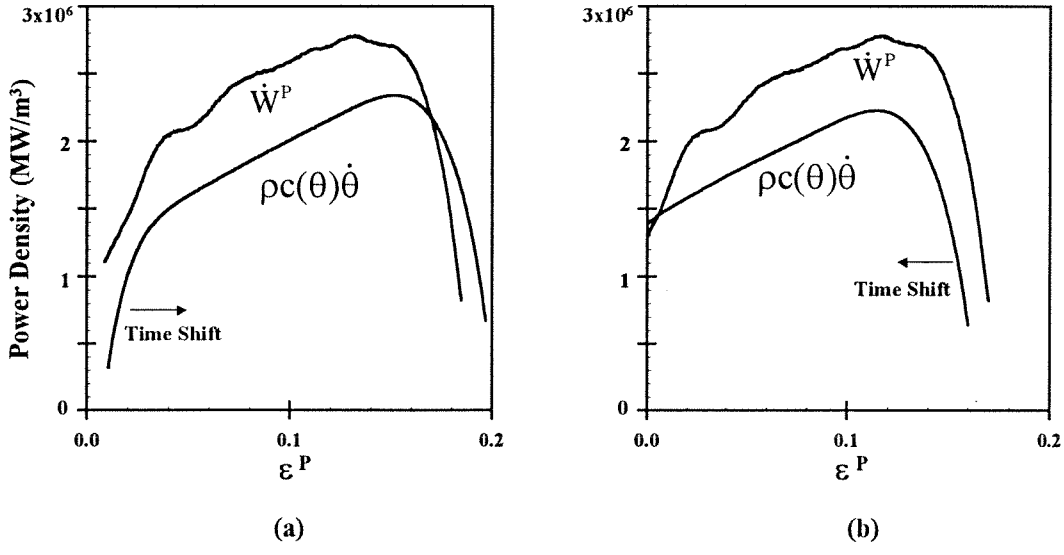

Figure 4.9 **Effect of time shifting the heating rate relative to plastic work rate: (a) positive time shift, (b) negative time shift.**

4.4 Results and Discussion.

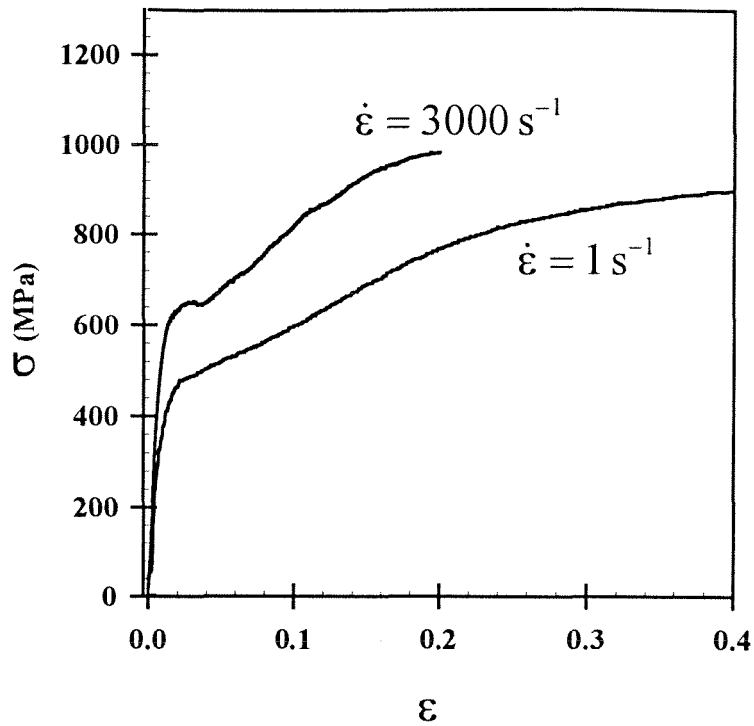

Figure 4.10 Strain rate effects on the true stress-strain behavior of α-titanium in uniaxial compression.

The strain rate dependence of flow stress was evident from the true stress-strain curves shown in Figure 4.10. The flow stress for α-titanium is clearly dependent on the strain rate during loading. Hardening rate also seemed to depend on strain rate. At equal strains, the tangent modulus for stress-strain curves produced from the Kolsky bar (> 10^3 s-1) was greater than the modulus for tests in the MTS load frame (< 1 s^{-1}). Tests at rates less than 10^{-2} s^{-1} were nearly isothermal, and the stress response was not influenced by thermal softening. Thus, the difference in tangent modulus may indeed be slightly greater than shown in Figure 4.10, since Kolsky bar tests are essentially adiabatic. Another point regarding Figure 4.10, the stress-strain curves produced by the Kolsky bar did not produce a well defined yield point, especially for rate-sensitive metals. The rise time of the loading pulse was too long to prevent yield before a constant strain rate was

attained. The first 1-2% strain after the onset of plastic flow was actually a state of increasing strain rate. Large strains were attained on the compression Kolsky bar by a recovery and reloading technique described in the previous chapter. Figure 4.11 shows the true stress-strain curves produced from this technique. For α-titanium and other rate-sensitive metals, care must be exercised to match strain rates for each loading sequence.

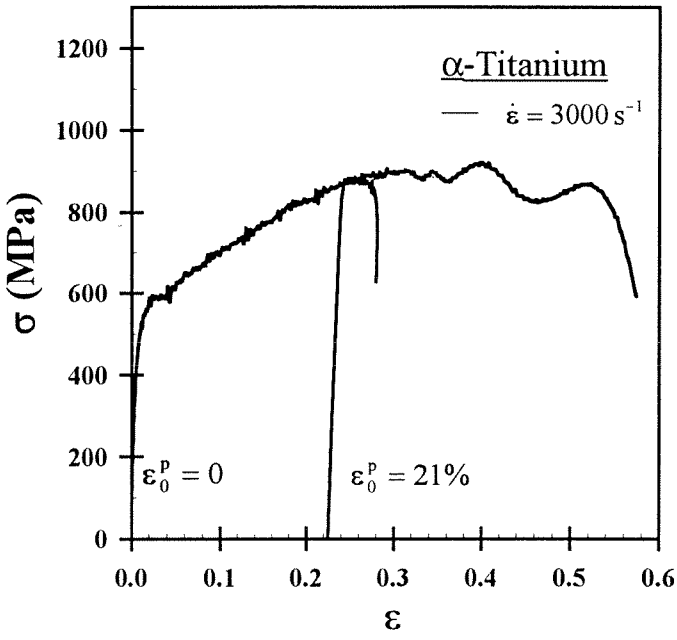

Figure 4.11 Result of recovery and reloading technique used to obtain large strains in the compression Kolsky bar.

The partition of plastic work, into heat and stored energy, was observed to be dependent on both of strain and strain rate in α-titanium. Figure 4.12 shows the fraction of plastic work converted into heat, β, plotted against engineering plastic strain during uniaxial compressive deformation. The curves shown here represent the value of β at low levels of plastic strain. At a strain rate of 1 s^{-1}, titanium stored a relatively large amount of energy, 35-40%, just after yield. As strain increased, the ability to store energy was reduced. At higher strain rates, less energy was stored at all strain levels in this range.

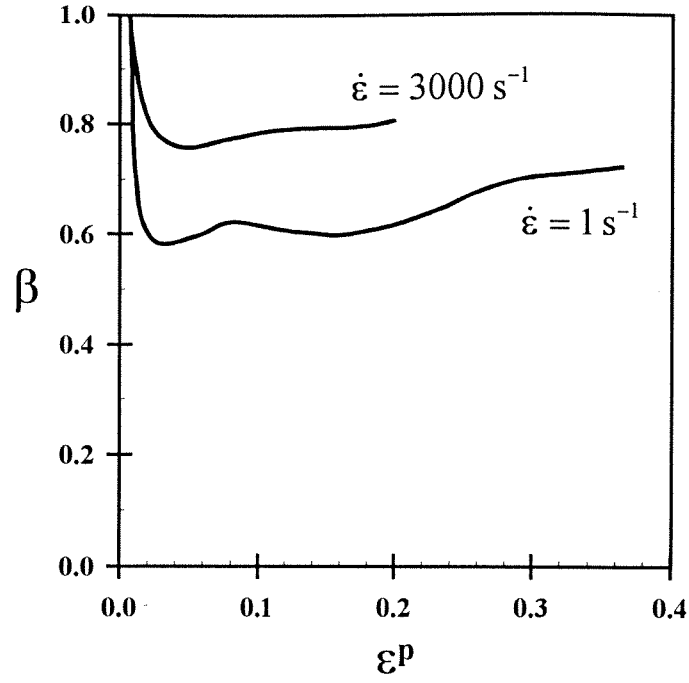

Figure 4.12 Effect of strain and strain rate on the fraction of plastic work converted into heat in α-titanium.

Figure 4.13 also plots β against engineering plastic strain, but includes a greater range of strains. The material cannot store energy indefinitely, and at some critical level of plastic strain, nearly all of the energy was dissipated as heat. The critical strain, after which the microstructure has exhausted all avenues of energy storage, may also depend on strain rate. The result for dynamic torsion, at a similar equivalent strain rate All curves shown in Figure 4.13 were produced by different loading methods, specimen geometry and temperature measurement, and thus, have their own intrinsic errors. However, the trends in all cases were consistent. The critical strain in dynamic torsion, for example, seemed to be lower than for dynamic compression. The specimen geometry in torsion did not lend itself to the remachining technique described in the previous chapter, and the results was influenced by the increased emissivity of the rough surface. The curves for dynamic compression in Figs. 4.13 and 4.14 represented nearly constant surface emissivity as a function of strain.

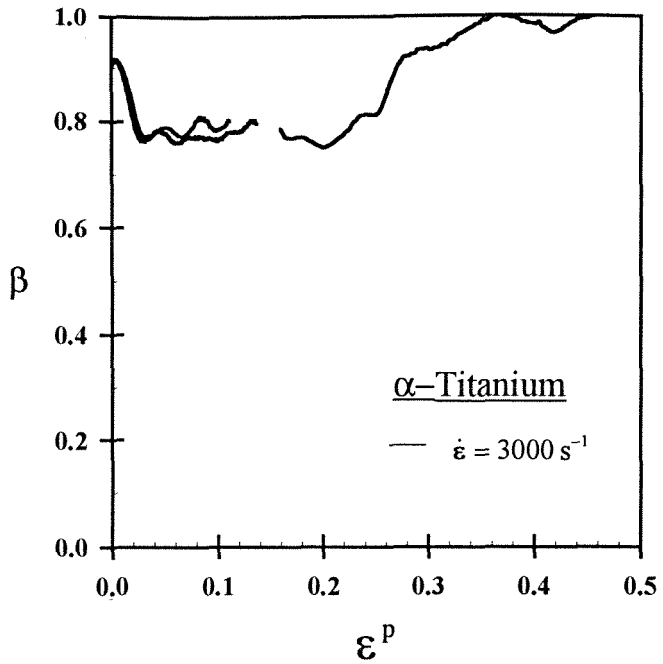

Figure 4.13 **Strain dependence of the fraction o plastic work converted into heat during uniaxial compression. Large strains were obtained by recovering, remachining, and reloading samples of α-titanium.**

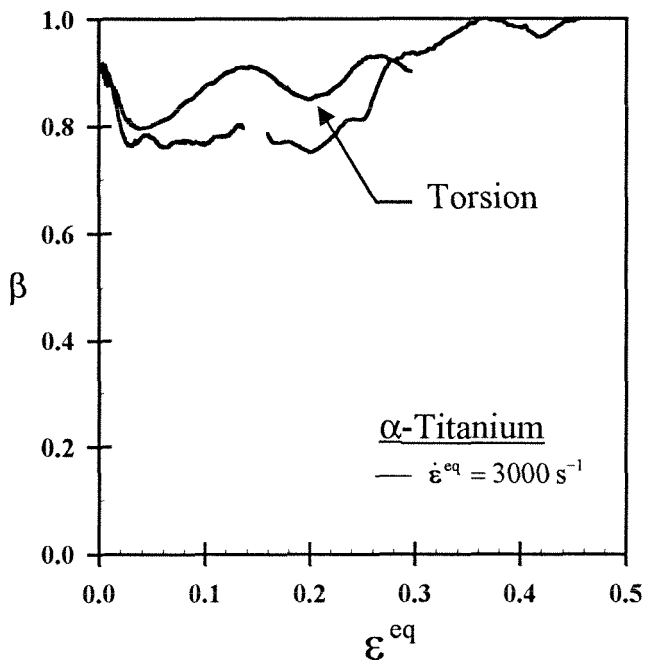

Figure 4.14 **Comparison of the fraction of plastic work converted into heat in compression and torsion.**

From the previous three figures (Fig. 4.12, Fig. 4.13, and Fig. 4.14) several features emerge concerning the amount of energy dissipation in α-titanium. It is clear that energy

storage in titanium is definitely a function of strain. The theoretical basis for such an assumption was developed in Chapter 2, and it has been demonstrated experimentally in the graphs above. Near the yield point, during the stage of rapid dislocation multiplication, β was observed to be a rapidly decreasing function of strain at both strain rates. This was predicted in the model by Aravas et al. (1990), and reviewed in Chapter 2. The relative ability of titanium to store cold work increased with decreasing strain rate. Referring back to Equation (2.46), which is the one-dimensional heat conduction equation for adiabatic plasticity (neglecting thermoelastic effects), β is predicted to decrease with decreasing strain rates. This is in agreement with Figure 4.12. The energy function in (2.46) is not a function of strain rate, thus, the rate dependence of β is a result of the rate dependence of σ. Generally speaking, an increase in strain rate is always accompanied by an increase in flow stress, since rate-sensitive metals are usually associated with $m>0$ (Eq. (4.1)). As shown in Figure 4.13, titanium cannot store energy indefinitely. After some critical level of plastic strain, titanium dissipates nearly all plastic work as heat. The critical strain could very well be strain rate dependent.

4.5 References

Aravas, N., Kim, K.S., Leckie, F.A. (1990), "On the Calculations of the Stored Energy of Cold Work," *J. Eng. Mat. Tech.*, **112**, 465.

Armstrong, R.W, Coffey, C.S., Elban, W.L. "Adiabatic Heating at a Dislocation Pile-Up Avalanche," *Acta Metall.*, **30**, 2111.

ASM Handbook: Vol 2. (1990), "Properties and Selection of Non-ferrous Alloys and Special Purpose Materials," ASM International, Metals Park, OH

Bever, M.B., Holt, D.L., Titchener, A.L., (1973), "The Stored Energy of Cold Work," *Prog. Mat. Sci.*, **17**, 1.

Chichili, D.R., Ramesh, K.T., Hemker, K.J. (1997), submitted to *Acta Metall.*

Groetsch, C.W. (1992), "Optimal Order of Accuracy in Vasin's Method for Differentiation of Noisy Functions," *J. Optimization Theory and Applications*, **74**, 373.

Meyers, M.A., Chawla, K.K. (1984), *Mechanical Metallurgy*, Prentice-Hall, New York.

Meyers, M.A., Subhash, G., Kad, B.K., Prasad, L. (1994), *Mech. Mat.*, **17**, 175.

Ravichandran G., Subhash, G. (1994), "Critical Appraisal of Limiting Strain Rates for Compression Testing of Ceramics in a Split Hopkinson Pressure Bar," *J. Am. Ceram. Soc.*, **77**, 263.

Taylor, G.I., Quinney, H. (1937), "The Latent Heat Remaining in a Metal after Cold Working," *Proc. Royal Soc.*, **A163**, 157.

Vasin, V.V. (1973), "The Stable Derivative in the Space C(-∞,∞)," USSR Comp. Math. Math. Phys., **13**, 16.

CHAPTER 5

ENERGY STORAGE IN RATE-INSENSITIVE METALS

5.1 Introduction and Background.

The stress-strain curves are, for the majority of metals, sensitive to the rate of deformation. In general, the flow stress increases with strain rate, or equivalently stated, larger forces are necessary to increase the velocity of dislocations, since it is the motion of dislocations which is responsible for plastic flow. Not all metals exhibit appreciable strain rate sensitivity. Aluminum and many of its alloys have zero, or a near zero of the strain sensitivity parameter, m, defined in the previous chapter. When considering the effect of strain rate on energy storage, it is natural to question whether materials which do not experience a flow stress dependence on strain rate. Energy storage in these materials would also be independent of strain rate.

Table 5.1 lists several physical and thermal properties of 2024 aluminum alloy. 2024 is one of the most common alloys of aluminum, having applications in aircraft structures, rivets, screw machine products and other miscellaneous structural applications. This particular alloy was used extensively in the current study, since it is widely available, widely studied and documented, and because of its applicability as a high performance structural material. Moreover, 2024 aluminum alloy was known to be rate insensitive over a wide range of strain rates, and deform homogeneously in the Kolsky bar.

Table 5.1 Some physical and thermal properties of 2024 aluminum alloy.

Property	Conditions	Value
Density	298 K	2770 kg/m^3
Melting Point	solidus	775 K
	liquidus	911 K
Crystal Structure	-	f.c.c.
Coefficient of Thermal Expansion	293-373 K	22.9 μm/m·K
	293-473 K	23.8 μm/m·K
	293-573 K	24.7 μm/m·K
Specific Heat Capacity	300 K	857 J/kg·K
	350 K	891 J/kg·K
	400 K	920 J/kg·K
Thermal Conductivity	T351,T4 - 300 K	120 W/m·K
	T6 – 300 K	151 W/m·K
Thermal Diffusivity	T351,T4 - 300 K	0.505 cm^2/s
	T6 – 300 K	0.636 cm^2/s

The strengthening mechanisms in aluminum alloys, in many ways, are coupled with its avenues for energy storage. It is therefore instructive to give a brief overview of aluminum microstructure , and precipitation strengthened materials in general. A good fraction of aluminum alloys rely on distributions of precipitates and second phase particles to improve strength and other mechanical properties. Common alloying elements, like copper, magnesium, iron, and manganese have different effects on the microstructure of the resulting alloy. In addition, by taking advantage of the temperature dependence of the solubility of these elements in aluminum, controlled heat treatments can be used to manipulate the final microstructure. Copper, magnesium, and manganese are the primary alloying elements in 2024 aluminum., and are added in excess of their solubility limit at room temperature, 4.4 % Cu and 1.5 % Mg 0.6% Mn. After quenching from the solution (initial heat treatment) temperature, second-phase particles are precipitated inside the grains. Manganese acts as a grain refiner. If other, impurity atoms

are present, then second-phase particles can also form at grain boundaries as well. The relative position, size, shape and hardness of precipitates in the aluminum alloy all influence dislocation nucleation and mobility. The size and spacing of precipitates can be altered by heat treatment, thus alloys of aluminum are always referenced by temper when listing mechanical properties.

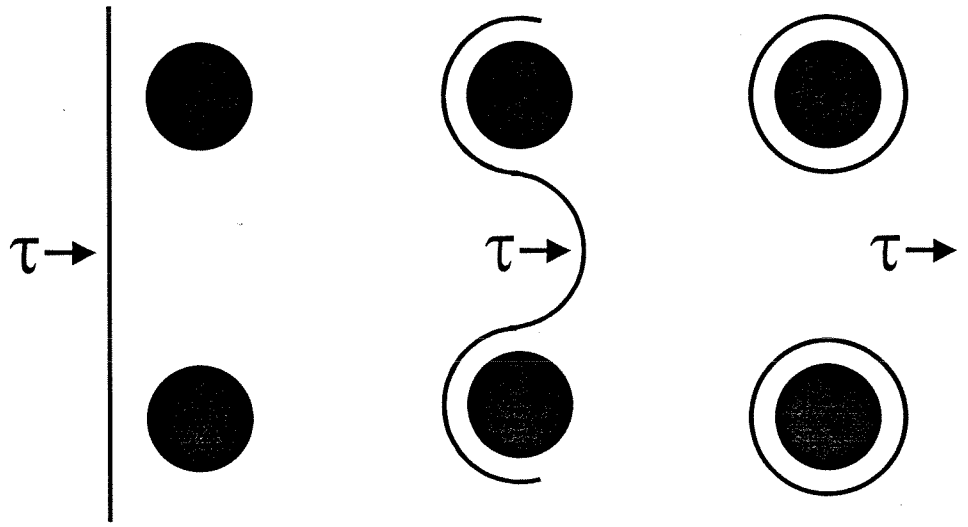

Figure 5.1 Orowan Model for Hardening in Precipitate Strengthened Alloys.

The presence of large precipitates within aluminum grains or at grain boundaries inhibit the mobility of dislocations (Hull, 1984). The precipitates are randomly dispersed and therefore intersect the slip planes. When a dislocation line encounters a precipitate, its motion is affected by short range forces due to the stress field surrounding the particle. The force necessary for the dislocation to overcome the barrier depend on several factors, including precipitate size, hardness, spacing, and coherency between the precipitate and surrounding aluminum lattice. In turn, these precipitate characteristics can be varied significantly by heat treatment. For alloys that are not artificially aged, the precipitates are relatively small and soft, and coherent with the aluminum matrix. In this case, it is easier for the dislocation to shear, or "cut," the precipitate. With increased aging time,

the particles increase in size, become harder, and begin to lose coherency with the aluminum matrix. Strength for these tempers is governed by the force necessary to "bend" dislocations around the precipitates. The concept for the classic model of precipitate strengthening, due to Orowan (1948), is sketched in Figure 5.1. The dislocation line is assumed to have an equivalent tension. To overcome the barrier, the dislocation line must bend into a semi-circular geometry between two precipitates. As the line "passes through" the neighboring precipitates, loops are left surrounding each particle which increases its effective size. A sketch of a typical ageing curve for precipitate strengthened aluminum alloys is given in Figure 5.2. The various tempers (T3, T4, T6, etc.) are also denoted relative to this sketch. The T3 and T7 type tempers indicate that a certain amount of cold work was performed after solution treating. T4, T6, and T8 tempers are not cold worked.

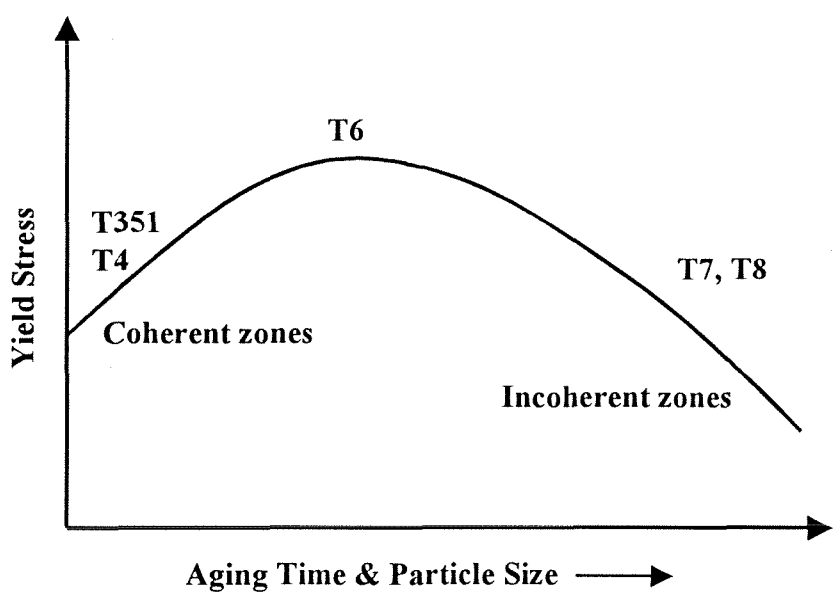

Figure 5.2 **Variation of yield stress with aging time typical of precipitate strengthened aluminum alloys.**

5.2 Raw Data and Analysis.

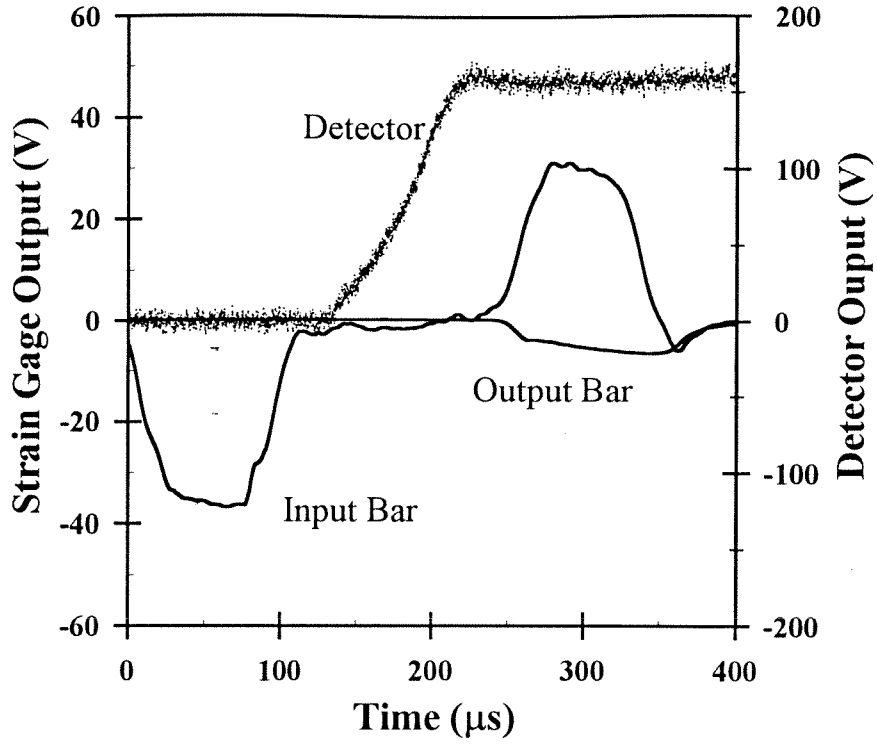

Figure 5.3 **Typical mechanical and thermal data for compression Kolsky bar tests involving aluminum alloys.**

For dynamic tests on the Kolsky bar, the method of calculating the fraction of mechanical work dissipated as heat proceeded much the same as for α-titanium. Raw data, from the strain gages and HgCdTe infrared detector, is shown in Figure 5.2 for 2024-T351 aluminum. The data in the figure closely resembles the data for α-titanium in Figure 4.2. The reader is referred to Chapter 4 for details on the analysis of Kolsky bar data. After applying a calibration to the thermal data in Figure 5.3, the temperature profile is shown in Figure 5.4.

Thermal data was also obtained for 2024 aluminum during tests on the MTS load frame at strain rates near 1 s^{-1}. Due to its high thermal diffusivity, the critical time for aluminum (refer to Table 3.1) was an order of magnitude lower than α-titanium. For

titanium, tests at these strain rates were nearly adiabatic for the entire test duration. This was not true for aluminum. Roughly, the first half of a 1 s-1 test of 2024 aluminum could be considered adiabatic. The strain rate is constant for an MTS test, so adiabatic conditions hold from 0 to 15-20% strain. Conduction effects become important at higher times, or equivalently, higher strains.

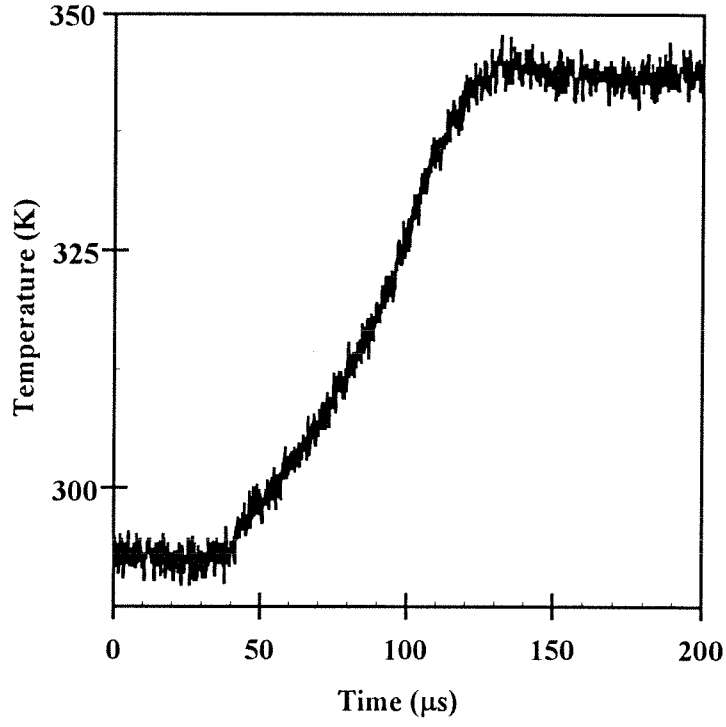

Figure 5.4 Temperature rise during dynamic uniaxial compression of 2024 aluminum .

5.3 Results and Discussion.

The compressive stress-strain curves for 2024 aluminum in the T351 temper is given in Figure 5.2. The T351 and T4 tempers are underaged, so their initial flow stress was relatively low. T351 is a cold worked after solid solution treatment, therefore at low plastic strains, the flow stress is 50 MPa greater than the annealed T4 temper. T6 is the designation for the peak aged temper, but in the case above, the alloy was slightly overaged to achieve near elastic-perfectly plastic stress-strain behavior. The flow stress

for T6 at yield was higher than that of T351 and T4, but does not increase appreciably during subsequent plastic flow. Because of the initial amount of cold work in the T351 temper, the initial dislocation density was appreciably higher than that of the T4 temper. During the initial stages of plastic flow, dislocations multiplied at a greater rate in T4, which was evident from the fact that the stress-strain curves for this temper exhibited substantial strain hardening. However, at large strains (ε>0.3), the response for T351 and T4 tempers merged and subsequently deformed with relatively little hardening.

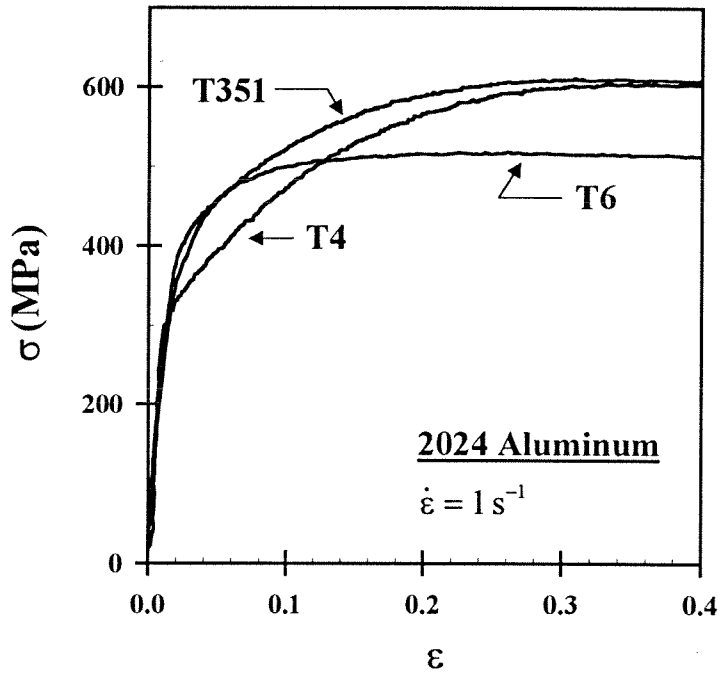

Figure 5.5 A comparison of true compressive stress-strain response for several tempers of 2024 aluminum alloy.

Figure 5.6 plots true compressive stress-strain curves for the T351 temper at two strain rates. Over the first 25-30 % the flow stress was nearly equal, over a range of strain rates from 10^{-3} s^{-1} to 3000 s^{-1}. Although the 10^{-3} s^{-1} test was nearly isothermal, and the 3000 s^{-1} was nearly adiabatic (Fig. 3.18), the stress-strain curves closely overlapped. The temperature rise in during a dynamic compression test was never more than 60 °C

above room temperature, which was barely 10% of the melting temperature. This explains the lack of significant thermal softening for the 3000 s^{-1} test in Figure 5.6. Although not shown here, the flow stress for all tempers tested was independent of strain rate within this range.

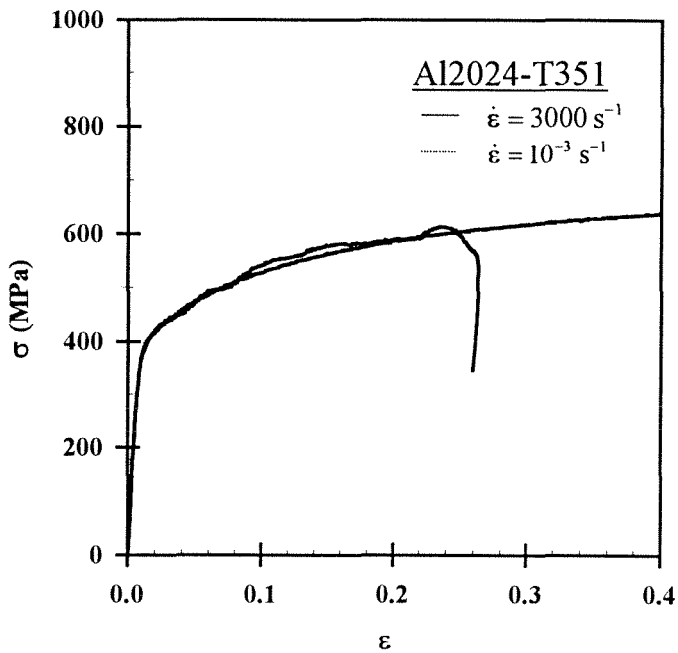

Figure 5.6 True Compressive stress-strain curves for Al2024-T351 at two strain rates

The fraction of plastic work dissipated as heat for 2024-T351 in compression is shown in Figure 5.7. These curves represent the functional dependence of β on the first 15% engineering plastic strain after yield. The two curves at 3000 s^{-1} represent two separate tests at that strain rate, and gave some measure of repeatability of the experimental method. There was no observed dependence of β on strain rate, although the tests shown in the figure were only separated by a factor of 3 in rate. As explained in the previous chapter, the near yield value of β for dynamic tests on the Kolsky bar was difficult to pinpoint. However, for the first few percent plastic strain, β was observed to

be a rapidly decreasing function of strain. Between 5-15 % plastic strain, only 30-35% of plastic work was dissipated as heat – a nearly constant value over that range.

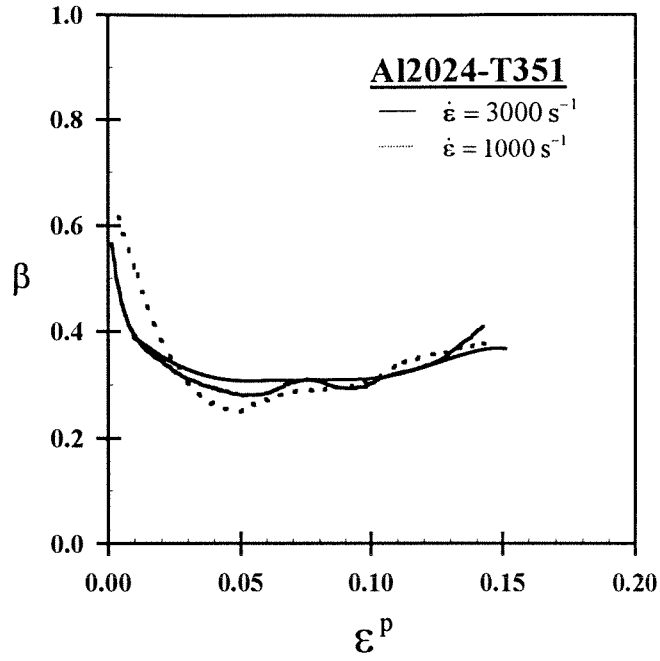

Figure 5.7 Fraction of plastic work converted into heat at low strains in Al2024-T351

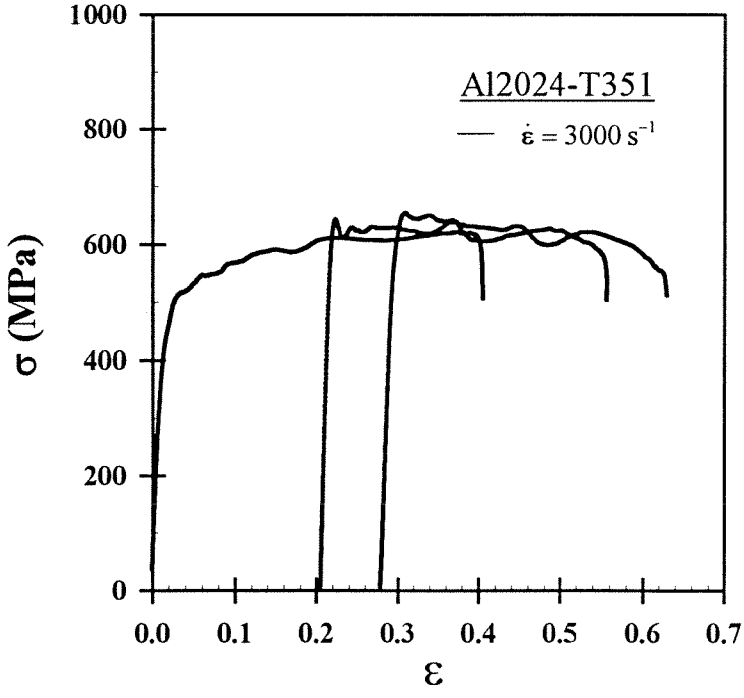

Figure 5.8 Sequence of true stress-strain curves at 3000 s^{-1} produced by recovering and reloading samples.

To determine the relative partition of plastic work at higher levels of strain in compression, the remachining technique described in Chapter 3 was employed. The emissivity of aluminum changes appreciably as plastic strain is accumulated, so the remachining technique was necessary to maintain nearly constant emissivity relative to strain. The true stress-strain curves in Figure 5.8 was produced from three separate samples, each with varying amounts of residual deformation, but with identical surface finish.

Large plastic strains can also be obtained during dynamic torsion. Equivalent stress and strain from a torsion test of 2024-T351 aluminum was superimposed onto Figure 5.8 and plotted separately in Figure 5.9.

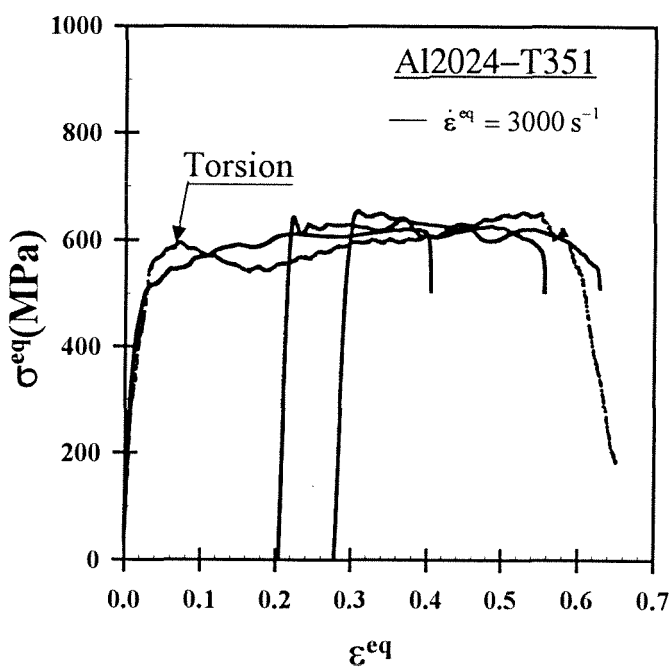

Figure 5.9 Comparison of large strain compression with equivalent stress-strain curve obtained from the torsion Kolsky bar.

The calculation of β for the three tests of Figure 5.8 are shown in Figure 5.10. From 0 to 15% plastic strain, the dependence of β on strain resembled the tests of Figure 5.7. After 15%, the ability to store energy decreases, and β rapidly increases. After 30-

35% plastic strain has been accumulated, nearly all input work was dissipated as heat. These trends were similar for β calculated from aluminum deformed in torsion (Figure 5.11). In torsion, at low strains, β was a decreasing function of strain. After only 10% strain, β begins to rise gradually towards a maximum near 1.0. Although the functional trends were indeed similar, there were a few errors associated with the torsion test. Heat conduction effects were more pronounced, especially for aluminum, in torsion than in compression.

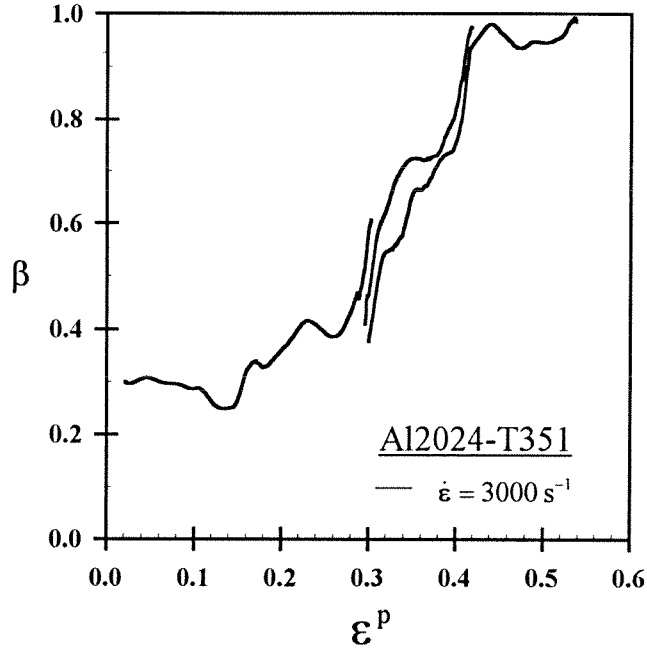

Figure 5.10 Fraction of plastic work converted into heat over large strains for Al2024-T351 deformed in the compression Kolsky Bar.

The design of the torsion specimen included integral flanges connected to the gage section. In compression, heat transfer between the deforming sample and the Kolsky bar occurred across a rough interface. Rough interfaces act as barriers to heat conduction. No such barriers existed in the torsion samples. In addition, because of the dimensions of the gage section, torsion samples could not be remachined in a similar fashion as compression samples. Thus, the plot in Figure 5.11 in torsion represented a curve of

varying emissivity, and conduction effects that increased with plastic strain. The increased emissivity was one reason that the entire curve in torsion lies above the compression curves. If conduction effects were not present, at the larger strains, β would tend towards 1.0 more rapidly.

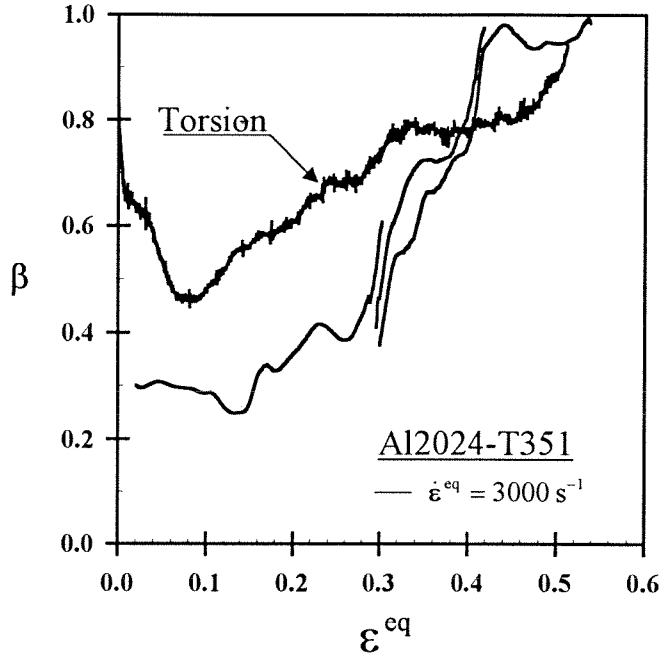

Figure 5.11 Comparison of the fraction of plastic work converted into heat obtained in compression and in torsion.

For the T4 and T6 tempers in dynamic compression, the β is plotted against plastic strain in Figure 5.12. Both tempers store more than 50% of input plastic work during the onset of plastic flow. After about 8% plastic strain, the T6 temper can no longer increase its internal energy, and subsequent plastic work is dissipated as heat. The T4 temper can store energy out to larger strains than T6, but also reaches a critical strain, after which nearly all work was dissipated.

At lower strain rates, the functional form of β for both tempers were similar to Figure 5.12. Figure 5.13 shows the result of the MTS test of 2024-T6, compared with a

compression Kolsky bar test. Figure 5.14 plots similar data for 2024-T4. For each temper, conduction effects played an important role at higher strains in the MTS. At low strains, the deformation was still adiabatic, and the low strain rate test can be directly compared to the β curve obtained in the Kolsky bar – which has been shown to be adiabatic for all strains in this range. Strain rate, again, was observed to have little effect on the fraction of work converted into heat, at least at low strains.

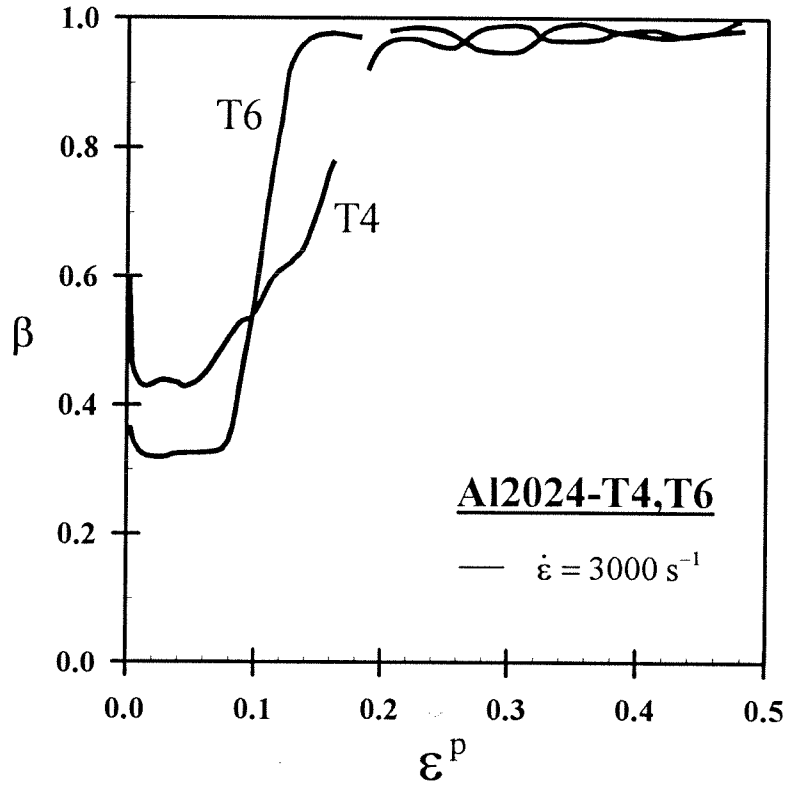

Figure 5.12 Comparison of the fraction of plastic work dissipated as heat between the T4 and T6 tempers of 2024 aluminum alloy.

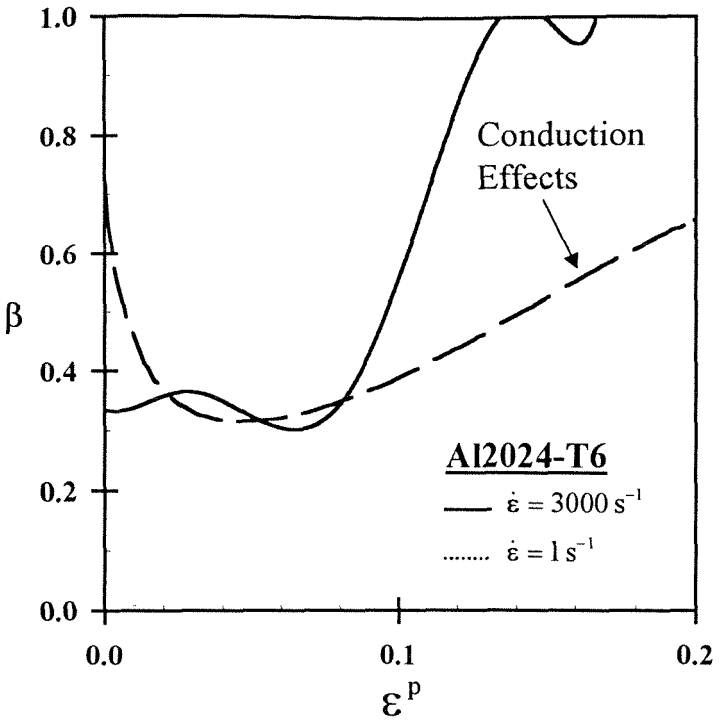

Figure 5.13 Strain rate dependence of the fraction of plastic work converted into heat for Al2024-T6.

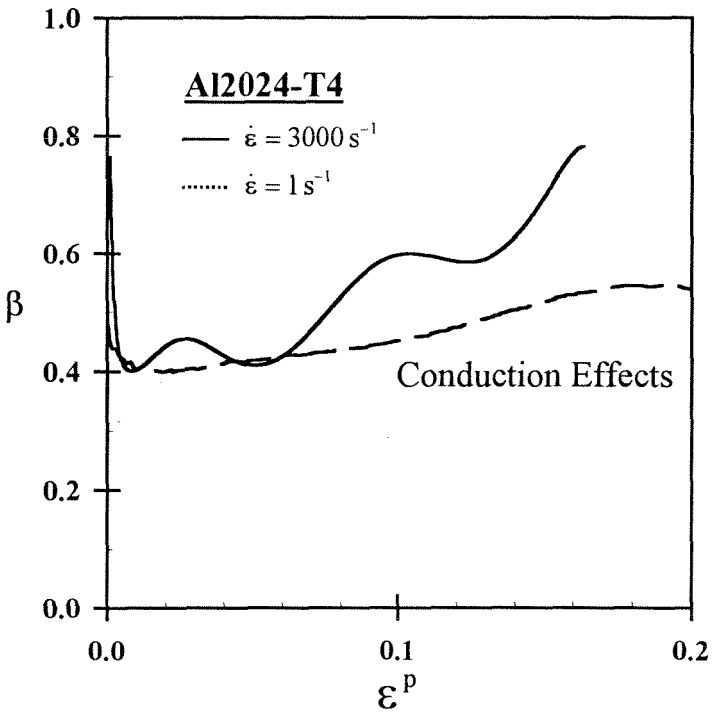

Figure 5.14 Strain rate dependence of the fraction of plastic work converted into heat for Al2024-T4.

5.4 References

Hornbogen, E., Starke, E.A. (1993), "Theory Assisted Design of High Strength Low Alloy Aluminum," *Acta Metall.*, **41**, 1.

Hull, D., Bacon, D.J. (1984), *Introduction to Dislocations*, Pergamon Press, Elmsford, NY.

Johnson, G.R., Cook, W.H. (1985), "Fracture Characteristics of Three Metals Subjected to Various Strains, Strain Rates, Temperatures, and Pressures," *Eng. Fracture Mechanics*, **21**, 31.

Meyers, M.A., Chawla, K.K. (1984), *Mechanical Metallurgy*, Prentice-Hall, New York.

Orowan (1948), *Internal Stresses in Metals and Alloys*, Institute of Metals, London.

Stevens, R.H. (1990), "Aluminum Alloys," in *ASM Handbook: Vol 2*, ASM International , Metals Park, OH.

CHAPTER 6

CONCLUSIONS

6.1 Summary

Based on the results of the previous chapters, several conclusions can be made regarding the dissipation of plastic work as heat, as well as the experimental techniques that produced these results:

- A novel experimental setup was used to measure the partition of plastic work into heat and stored energy in plastically deforming metals. A high-speed HgCdTe photoconductive detector, together with custom infrared optics, was used to determine heat evolution during dynamic deformations. The time response of the detector system was on the order of 0.5 μs, and had a temperature resolution of less than 1 °C near ambient (room temperature) conditions. The HgCdTe photoconductive detector was ideally suited to measure small temperature excursions from ambient conditions, and proved a vast improvement over InSb photovoltaic detectors for this purpose. The Kolsky bar, in compression and torsion, provided uniaxial dynamic loading.
- A technique was developed to experimentally calibrate the HgCdTe detector system which allowed for accurate temperature measurement.
- The experimental setup was capable of repeatable measurement of the mechanical and thermal field quantities.

- The surface roughness of metal samples was found to increase over moderate levels of plastic strain, which increased the effective emissivity of the sample. This had implications on the validity of the infrared detector calibration. A technique of recovering samples after initial loading, removing the rough outer surface layer, and reloading was developed to obtain large plastic strains in the Kolsky bar. The validity of the temperature calibration was extended by keeping the surface roughness nearly constant.
- The adiabatic, homogenous deformation in the Kolsky bar allowed a simple calculation of the fraction of plastic work converted into heat. The ratio of plastic work converted into heat, β, was treated as a material constitutive function, and its dependence on both strain and strain rate was investigated.
- A Materials Testing System (MTS) servo-hydraulic load frame was used to measure mechanical properties at lower strain rates, 10^{-5} s^{-1} to 1 s^{-1}. When temperature measurement was needed within this range of strain rates, an E-type thin wire thermocouple, with a time response of 1 ms, was employed. With this setup, the fraction of energy converted into heat could be ascertained at moderate strain rates.
- 2024 aluminum alloy, and commercially pure α-titanium were the metal systems used in the current study to determine the functional dependence of β on strain and strain rate.
- The T351, T4 and T6 tempers of 2024 aluminum did not exhibit strain rate dependence in flow stress over the entire range of strain rates tested. At low levels of plastic strain, all tempers of 2024 aluminum stored more than 50% of the input plastic work. At some level of plastic strain, depending on temper, 2024 aluminum could no

longer store plastic work. After this point, β increased to a value near 1.0 and remained nearly constant during subsequent plastic deformation. When averaged over all strains, β was 0.85-0.95 depending on the particular heat treatment. The fraction of plastic work dissipated as heat was not found to be sensitive to strain rate over a wide range of strain rates.

- In contrast to aluminum, the flow stress of α-titanium was strongly dependent on strain rate. The initial flow stress increased by more than 15% between strain rates of 10^{-3} s^{-1} and 10^{3} s^{-1}. In addition, the strain hardening was also observed to be rate dependent. For fixed plastic strain, the tangent modulus increased as strain rate increased. Titanium dissipated a greater proportion of energy as heat at low strains than all tempers of 2024 aluminum. The ability to store energy in titanium decreased with increasing plastic strain. For plastic strains above 0.25-0.3, titanium dissipated nearly all input plastic work as heat. The proportion of energy dissipated as heat at fixed strain increased as strain rate increased.
- The experimental results for the fraction of mechanical work converted into heat, or equivalently, the fraction of stored energy, was compared to the predictions of several existing models. Models based solely on a single mechanism, such as dislocation generation or residual stresses, were only accurate within a range of strains where a single mechanism was dominant. In general, these types of models cannot accurately predict energy storage, or energy dissipation, over a wide range of plastic strains or strain rates. More appropriate models used to predict the experimental results were those which considered fundamental thermodynamic constitutive functions, and incorporated microstructural parameters as internal variables.

6.2 Final Comments & Future Work

The majority of experimental investigations raise (at least) as many questions as they hope to answer. The work presented here is, perhaps, no exception. Is there truly a critical strain, after which all subsequent plastic work is dissipated as heat? Is it a material property? Does it depend on strain rate? How are some metals able to store so much energy at low strains? Many of the questions are out of the scope of the current study, but one could conceive of methods to answer them.

The techniques used to determine the amount of plastic work dissipated as heat were tailored to provide a reasonably degree of accuracy. The various experimental configurations are ideally suited to determine the fraction of plastic work converted into heat as a function of strain. Moreover, a wide enough range of strain rates was obtained in order to demonstrate rate dependence of β for rate-sensitive metals. Unfortunately, the techniques used here could only be applied over (a relatively small) three orders of magnitude in strain rate (1 s^{-1} to $3x10^3$ s^{-1}). These are some ideas concerning future directions and improvements:

- With current methods, it is difficult to determine the fraction of plastic work converted into heat for metals which tend to localize during plastic deformation. Often, it is these materials that are of interest to researchers who study shear localization and dynamic fracture.

- For single crystals, the only mechanism of energy storage is dislocation creation and their mutual interaction. Polycrystals have potentially more avenues for energy storage. For polycrystals containing multiple phases, isolating the various storage mechanisms can be a difficult task. Only by systematically varying the

microstructure could one hope to experimentally determine the relative importance of each storage mechanism.

- Quantitative microscopy, in tandem with a systematic variation of microstructure, could provide insight into the relative importance of the various storage mechanisms.
- Data from other rate-dependent metals are needed to assess the predictive capability of model developed in Chapter 2 (section 2.1).